



SPRING/SUMMER 2015
VOLUME 7, NUMBER 1

Print ISSN: 2152-4157
Online ISSN: 2152-4165

WWW.IJERI.ORG

International Journal of Engineering Research & Innovation

Editor-in-Chief: Mark Rajai, Ph.D.
California State University Northridge



Published by the
International Association of Journals & Conferences



www.ijeri.org

Print ISSN: 2152-4157
Online ISSN: 2152-4165



www.iajc.org

INTERNATIONAL JOURNAL OF ENGINEERING RESEARCH AND INNOVATION

ABOUT IJERI:

- IJERI is the second official journal of the International Association of Journals and Conferences (IAJC).
- IJERI is a high-quality, independent journal steered by a distinguished board of directors and supported by an international review board representing many well-known universities, colleges, and corporations in the U.S. and abroad.
- IJERI has an impact factor of **1.58**, placing it among an elite group of most-cited engineering journals worldwide.

OTHER IAJC JOURNALS:

- The International Journal of Modern Engineering (IJME)
For more information visit www.ijme.us
- The Technology Interface International Journal (TIIJ)
For more information visit www.tiij.org

IJERI SUBMISSIONS:

- Manuscripts should be sent electronically to the manuscript editor, Dr. Philip Weinsier, at philipw@bgsu.edu.

For submission guidelines visit
www.ijeri.org/submissions

TO JOIN THE REVIEW BOARD:

- Contact the chair of the International Review Board, Dr. Philip Weinsier, at philipw@bgsu.edu.

For more information visit
www.ijeri.org/editorial

INDEXING ORGANIZATIONS:

- IJERI is indexed by numerous agencies. For a complete listing, please visit us at www.ijeri.org.

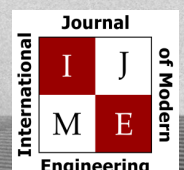
Contact us:

Mark Rajai, Ph.D.

Editor-in-Chief
California State University-Northridge
College of Engineering and Computer Science
Room: JD 4510
Northridge, CA 91330
Office: (818) 677-5003
Email: mrajai@csun.edu



www.tiij.org



www.ijme.us

INTERNATIONAL JOURNAL OF ENGINEERING RESEARCH AND INNOVATION

The INTERNATIONAL JOURNAL OF ENGINEERING RESEARCH AND INNOVATION (IJERI) is an independent and nonprofit publication, which aims to provide the engineering community with a resource and forum for scholarly expression and reflection.

IJERI is published twice annually (fall and spring issues) and includes peer-reviewed research articles, editorials, and commentary that contribute to our understanding of the issues, problems, and research associated with the engineering and related fields. The journal encourages the submission of manuscripts from private, public, and academic sectors. The views expressed are those of the authors, and do not necessarily reflect the opinions of the IJERI or its editors.

EDITORIAL OFFICE:

Mark Rajai, Ph.D.
Editor-in-Chief
Office: (818) 677-2167
Email: ijmeeditor@iajc.org
Dept. of Manufacturing Systems
Engineering & Management
California State University-
Northridge
18111 Nordhoff Street
Northridge, CA 91330-8332

THE INTERNATIONAL JOURNAL OF ENGINEERING RESEARCH AND INNOVATION EDITORS

Editor-in-Chief:

Mark Rajai

California State University-Northridge

Associate Editors:

Paul Wilder

Vincennes University

Li Tan

Purdue University North Central

Production Editor:

Philip Weinsier

Bowling Green State University-Firelands

Subscription Editor:

Morteza Sadat-Hossieny

Northern Kentucky University

Web Administrator:

Saeed Namyar

Advanced Information Systems

Manuscript Editor:

Philip Weinsier

Bowling Green State University-Firelands

Copy Editors:

Li Tan

Purdue University North Central

Ahmad Sarfaraz

California State University-Northridge

Technical Editors:

Marilyn Dyrud

Oregon Institute of Technology

David Foster

Kettering University

Publisher:

International Association of Journals and Conferences

TABLE OF CONTENTS

<i>Editor's Note (In This Issue): Space Perception and Navigation Assistance for the Visually Impaired using Depth Sensors and Haptic Feedback</i>	3
Philip Weinsier, IJERI Manuscript Editor	
<i>A Taylor Tool Life Constant-Based Method for the Analysis of the Effect of Coolant/Lubricant Selection on Machining Operations</i>	5
Kevin M. Hubbard, Missouri State University; Martin P. Jones, Missouri State University; Richard N. Callahan, Missouri State University	
<i>Effects of Elevated Temperatures on Bond Strength between Epoxy-Coated Reinforcement and Fiber-Reinforced Concrete</i>	13
José A. Peña, Purdue University Calumet; Drew Oppenhuis, Purdue University Calumet	
<i>A Comparative Study on the Micromachining Performance of Copper, Brass, and Aluminum</i>	23
Muhammad P. Jahan, Western Kentucky University; Gregory K. Arbuckle, Western Kentucky University; Abdulhameed Dawood, Western Kentucky University	
<i>Ramp Rate Effect on Maximizing Profit of a Microgrid using a Gravitational Search Algorithm</i>	32
F. Safdarian, Amirkabir University of Technology (Tehran Polytechnic); M.M. Ardehali, Amirkabir University of Technology (Tehran Polytechnic); G.B. Gharehpetian, Amirkabir University of Technology (Tehran Polytechnic)	
<i>Analysis of Wind-Power Generation with a Wind-Guide Attachment</i>	43
Ulan Dakeev, University of Michigan–Flint; Connie Lam, University of Michigan–Flint; James Pung, University of Michigan–Flint	
<i>Vertical Axis Wind Turbine Performance Prediction Models Using High and Low Fidelity Analyses</i>	48
Franklyn Kanyako, Masdar Institute of Science and Technology, UAE; Isam Janajreh, Masdar Institute of Science and Technology, UAE	
<i>Space Perception and Navigation Assistance for the Visually Impaired Using Depth Sensors and Haptic Feedback</i>	56
Kumar Yelamarthi, Central Michigan University; Kevin Laubhan, Central Michigan University	
<i>Capstone Project: PLC Control System with Integrated PID Controller for Control System Optimization</i>	63
Abdullah Al Atwa, Michigan Technological University; Ian Bumgardner, Michigan Technological University; Mohammed Bushlaibi, Michigan Technological University; Steven Castello, Michigan Technological University; Joshua Erickson, Michigan Technological University; Aleksandr Sergeyev, Michigan Technological University; Mohsen Azizi, Michigan Technological University	
<i>Instructions for Authors: Manuscript Requirements</i>	72

IN THIS ISSUE (p.56)

SPACE PERCEPTION AND NAVIGATION ASSISTANCE FOR THE VISUALLY IMPAIRED USING DEPTH SENSORS AND HAPTIC FEEDBACK

Philip Weinsier, IJERI Manuscript Editor

For anyone following my *Editor's Notes*, you may start to see some recurring themes; not for lack of interesting research to choose from, but rather because I consider it important to focus on work that helps humans feel more, well, human. Two years ago (Spring/Summer 2013, v5 n1), I featured a joint article—Johns Hopkins University and Penn State University—by the HOAD Research Group in which the authors developed a hand-opening assistive device for stroke victims and the neurologically impaired. In this current issue, I have again chosen to highlight an article related to helping individuals with sensory deprivation. In this case, the authors used a 3D depth sensor—used extensively in the computer vision and gaming industry—and haptic feedback in the development of a lightweight and low-cost navigation assistive device for the visually impaired.

There are 285 million visually impaired people worldwide (according to the World Health Organization), 90% of whom live in developing countries and 65% of whom are aged 50 and above; thus, the first two key terms here are lightweight and low cost: lightweight, as the elderly generally will not have the strength and endurance of younger people; and, low cost, as people living in developing countries have comparatively little money for the purchase of such devices. But there are two more terms in this article that beg for attention: haptic and visually impaired. Vision, or sight (ophthalmoception), is one of our five senses—the others being hearing (audioception), taste (gustaoception), smell (olfaoception), and touch (tactioception or tactile perception). Consider also that one definition of “sense” is a physiological capacity to perceive information. I’m sure you can now see where the authors are going with this.

But these five senses are not our only means for detecting stimuli, we also have the ability to perceive information via temperature, (thermoception), kinesthetics (proprioception), pain (nociception), balance (equilibrioception), and vibration (mechanoreception), among others. Haptic technology deals with tactile perception and kinesthetics (our ability to feel movements of our limbs and body). Proprioception—coming from Latin, *proprius* means “own” plus reception—is our ability to sense not simply the movements of our body parts but also position, location, and orientation.

At this point, you are no doubt wondering about the connection between all of this discussion about our senses and helping visually impaired people navigate. A few examples likely will put things into perspective. Do you use a cell phone? Have you ever had to put it on vibrate so as not to annoy your neighbors? Have you typed a text message on a smartphone and felt a small vibration in your fingertips with each key stroke? How about gaming your way through an enemy horde and felt each shot of your rifle? If you have kids, have you had the thrill of riding along in *Mario Kart* and experienced the feel of hitting a wall or another driver? Ever played *Wii* tennis and experienced the feedback you get in your controller each time you hit the ball? Ok, just one more: Have you ever operated on a patient, who literally is hundreds of miles away, using telesurgery? I think I’m safe in assuming that you answered yes to at least one these. Thus, you have experienced haptic feedback technology.

But haptic feedback is more than simply a vibration response from a device. One might say that vibration alerting is a subset of haptic feedback, but it’s particularly effective if all you require is a simple response, and it’s certainly cheaper to implement than a haptic system. Take, for example, the situation of a car with a parking sensor backing up and coming close to an object. A simple response might be a beep from a speaker or a vibration in your steering wheel. A more complex, haptic response would have the beep from your speaker change in intensity or pitch as you got closer to the object; or, the vibration pattern in your steering wheel would change as you closed the distance to the object. It is also likely obvious, then, that the main concerns for the design of a vibration alerting system would be amplitude and power consumption.

For a haptic system, more involved electronics are called for. The system proposed by the authors of this current article is able to interpret a person’s field-of-view and convert information into a depth matrix, the data from which are processed in order for the person to recognize the nearby object as human or non-human and provide haptic feedback for continued navigation. The authors successfully identified, detected, and tracked the closest objects, including humans, based on real-time distance measurements.

Editorial Review Board Members

Mohammed Addallah	State University of New York (NY)	Shiyoung Lee	Penn State University Berks (PA)
Nasser Alaraje	Michigan Tech (MI)	Soo-Yen Lee	Central Michigan University (MI)
Aly Mousaad Aly	Louisiana State University (LA)	Chao Li	Florida A&M University (FL)
Jahangir Ansari	Virginia State University (VA)	Jimmy Linn	Eastern Carolina University (NC)
Kevin Berisso	Ohio University (OH)	Dale Litwhiler	Penn State University (PA)
Salah Badjou	Wentworth Institute of Technology (MA)	Guoxiang Liu	University of North Dakota (ND)
Pankaj Bhambri	Guru Nanak Dev Engineering (INDIA)	Louis Liu	University of New Orleans (LA)
Water Buchanan	Texas A&M University (TX)	Mani Manivannan	ARUP Corporation
Jessica Buck Murphy	Jackson State University (MS)	G.H. Massiha	University of Louisiana (LA)
John Burningham	Clayton State University (GA)	Thomas McDonald	University of Southern Indiana (IN)
Shaobiao Cai	Penn State University (PA)	David Melton	Eastern Illinois University (IL)
Vigyan Chandra	Eastern Kentucky University (KY)	Shokoufeh Mirzaei	Cal State Poly Pomona (CA)
Isaac Chang	Cal Poly State University SLO (CA)	Bashir Morshed	University of Memphis (TN)
Bin Chen	Purdue University Calumet (IN)	Sam Mryyan	Excelsior College (NY)
Wei-Yin Chen	University of Mississippi (MS)	Wilson Naik	University of Hyderabad (INDIA)
Hans Chapman	Morehead State University (KY)	Arun Nambiar	California State University Fresno (CA)
Rigoberto Chinchilla	Eastern Illinois University (IL)	Ramesh Narang	Indiana University-Purdue University (IN)
Phil Cochrane	Indiana State University (IN)	Anand Nayyar	Institute Management and Tech (INDIA)
Michael Coffman	Southern Illinois University-Carbondale (IL)	Stephanie Nelson	Cal State LA (CA)
Emily Crawford	Southern Wesleyan University (SC)	Hamed Niroumand	Universiti Teknologi (MALAYSIA)
Brad Deken	Southeast Missouri State University (MO)	Aurenice Oliveira	Michigan Tech (MI)
Z.T. Deng	Alabama A&M University (AL)	Troy Ollison	University of Central Missouri (MO)
Sagar Deshpande	Ferris State University (MI)	Reynaldo Pablo	Indiana University-Purdue University (IN)
David Domermuth	Appalachian State University (NC)	Basile Panoutsopoulos	Community College of Rhode Island (RI)
Ryan Dupont	Utah State University (UT)	Shahera Patel	Sardar Patel University (INDIA)
Marilyn Dyrud	Oregon Institute of Technology (OR)	Jose Pena	Purdue University Calumet (IN)
Mehran Elahi	Elizabeth City State University (NC)	Karl Perusich	Purdue University (IN)
Ahmed Elsayy	Tennessee Technological University (TN)	Thongchai Phairoh	Virginia State University (VA)
Rasoul Esfahani	DeVry University (OH)	Huyu Qu	Honeywell Corporation
Dominick Fazarro	Sam Houston State University (TX)	John Rajadas	Arizona State University (AZ)
Morteza Firouzi	University of Technology (MALAYSIA)	Desire Rasolomampionona	Warsaw University of Tech (POLAND)
Rod Flanigan	University of Nebraska-Kearney (NE)	Mulchand Rathod	Wayne State University (MI)
Ignatius Fomunung	University of Tennessee Chattanooga (TN)	Mohammad Razani	New York City College of Tech (NY)
Ahmed Gawad	Zagazig University EGYPT)	Sangram Redkar	Arizona State University-Poly (AZ)
Daba Gedafa	University of North Dakota (ND)	Michael Reynolds	University of Arkansas Fort Smith (AR)
Ralph Gibbs	Eastern Kentucky University (KY)	Marla Rogers	Wireless Systems Engineer
Mohsen Hamidi	Utah Valley University (UT)	Dale Rowe	Brigham Young University (UT)
Mamoon Hammad	Abu Dhabi University (UAE)	Anca Sala	Baker College (MI)
Youcef Himri	Safety Engineer in Sonelgaz (ALGERIA)	Mehdi Shabaninejad	Zagros Oil & Gas Company (IRAN)
Xiaobing Hou	Central Connecticut State University (CT)	Ehsan Sheybani	Virginia State University (VA)
Shelton Houston	University of Louisiana Lafayette (LA)	Musibau Shofoluwe	North Carolina State University (NC)
Barry Hoy	St. Leo University (VA)	Siles Singh	St. Joseph University Tanzania (AFRICA)
Ying Huang	North Dakota State University (ND)	Ahmad Sleiti	University of North Carolina Charlotte (NC)
Charles Hunt	Norfolk State University (VA)	Jiahui Song	Wentworth Institute of Technology (MA)
Dave Hunter	Western Illinois University (IL)	Yuyang Song	Toyota Corporation
Christian Hyeng	North Carolina A&T University (NC)	Carl Spezia	Southern Illinois University (IL)
Pete Hylton	Indiana University Purdue (IN)	Michelle Surerus	Ohio University (OH)
Ghassan Ibrahim	Bloomsburg University (PA)	Vassilios Tzouanas	University of Houston Downtown (TX)
John Irwin	Michigan Tech (MI)	Jeff Ulmer	University of Central Missouri (MO)
Sudershan Jetley	Bowling Green State University (OH)	Mihaela Vorvoreanu	Purdue University (IN)
Rex Kanu	Ball State University (IN)	Phillip Waldrop	Georgia Southern University (GA)
Reza Karim	North Dakota State University (ND)	Abraham Walton	Purdue University (IN)
Tolga Kaya	Central Michigan University (MI)	Liangmo Wang	Nanjing University of Science/Tech (CHINA)
Satish Ketkar	Wayne State University (MI)	Jonathan Williams	Lake Erie College (OH)
Manish Kewalramani	Abu Dhabi University (UAE)	Boonsap Witchayangkoon	Thammasat University (THAILAND)
Tae-Hoon Kim	Purdue University Calumet (IN)	Alex Wong	Digilent Inc.
Doug Koch	Southeast Missouri State University (MO)	Shuju Wu	Central Connecticut State University (CT)
Sally Krijestorac	Daytona State College (FL)	Baijian Yang	Ball State University (IN)
Ognjen Kuljaca	Brodarski Institute (CROATIA)	Mijia Yang	North Dakota State University (ND)
Chakresh Kumar	Uttar Pradesh Tech University (INDIA)	Faruk Yildiz	Sam Houston State University (TX)
Zaki Kuruppallil	Ohio University (OH)	Yuqiu You	Morehead State University (KY)
Edward Land	Johns Hopkins Medical Institute	Jinwen Zhu	Missouri Western State University (MO)
Ronald Land	Penn State University (PA)		
Jane LeClair	Excelsior College (NY)		

A TAYLOR TOOL LIFE CONSTANT-BASED METHOD FOR THE ANALYSIS OF THE EFFECT OF COOLANT/LUBRICANT SELECTION ON MACHINING OPERATIONS

Kevin M. Hubbard, Missouri State University; Martin P. Jones, Missouri State University; Richard N. Callahan, Missouri State University

Abstract

The calculation of the cutting conditions, which result in the optimization of parameters such as unit cost of production and maximum production rate, has traditionally been performed under the assumptions that each factor considered is deterministic and that the major determining factor in these calculations is cutting speed. Many factors incorporated in these calculations, however, exhibit stochastic variation rather than deterministic behavior. Recently, it has become evident that the properties of the coolants/lubricants employed in machining operations, for example, exhibit stochastic variation.

One result of the stochastic variation observed in coolant/lubricant properties and performance is a variation in tool life and, specifically, a variation in the values of the constants appearing in the Taylor Tool Life equation. In this paper, a method is detailed capturing and accounting for this variation and assessing its effect on the unit cost of production of machined work parts. A test case was also formulated and analyzed and the results of coolant/lubricant property variation were shown to be potentially much larger than the effects associated with variations in cutting speed.

Introduction

The use of cutting fluids (either coolants or lubricants) in machining operations provides benefits including [1]:

- Increased cutting-tool life;
- Reduced temperatures at the tool/work/chip interface;
- Improved surface finish and integrity;
- Reduction or elimination of residual stresses in the machined work part;
- Reduction or elimination of built-up-edge chip formation; and,
- Increased rate of production.

The use of coolants/lubricants in machining may, therefore, result in lower unit costs of production and improved work part quality. However, costs are incurred through the use of coolants/lubricants as well. As Environmental Protection Agency (EPA) and Occupational Safety and Health

Administration (OSHA) regulations have become more stringent, increased costs have become associated with the use of these fluids [2]. For a particular work material, the selection of cutting-tool material can also have a significant effect on many of these parameters. In particular, the selection of cutting-tool material has an effect on tool life, production rate, and unit cost. Often, the use of a more expensive cutting-tool material results in a lower unit cost and/or a greater production rate [3].

The determination of the cutting conditions, which result in maximum production rate or those which result in minimum unit cost, was derived in 1950 [4] and is relatively straightforward. This traditional derivation, however, assumed deterministic rather than stochastic work material, tool material, and coolant/lubricant properties. A variation in cutting-tool material results in changes in the constants employed in Taylor's Tool Life equation. In addition, coolant/lubricant selections have an effect on Taylor Tool Life constants [5]. These constants appear in the relationships that describe material removal rate, production rate, and the unit cost of machined work parts. As Taylor constants vary, optimum cutting conditions, including spindle speed, cutting speed, feed, and feed rate, also vary [6]. As a result, changes in either the cutting-tool material employed and/or the coolant/lubricant used may have a significant effect on production rate and the unit cost of production.

In addition to these considerations, stochastic variations in work material properties, tool material properties, and coolant/lubricant properties each may have an effect on material removal rate, production rate, and the unit cost of production [7]. To compound these effects, changes in cutting conditions deliberately induced by shop floor personnel as well as inadvertent changes in coolant/lubricant mixture ratios may compound these effects. As a result of these factor changes, some amount of uncertainty exists in the selection of optimum cutting conditions for any given work part/cutting-tool/cutting-fluid scenario. Extensive analyses have been performed to document the effect of changes in cutting speed and cutting-tool material on tool life and, ultimately, on the unit cost of production. Very little attention, however, has been focused on the effect of the stochastic changes in coolant/lubricant properties and their effect on unit cost. In this study, the authors examined these effects.

Current Methodologies

The calculation of cutting speed, which maximizes production rate and minimizes the unit cost of production of machined work parts, is well documented [8] and given in Equation (1):

$$T_c = T_h + T_m + \frac{T_t}{n_p} \quad (1)$$

where,

- T_c = cycle time
- T_h = handling time
- T_m = machining time
- T_t = tool change time, when the tool change is attributed to a depleted cutting tool
- n_p = the number of parts that may be machined before the cutting tool is depleted

Note that the term T_t/n_p is the tool change time on a per-work part basis. Also:

$$T_m = \frac{\pi DL}{Vf} \quad (2)$$

where,

- D = cutting-tool diameter (for operations with rotating tools such as end milling and drilling)
- L = length of cut
- V = cutting speed
- f = feed

The simplest form of the Taylor Tool Life equation is shown in Equation (3):

$$C = VT^n \quad (3)$$

where,

- T = the life of the cutting tool, as predicted by the Taylor Tool Life equation (in minutes)
- C = a Taylor Tool Life equation constant that is numerically equal to the cutting speed (expressed in surface feet per minute, sfpm), which results in one minute of tool life
- n = a Taylor Tool Life equation constant that expresses the sensitivity of tool life with regard to changes in cutting speed

The number of parts that may be machined before the cutting tool is depleted, due to gradual wear is given by Equation (4):

$$n_p = \frac{T}{T_m} = \frac{fC^{1/n}}{\pi DLV^{(1/n-1)}} \quad (4)$$

In expanded form, then, Equation (1) becomes Equation (5):

$$T_c = T_h + \frac{\pi DL}{Vf} + \frac{T_t \pi DL V^{(1/n-1)}}{fC^{1/n}} \quad (5)$$

The cutting speed that results in minimum cycle time (and therefore maximum production rate) may be found by setting the derivative of Equation (5) to zero, as shown in Equation (6):

$$V_{\max Rp} = \frac{C}{\left[T_t \left(\frac{1}{n} - 1 \right) \right]^n} \quad (6)$$

where,

- $V_{\max Rp}$ = the cutting speed, which results in maximum rate of production.

The derivation for the cutting speed, which results in minimum unit cost, is similar and its result is presented in Equation (7):

$$V_{\min Cpc} = C \left[\frac{n}{1-n} \left(\frac{C_o}{C_o T_t + C_t} \right) \right]^n \quad (7)$$

where,

- $V_{\min Cpc}$ = the cutting speed, which results in minimum unit cost
- C_o = the shop rate (cost per time to operate the production operation)
- C_t = the cost of disposable tooling on a per-tool life (for re-grindable tooling) or on a per-cutting edge (for disposable insert tooling) basis

The C_t term may be expanded, as shown in Equation (8):

$$C_t = \frac{C_{pt}}{1 + n_{rs} - a} + (1-a)C_{otr} T_{rs} \quad (8)$$

where,

- C_{pt} = the cost to purchase one cutting tool
- n_{rs} = the number of allowable tool re-conditionings (for re-grindable tooling) or cutting edges (for disposable insert tooling)
- a = a factor equal to zero (for re-grindable tooling) or one (for disposable insert tooling)

Traditionally, the cutting speed, which results in minimum unit cost, has served as the lower bound for the cutting speed, which is actually employed in a given operation, while the cutting speed, which results in maximum production rate, has served as the upper bound, as depicted in Figure 1.

The values employed in the generation of the graph of Figure 1 are:

$$C = 809.3$$

$$n = 0.125$$

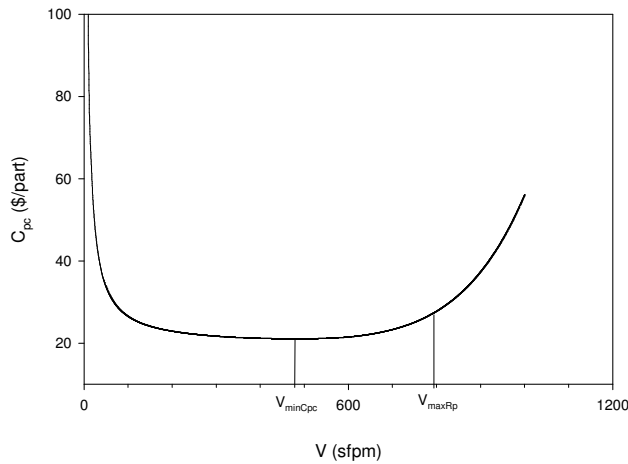


Figure 1. Unit Cost as a Function of Cutting Speed

These values are representative of the case where the work part is comprised of AISI 4140 steel with a hardness of approximately R_C25 ; the cutting tool is an uncoated carbide end mill, and the coolant/lubricant is a soluble oil (10% concentration by volume in water).

The Tool Life Constant Uncertainty Model

Figure 2 depicts the cutting speed versus unit cost curves for the production of a particular work part using two different coolant/lubricants.

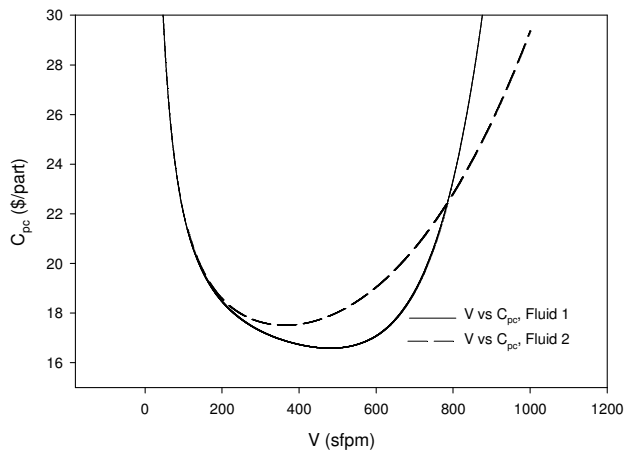


Figure 2. Cutting Speed versus Unit Cost Using Two Coolant/Lubricants

The data from which the curves of Figure 2 were generated are detailed in Table 1.

Table 1. Work part and Manufacturing Process Summary

Characteristic	Parameter
Work part Material	AISI 4140 Steel
Work part Material Hardness	R_c 24 to R_c 26
Operation	End Milling
Volume Removed	4.3 in ³
Material Removal Rate	0.459 in ³ /min.
Cutting Speed	400 sfpm
Chip Load	0.005 ipt
Number of Teeth	2
Machining Time	9.37 min.
Tool Material	Uncoated Carbide
Coolant/Lubricant 1	Soluble Oil, 10% Concentration in Water
Coolant/Lubricant 2	Soluble Oil with Extreme Pressure Additives, 10% Concentration in Water

Table 2 details the Taylor Tool Life equation constants for these work part material/cutting-tool/cutting fluid combinations (derived from data from the work done by McClure et al. [2] and Groover [8]).

Table 2. Taylor Tool Life Constant Values

Cutting Fluid	C	n
Coolant/Lubricant 1	809.3	0.125
Coolant/Lubricant 2	833.5	0.150

The unit cost of production may be calculated using a modified version of one commonly accepted machined work part unit cost equation [6]. This equation—shown in Equation (9)—accounts for three major factors: the costs associated with raw material, time spent by the work part in the machine tool, and disposable tooling.

$$C_{pc} = C_m + C_{MT} + C_{DT} \quad (9)$$

where,

C_{pc} = the work part unit cost of production

C_m = raw material cost for one work part

C_{MT} = the cost associated with the time spent by the work part in the machine tool

C_{DT} = the cost, on a per-work part basis, associated with disposable tooling wear

Expanding Equation (9) yields Equation (10):

$$C_{pc} = C_m + C_o \left(\left(\sum_{i=1}^{n_i} T_{m_i} \right) + \frac{R}{r} + n_{tc} T_{tc} \right) + \sum_{i=1}^{n_i} \left[\frac{T_m}{T} \left(\frac{C_{pt}}{1+n_{rs}-a} + (1-a) C_{otr} T_{rs} \right) \right] \quad (10)$$

where,

- C_o = shop rate: the cost per time to operate the production system on a per-machine basis
- T_m = machining time per part
- R = rapid travel distance/work part required
- r = rapid travel rate
- n_{tc} = number of tool changes/work part required
- T_{tc} = time required to perform one tool change
- n_t = number of different cutting tools required to produce the work part
- T = cutting-tool life
- C_{pt} = cost to purchase disposable tool type i
- n_{rs} = number of allowable tool re-conditionings (for re-grindable tooling) or cutting edges (for disposable insert tooling) for tool type i
- a = a factor equal to zero (for re-grindable tooling) or one (for disposable insert tooling)
- C_{otr} = tool room rate: cost/time to operate tool room
- T_{rs} = time required to re-sharpen tool type i

The Taylor Tool Life equation constants C and n are influenced by numerous factors, which may vary stochastically [9]. The concentration and composition of the coolant/lubricant may vary as a result of variability in the initial mixture, particularly in the case of water-soluble oils, where the dilution ratio is typically in the range of 5:1 to 30:1 (water to soluble oil, by volume) [10]; variability in the mixture ratio, due to water evaporation over time; variability in the mixture, due to make-up fluid mixing inconsistencies; variability in the properties of soluble oil attributed to age and time-in-service; and the presence of tramp oil in the fluid. Other factor variations, which have an effect on tool life, include deliberately induced changes in spindle speed (resulting in changes in cutting speed) as well as stochastic variations in work part and cutting-tool material properties. Figure 3 depicts the effect of changes in the Taylor constant C on the unit cost of production.

The type of fluid employed, changes in soluble oil water-to-fluid ratio, and changes in application method each may have an effect on the Taylor Tool Life constant C [8]. As the value of C increases, the unit cost as a function of cutting speed curve becomes slightly elongated along the horizontal (cutting speed) axis. Coolant/lubricant type, concentration, condition, and application method may have a significant effect on the Taylor Tool Life constant n , as well

[11]. A five percent change in cutting fluid concentration alone may result in a change in the value of n of approximately 10.5% or more [12]. Figure 4 depicts the effect of changes in the value of the Taylor constant n on the unit cost of production as a function of cutting speed.

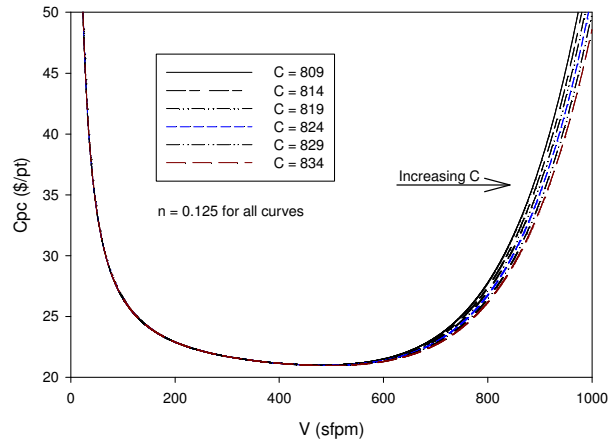


Figure 3. Effect of Increases in the Taylor Tool Life Constant C on Unit Cost as a Function of Cutting Speed ($n = 0.125$)

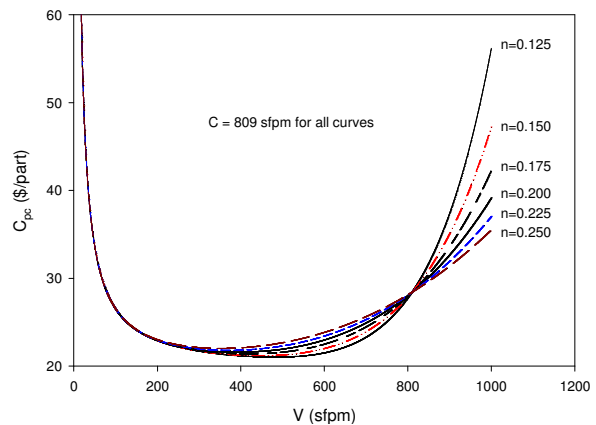


Figure 4. Effect of Increases in the Taylor Tool Life Constant n on Unit Cost as a Function of Cutting Speed ($C = 809$ sfpm)

As the value of the constant n increases, the curve becomes markedly shallower, or more flat. Increases in the value of the constant n have an effect that is similar to decreasing the degrees-of-freedom parameter in a statistical t distribution or increasing the eccentricity of an ellipse. For the purposes of this discussion, the eccentricity analogy will be employed. Since stochastic variations in the coolant/lubricant are inevitable, and since it is also extremely common for machine operators to make adjustments to machining parameters "on the fly", curves with a larger (wider) region in which the slope of the curve is small are preferable to those exhibiting narrower near-zero-slope regions. In practical terms, curves with larger near-zero-slope regions

(i.e., larger values of "eccentricity") depict unit cost functions which are more forgiving with regard to deliberately induced and/or stochastic process variable changes.

Through the appropriate choice of cutting fluid, the effects of fluid and process variability on unit cost may be minimized. Differing combinations of cutting fluid, cutting-tool material, and work material result in differing values of the Taylor constants C and n . Changes in the value of the constant n , in particular, have the potential to minimize the effects of stochastic variation on the unit cost of production of machined work parts. Note that in Figure 4, a point of singularity exists where all curves intersect. This point of singularity occurs where the cutting speed, V , is equal to the Taylor Tool Life constant C . Equation (9) states that the unit cost of production for a machined work part is made up of three elements: the cost of raw material, the cost associated with time spent in the machine tool, and the cost associated with disposable tooling. The cost of raw material, obviously, is not dependent either on cutting speed or on the Taylor constants. The cost of machine time is, then, is given in Equation (11):

$$C_{MT} = C_o \left(\left(\sum_{i=1}^{n_i} T_{m_i} \right) + \frac{R}{r} + n_{tc} T_{tc} \right) \quad (11)$$

where, C_{MT} term is dependent on cutting speed, since machining time is a function of cutting speed but is not dependent on the Taylor constants C and n . The cost associated with disposable tooling is given in Equation (12):

$$C_{DT} = \sum_{i=1}^{n_i} \left[\frac{T_m}{T} \left(\frac{C_{pt}}{1 + n_{rs} - a} + (1 - a) C_{otr} T_{rs} \right) \right]_i \quad (12)$$

where, T_m is a function of cutting speed, while the tool life (T) is dependent on cutting speed as well as the Taylor constants C and n . From Equation (13), the fraction T_m/T , in practical terms, is the proportion of the cutting tool expended to make one work part. When the cutting speed, V , is equal to the Taylor constant C , tool life, T , is equal to one minute.

$$\left. \frac{T_m}{T} \right|_{V=C} = T_m \quad (13)$$

When cutting speed is less than the Taylor constant C , tool life, T , is greater than one minute, as shown Equation (14):

$$\left. \frac{T_m}{T} \right|_{V < C} < T_m \quad (14)$$

When cutting speed is greater than the Taylor constant C , tool life, T , is less than one minute, as shown in Equation (15):

$$\left. \frac{T_m}{T} \right|_{V > C} > T_m \quad (15)$$

At cutting speeds less than C , lower values of n result in somewhat smaller unit costs. At cutting speeds greater than C , larger values of n result in markedly lower unit costs. From a practical perspective, however, the choice of a cutting speed lying to the right of the point of singularity exhibited in Figure 4 is unlikely. In addition, it is worth noting that traditional practice has been to select cutting speeds that lie in the region bounded by the cutting speed, which results in the maximum production rate (V_{maxRp}) and minimum unit cost (V_{minCpc}). Figure 5 depicts these boundaries calculated using the average of the two values of the Taylor constant n ($n = 0.125$ and $n = 0.250$) considered previously.

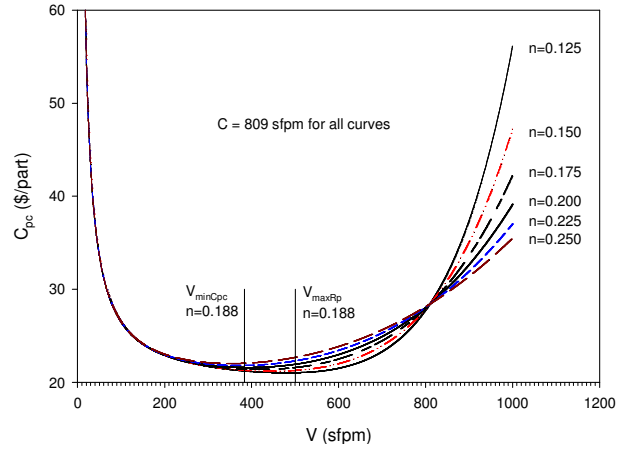


Figure 5. V_{minCpc} and V_{maxRp} with $n = 0.188$

Table 3 details the unit cost incurred at the cutting speed, which results in minimum unit cost (C_{pcVmin}); the unit cost incurred at the cutting speed, which results in maximum production rate (C_{pcVmax}); and the change in unit cost, as cutting speed is increased from V_{minCpc} to V_{maxRp} . Note that as n increases, the change in unit cost, as cutting speed is increased, results in minimum unit cost and maximum production rate (i.e., as n increases, ΔC_{pc} increases). The largest percentage increase in Table 3 is 2.2%, corresponding to a Taylor constant $n = 0.250$. Figure 6 graphically depicts ΔC_{pc} for $n = 0.125$. Over the range of n values considered here, the relationship between n and ΔC_{pc} (as well as n and $\% \Delta C_{pc}$) is essentially linear, as depicted in Figure 7.

Table 3. Change in Unit Cost due to Changes in Cutting Speed at Various Values of the Taylor Constant n

n	$V_{\min C_{pc}}$ (sfpm)	$V_{\max R_p}$ (sfpm)	$C_{pc} V_{\min}$ (\$/part)	$C_{pc} V_{\max}$ (\$/part)	DC_{pc} (\$/part)	$\%DC_{pc}$ (\$/part)
0.125	463	553	16.59	16.74	0.15	0.9%
0.150	428	529	16.77	16.97	0.20	1.2%
0.175	398	509	16.97	17.21	0.24	1.4%
0.188	383	500	17.07	17.34	0.27	1.6%
0.200	371	492	17.17	17.45	0.28	1.7%
0.225	348	478	17.38	17.72	0.34	2.0%
0.250	328	467	17.61	17.99	0.38	2.2%

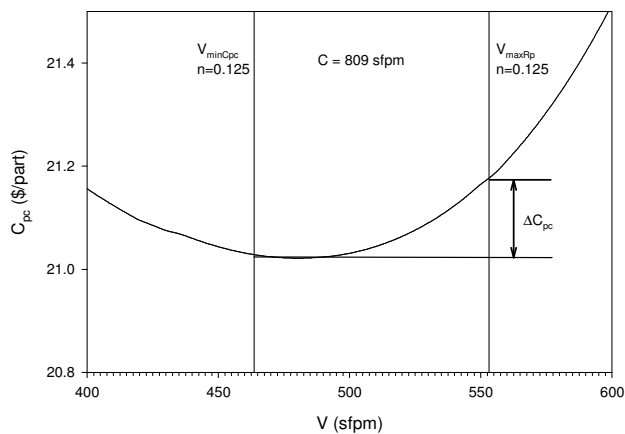


Figure 6. ΔC_{pc} for $n = 0.125$

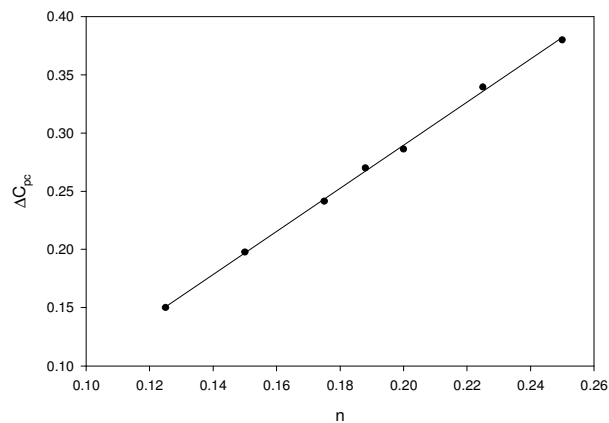


Figure 7. ΔC_{pc} as a Function of the Taylor Constant n

The variation in unit cost due to changes in cutting conditions (specifically, cutting speed) has been of traditional concern [13]. Stochastic changes resulting in differing val-

ues of the Taylor constant n, however, may have an effect on unit cost that is more than twice as large as that resulting from changes in cutting conditions. If there is reason to believe that the Taylor constant n has a value that lies between 0.125 and 0.250, then there may be reason to assign a value for n of 0.188 as "most likely". If the process is operated at a cutting speed of 383 sfpm ($V_{\min C_{pc}}$ for $n=0.188$), and if the "true" value of n is 0.125, then the unit cost of production is evaluated as \$16.79. If, on the other hand, the actual value of n is 0.250, then the unit cost of production is evaluated to \$17.62. This variation represents a $\Delta C_{pc} = \$0.83$ per part, and a $\% \Delta C_{pc} = 4.9\%$. Figure 8 depicts this situation graphically.

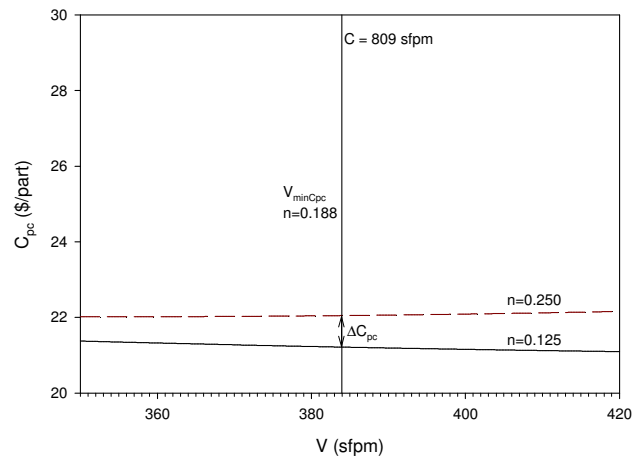


Figure 8. ΔC_{pc} , $n V = 383$ sfpm, n Varying from 0.125 to 0.250

At a cutting speed of 500 sfpm ($V_{\max R_p}$ for $n=0.188$), as n varies from 0.125 to 0.250, $\Delta C_{pc} = \$1.66$ per part and $\% \Delta C_{pc} = 10\%$. This variation in unit cost is approximately 4.5 times greater than that associated with a cutting speed variation from $V_{\min C_{pc}}$ to $V_{\max R_p}$ with n held constant at 0.250.

Conclusions

The properties of coolants/lubricants, and specifically those of water-based soluble oil solutions employed in machining operations, vary stochastically due to variability in the initial mixture ratio, variability in the mixture ratio as a result of water evaporation over time, variability in the mixture due to make-up fluid mixing inconsistencies, variability in the properties of soluble oil attributed to age and time-in-service, and the presence of tramp oil in the fluid. These stochastic variations result in variability in the values of the Taylor Tool Life equation constants C and n.

The effect of variations in the Taylor constant C on the unit cost of production of machined work parts is relatively small, particularly if cutting speeds are maintained in the

range $V_{\min Cpc} \leq V \leq V_{\max Rp}$. The effect of variations in the value of the Taylor constant n , however, may be relatively large. Traditionally, analyses of unit cost variation have been focused on the effect of variations in the cutting speed. For the work part, cutting tool, and cutting conditions analyzed in this paper, the effect of stochastic variations in coolant/lubricant properties may result in an increase in unit cost between 2 and 4.5 times greater than that associated with variations in cutting speed. As a result, it is permissible to conclude that stochastic coolant/lubricant property variations have significantly larger effects on unit cost than cutting speed variations.

In summary:

- The properties of the coolants/lubricants employed in machining operations vary stochastically.
- These stochastic variations result in varying values of the constants C and n , which appear in the Taylor Tool Life equation.
- The effect of variations in the Taylor constant C on unit cost is relatively small.
- The effect of variations in the Taylor constant n on unit cost may be large.

In this paper, the authors quantified the variation in unit cost due to variations in fluid properties for a sample workpart/process combination. The results of this analysis showed that cutting fluid condition may have a much larger effect on unit cost than cutting speed, which has been the traditional parameter of concern. Future work will investigate the applicability of this current approach on different materials, tools, and coolants.

References

- [1] Ezugwu, E. O., Bonney, J., & Olajire, K. A. (2002). The Effect of Coolant Concentration on the Machinability of Nickel-Base, C-263 Alloy, *Proceedings of the 6th International Tribology Conference*, (pp. 515-520). Perth, Western Australia.
- [2] McClure, T., Adams, R., & Gugger, M. (2004). *Comparison of Flood vs. Microlubrication on Machining Performance*. Unpublished manuscript, UNIST, Inc., Grand Rapids, MI.
- [3] Koren, Y., Tsu-Ren, K., & Ulsoy, A. (1991). Flank Wear Estimation under Varying Cutting Conditions. *Journal of Dynamic Systems, Measurement, and Control*, 113(2), 300-307.
- [4] Gilbert, W. W. (1950). *Economics of Machining: In Machining – Theory and Practice* (pp. 476–480). Cleveland, OH: American Society for Metals.
- [5] Isik, Y. (2010). An Experimental Investigation on Effect of Cutting Fluids in Turning with Coated Carbides Tool. *Journal of Mechanical Engineering* 56 (3), 195-201.
- [6] Lee, S. S. (2011). Tool-Condition Monitoring in CNC Turning Operations: A Statistical Approach for Quick Implementation. *International Journal of Modern Engineering*, 11(2), 37-46.
- [7] Zhang, J. Z., Rao, P.N., & Eckman, M. (2012). Experimental Evaluation of a Bio-Based Cutting Fluid Using Multiple Machining Characteristics. *International Journal of Modern Engineering*, 12(2), 35-44.
- [8] Groover, M. P. (2010). *Fundamentals of Modern Manufacturing: Materials, Processes, and Systems*. (4th ed.). Wiley.
- [9] Lee, S. S. (2010). Tool Condition Monitoring System in Turning Operation Utilizing Wavelet Signal Processing and Multi-Learning ANNS Algorithm Methodology. *International Journal of Engineering Research & Innovation*, 2(1), 49-55.
- [10] Iowa Waste Reduction Center. (2003). *Cutting Fluid Management for Small Machining Operations* (p. 20). (3rd ed.). Cedar Falls, IA: University of Northern Iowa.
- [11] Davim, J. P. (Ed.). (2008). *Machining: Fundamentals and Recent Advances*. London: Springer Science & Business Media.
- [12] Sales, W. F., Diniz, A. E., & Machado, A. R. (2001). Application of Cutting Fluids in Machining Processes. *Journal of the Brazilian Society of Mechanical Sciences*, 23(2).
- [13] Thamma, R. (2010). Comparison of Regression Models to Study Effect of Turning Parameters on the Surface Roughness. *International Journal of Engineering Research and Innovation*, 2(2), 80-86.

Biographies

KEVIN M. HUBBARD is an Assistant Professor of Technology and Construction Management at Missouri State University. He earned his B.S. degree (Aerospace Engineering, 1991) from the University of Missouri–Rolla; M.S. (Engineering Management, 1993) from the University of Missouri–Rolla; and Ph.D. from the University of Missouri–Rolla (Engineering Management, 1996). Dr. Hubbard is currently teaching at Missouri State University. His interests are in automation and device control, manufacturing systems, device design, and process optimization. Dr. Hubbard may be reached at KHubbard@MissouriState.edu

MARTIN P. JONES is an Associate Professor of Technology and Construction Management at Missouri State University. He earned his B.S. degree (Physics, 1981) from

the University of Maryland; M.S. (Materials Science & Engineering, 1984) from the Johns Hopkins University; and Ph.D. (Materials Science & Engineering, 1987) from the Johns Hopkins University. Dr. Jones is currently teaching at Missouri State University. His interests are in scanner technology, nondestructive evaluation, manufacturing processes, and quality assurance. Dr. Jones may be reached at MartinJones@MissouriState.edu

RICHARD N. CALLAHAN is Department Head and a Professor of Technology and Construction Management at Missouri State University. He earned his B.S. degree (Engineering Management, 1988) from the University of Missouri–Rolla; M.S. (Engineering Management, 1992) from the University of Missouri–Rolla; and Ph.D. (Engineering Management, 1999) from the University of Missouri–Rolla. Dr. Callahan is currently teaching at Missouri State University. His interests are in project management, process optimization, and manufacturing systems. Dr. Callahan may be reached at NealCallahan@MissouriState.edu

EFFECTS OF ELEVATED TEMPERATURES ON BOND STRENGTH BETWEEN EPOXY-COATED REINFORCEMENT AND FIBER-REINFORCED CONCRETE

José A. Peña, Purdue University Calumet; Drew Oppenhuis, Purdue University Calumet

Abstract

The bonding strength between fiber-reinforced concrete and steel reinforcing bars subjected to elevated temperatures has been studied by several researchers. The use of epoxy-coated reinforcing bars has become commonplace in construction over the last 20 years. The use of epoxy-coated bars helps to increase the durability of reinforced concrete when the concrete structure is located in harsh environments. However, the effect of an epoxy coating on the bonding strength between the reinforcement and the concrete when the structure has been subjected to high temperatures has not been studied. In this current research study, the authors investigated the bonding strength between 20-mm-diameter, epoxy-coated steel bars and concrete subjected to temperatures in the range of 350 °C to 700 °C. Forty modified pullout specimens were prepared using high-strength concrete containing trap rock, sand aggregate, and different volumetric mixtures of two different fibers (hooked steel fibers, and high-modulus polypropylene fibers). The concrete was cured for 28 days under high-humidity conditions at room temperature. Selected specimens were subjected to the indicated range of elevated temperatures using a furnace. Specimens designated for control were kept at room temperature. All specimens were subjected to pullout testing up to failure. The conditions, cracking and strength of both the control and heat-treated specimens, were observed and recorded. The results and analyses are presented in this paper.

Introduction

Concrete is a rock-like material produced by mixing cement, aggregates, admixtures, and water [1]. The aggregates in concrete consist of a mass of particles such as crushed stone, gravel, and sand, although some other types of aggregates have been used in the manufacture of concrete. Concrete is known for its high compressive strength but it is very weak in tension; therefore, concrete is usually reinforced with steel bars (rebars) to prevent failure due to tensile stresses. In the resulting material, the rebars resist the tensile stresses, while the concrete resists the compressive stresses [2]. Rebars are produced in different diameters commonly formed from carbon steel with surface ribs to

help them bond tightly to the concrete. The bond between the rebar and the concrete must be such that the transmission of stresses and the working of the two structural materials as a unit is ensured. The bond between steel and concrete depends on several factors, among them: the age of the concrete and the environment to which it is exposed.

Elements of reinforced concrete may be exposed to harsh environments that could lead to corrosion of steel and deterioration of the structure. Diffusion of deleterious substances into the concrete may produce changes in the internal concrete environment, leading to rupture of the passive layer protecting the steel [3]. If the passive layer breaks the steel will corrode. Corrosion on steel embedded in concrete will occur in the form of rust. Corrosion products are known to have a larger volume than the original steel, which introduces internal tensile stresses in the concrete, producing cracking and leading to spalling and further deterioration [3], [4]. Furthermore, the formation of rust will cause loss in bond strength between the steel and the concrete, resulting in a loss of overall strength capacity. Although concrete can achieve high compressive strength, it is a brittle material. Previous studies [5-8] have shown that the inclusion of fibers within the concrete matrix can significantly increase the capacity of the concrete to resist impact as well as increase its tensile and flexural strength. The introduction of fibers into the concrete mix helps improve other mechanical properties such as resistance to fatigue, thermal shock, and spalling [8-12]. The effect of introducing fibers into the concrete mixes has been extensively reported in the literature [5-12].

In situations where the steel reinforcement may be in danger of corrosion, epoxy-coated rebar can be used. Though the epoxy coating protects against steel corrosion, its bond strength with the concrete has been shown to be much lower than uncoated or galvanized steel rebar. As shown by test results on the bond strength of both epoxy-coated and galvanized rebars reported by the American Galvanized Association [13], the epoxy coating reduced the bond strength to about 85 percent of uncoated rebars and pullout failure occurred at only 65 percent of the bond strength when failure occurred by splitting. This fact leads to conclude that when corrosion is not an issue, uncoated rebar would provide better tensile strength.

In some structural concrete applications, it is necessary to determine the effect of fire on the mechanical properties of the reinforced concrete elements and the performance of the constituent materials; namely, concrete and steel, as well as the materials that make up the concrete itself. Knowledge on the behavior of steel subjected to high temperatures is quite broad. There is also extensive information on research performed on the effects of temperature on concrete [14-18]. Elevated temperatures affect both the aggregates and the cement paste with physical and chemical changes in the material as temperature increases [14]. When concrete is subjected to elevated temperatures, evaporation of free water first, and bound water later, produces shrinkage of the cement paste, while expansion of aggregate size takes place producing differential strain within the concrete structure. The magnitude of aggregate expansion depends on the type and amount of aggregate used in the mix. The strain will eventually produce cracking after transient creep has occurred [17].

Structural concrete elements built for steel manufacturing plants may be subjected to both harsh environments, where epoxy-coated bars would be recommended, and to elevated temperatures—not necessarily produced by unintentional fire—which will affect the stress-carrying capacity of the structural element. The effect of elevated temperature on the bond between the steel reinforcement and concrete at regular and high temperatures has been addressed by other researchers [18-20]. This current investigation addressed the effects of high temperatures on the bond between epoxy-coated steel reinforcement and fiber reinforced concrete.

The mechanical properties of concrete and rebars were affected by elevated temperatures producing a decrease in the stress-carrying capacity of both and of the reinforced concrete as a whole [20]. The results of these tests will help to predict the residual strength of concrete with epoxy-coated rebars and fibers that have been exposed to high temperatures. Having this information available will aid in the design of reinforced concrete that may be subjected to fire or some other source of extreme heat. The better reinforced concrete is designed, the higher residual strength it will have, which also results in improved durability.

Materials and Experimental Procedure

Four different concrete mixtures were prepared. Specimens were built to test the bond strength of fiber-reinforced concrete and epoxy-coated steel reinforcement after being subjected to extreme temperatures. Reinforcing fibers were used since they have shown to improved tensile strength and

thermal shock resistance of concrete. Specimens to test the compressive strength as quality control of the concrete mixes were also prepared. Ten concrete cylinders, four inches in diameter and eight inches in height, were prepared for compression testing and ten concrete pullout specimens were prepared for pullout testing for each mix. Compressive strength testing was performed following ASTM C39/C39M Standard Test Method for Compressive Strength of Cylindrical Concrete Specimens [21].

Aggregates

The coarse aggregate used in this study was crushed trap rock with a maximum size of 0.75 inches (19 mm). The fine aggregate used was standard sand having a maximum size of 0.187 inches (4.75mm). All aggregates were used under saturated surface-dry (SSD) conditions. Characterization of all aggregates was performed following ASTM C29 [22], ASTM C127 [23], ASTM C128 [24], and ASTM C136 [25] standards. Results from tests performed according to these standards are shown in Table 1. The particle size distribution for both aggregates is shown in Figure 1.

Table 1. Aggregate Characterization

	Coarse Aggregate	Fine Aggregate
Bulk Specific Gravity	2.59	2.61
Apparent Specific Gravity	2.61	2.67
Absorption (%)	0.37	2.42
Bulk Unit Weight (lb/ft ³)	105.7	64.2
Fineness Modulus	3.1	2.58

Concrete Mixes

The concrete mixes consisted of: a control mix with no fiber reinforcement, a mix with homopolymer propylene fibers, a mix with steel fibers and a mix using half homopolymer propylene fibers and half steel fibers. The specific quantities of ingredients in each concrete mixture are shown on Table 2. Portland cement type I was used for all concrete mixtures. A water reducer (glenium®) was used in all mixes. The propylene fibers used were Propex® Concrete Systems' *Fibermesh 150*. The steel fibers used were Propex Concrete Systems *Novocon XR*. The amount of *Novocon XR* and *Fibermesh 150* fibers were determined according to application rates recommended by Propex Concrete Systems.

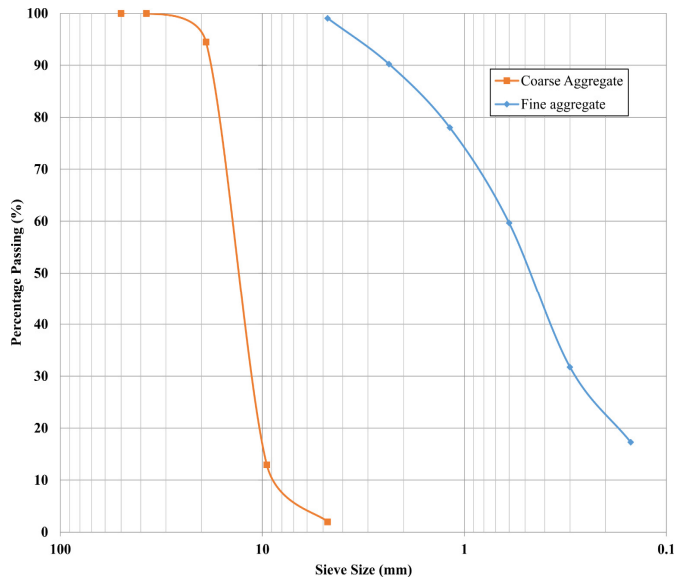


Figure 1. Particle Size Distribution for Coarse and Fine Aggregates

Table 2. Proportions of Concrete Mix Ingredients

Ingredients	Mix 1	Mix 2	Mix 3	Mix 4
Cement (lb)	28.34	28.34	28.34	28.34
Water (lb)	74.92	74.92	74.92	74.92
Coarse Aggr. (lb)	95.26	95.26	95.26	95.26
Fine Aggr. (lb)	101.7	101.7	101.7	101.7
<i>Fibermesh 150</i>	0	0.67	0	0.33
<i>Novocon XR</i>	0	0	16.67	8.33
Glenium (fl oz)	5.75	5.75	5.75	5.75

Pullout Specimens

Pullout specimens were built to those proposed by Chapman and Shah [26] and used by Haddad and Shannis [18]. Custom wooden forms with a cross-section of four inches by four inches were built using 3/4-inch-thick smooth sanded plywood. The reinforcing steel consisted of No. 3 and No. 4 hot-rolled Grade 60 deformed steel bars (3/8-inch and 1/2-inch diameters). The 3/8-inch-diameter rebars were uncoated since their function was to be fixed in the corners of the specimens to prevent tensile failure of the concrete prior to bond failure between the concrete and the epoxy coated bar. A 4-inch by 4-inch square, 1/2-inch-thick steel spacer was used to hold the reinforcing bars in place during pouring

(see Figures 2 and 3). A 1/2-inch-diameter epoxy-coated bar was placed in the center of the specimen. Two 1/2-inch plastic spacers were used to delimit the embedment length of the epoxy-coated rebar to six inches. On the opposite side of the spacer, a 5/8-inch-diameter hexagonal bolt fixed in the center of the cross-section of the mold was used to allow holding of the specimen by the testing machine. A Tinius-Olsen machine was used for tensile testing. This specimen design ensured a uniform distribution of shearing stress along the interface between the epoxy-coated rebar to be pulled out and the concrete.



Figure 2. Steel Spacer and Rebar Cage Reinforcement for Pullout Specimen

Mixing

The mixing procedure followed the ASTM C192 standard Practice for making and Curing Concrete Test Specimens in the Laboratory [27]. The wooden forms were coated with oil before the steel reinforcement was placed and the concrete was poured. The same amount of plasticizer (glenium®) was used in all mixes to increase workability and avoid segregation and bleeding. Slump tests were performed following the ASTM C143 Standard Test Method for Slump of Hydraulic Cement Concrete [28]. The concrete specimens (see Figure 4) were taken out of the molds 24 hours after casting and placed in a 100% humidity curing chamber.

Heat Treatment

The pullout specimens designated for heat treatment were subjected to temperatures of 350, 500, 600, and 700 °C for two hours using an electrical furnace after 28 days of cur-

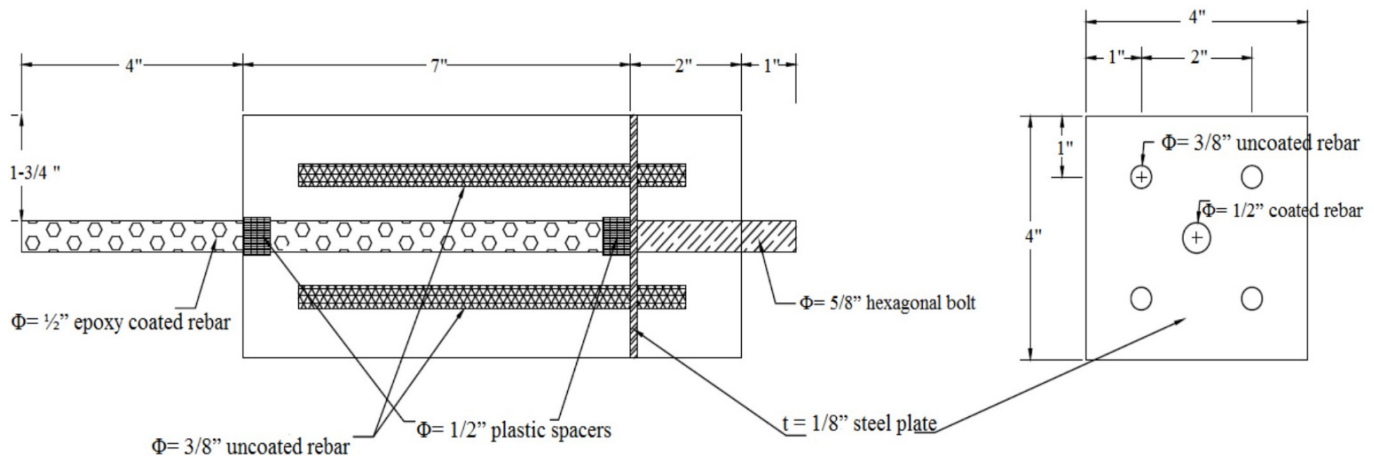


Figure 3. Pullout Specimen and Steel Spacer Diagram

ing. Duplicated specimens were subjected to the designated temperature for each mix. Also, duplicated specimens for the laboratory air for seven days before being subjected to pullout testing. The cracking and spalling of specimens exposed to heat were evaluated by visual inspection and documented before pullout testing took place.



Figure 4. Typical Concrete Pullout Specimen

Pullout Testing

The load-slip relationship for the pullout specimens was obtained by using a Tinius-Olsen testing machine. Pullout testing was performed at a loading rate of 45 lb/s [25]. The pullout loads versus slippage measurements were recorded

and processed in order to obtain the bond stress and strain. The ultimate bond strength of each specimen was also recorded.

Results

Following are the results of the tests performed on the fresh concrete and hardened concrete. Results for testing of fresh concrete mixes consisted of the slump tests, as an indication of workability of the mixes being similar. Results of testing in the hardened concrete cylinders consisted of compressive strength and the pullout testing strength. Table 3 and Figure 5 show the results of the slump tests performed on the fresh concrete as an indication of workability. Results for compressive strength at 14 days and 28 days are shown in Table 4 and Figure 6. Results of the bond strength for the four mixes after being subjected to heat treatment as well as the untreated mixes (at 25 °C) are shown in Table 5 and in Figures 7 and 8.

Table 3. Concrete Slump Test Results

Mix	Mix 1	Mix 2	Mix 3	Mix 4
Slump (in.)	9.5	9	9.25	9.25

Discussion

Compressive Strength

The compression strength test results are shown in Table 4 and Figure 6. Mix 3, containing Novocon XR steel fibers,

showed the highest compression strength at both ages, while Mix 2 containing propylene fibers (Fibermesh 150) showed the lowest compressive strength. However, Mix 2 still showed compressive strength greater than 5000 psi in 90% of the specimens tested and an average compressive strength of only 18.6% below the highest average compressive strength of the whole testing program. For Mixes 3 and 4, the presence of fibers indicated a slight improvement of the compressive strength of the mixes, while for Mix 2, a decrease of 17.6% with respect to the average compressive strength of the control, Mix 1, was noted.

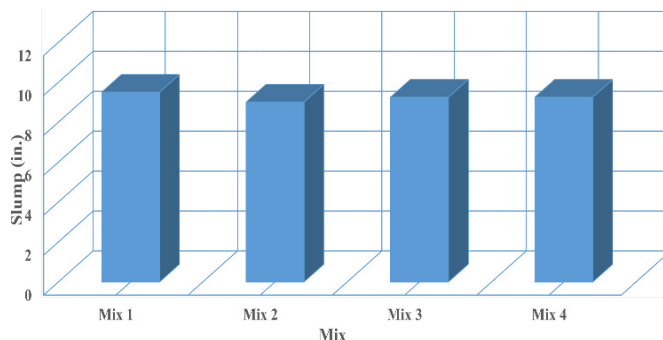


Figure 5. Concrete Slump Test Results

Table 4. Compression Strength of Concrete Mixes

Curing Age		14 Days					28 Days				
Specimen No.		1	2	3	4	5	1	2	3	4	5
Mix 1 Control	Ultimate Load (lb)	78900	67800	90600	86400	75100	89100	102300	98700	100800	76100
	Compression Strength (psi)	78900	67800	90600	86400	75100	7088.3	8138.4	7852.0	8019.1	6054.1
Mix 2	Ultimate Load (lb)	78900	67800	90600	86400	75100	74900	75000	76100	79000	79900
	Compression Strength (psi)	78900	67800	90600	86400	75100	5958.6	5966.6	6054.1	6284.8	6356.4
Mix 3	Ultimate Load (lb)	78900	67800	90600	86400	75100	94100	99400	79400	104400	95400
	Compression Strength (psi)	78900	67800	90600	86400	75100	7486.1	7907.7	6316.6	8305.5	7589.5
Mix 4	Ultimate Load (lb)	78900	67800	90600	86400	75100	83000	78600	72900	83800	76400
	Compression Strength (psi)	78900	67800	90600	86400	75100	6603.0	6253.0	5799.5	6666.7	6078.0

Table 5. Ultimate Load and Bond Strength of Concrete Pullout Specimens

		Mix 1 Control		Mix 2		Mix 3		Mix 4	
Designated Temperature	Specimen No.	Ultimate Load (lbf)	Bond Strength (psi)						
Room Temperature	1	5230	555.2	9400	997.9	9530	1011.7	7180	762.2
	2	5570	591.3	8230	873.7	6880	730.4	4860	515.9
350 °C	3	3410	362.0	2800	297.2	5470	580.7	3580	380.0
	4	2830	300.4	2040	216.6	4720	501.1	4290	455.4
500 °C	5	1815	192.7	1716	182.2	3280	348.2	2260	239.9
	6	2230	236.7	1633	173.4	3150	334.4	3130	332.3
600 °C	7	1457	154.7	1453	154.2	2650	281.3	2070	219.7
	8	1638	173.9	1277	135.6	2410	255.8	1900	201.7
700 °C	9	1233	130.9	652	69.2	2230	236.7	728	77.3
	10	925	98.2	132	14.0	2150	228.2	956	101.5

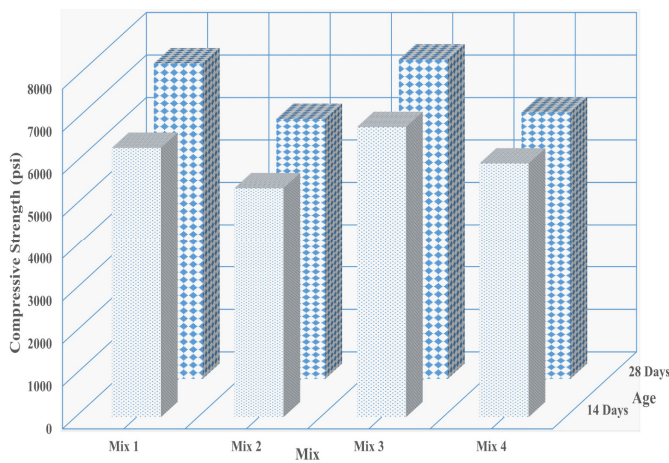


Figure 6. Compressive Strength of Concrete Mixes

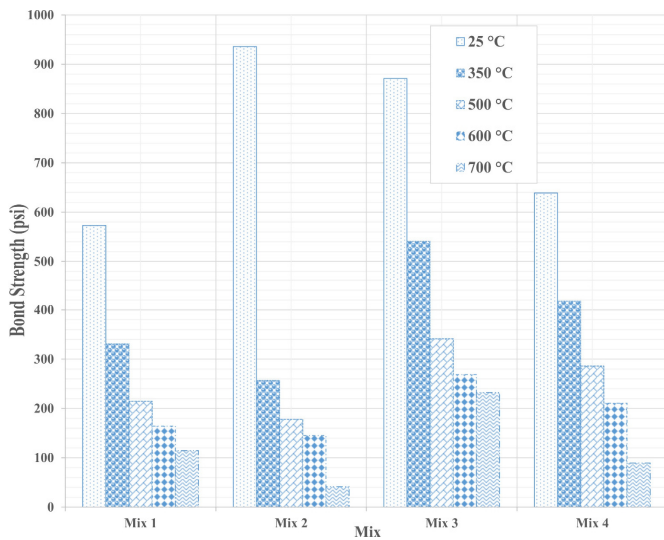


Figure 7. Bond Strength versus Mix Design

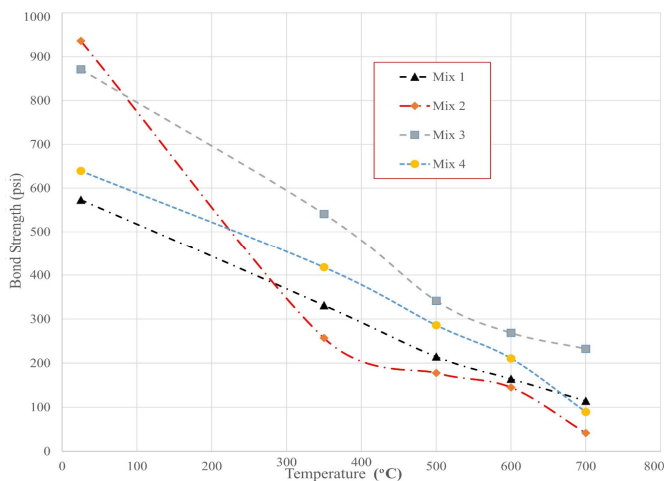


Figure 8. Bond Strength versus Temperature

Damage of Concrete Due to Heat

The damage of the concrete specimens due to heat exposure was documented and visually evaluated. The difference in the amount and size of cracks on specimens from different mixes was slight. For the control mix, it was observed that at 350 °C the concrete specimens color turned darker and formed a few small cracks on the surface. As the heat treatment temperature increased, the amount and size of the cracks increased, with spalling being noticeable at the two highest levels of heat treatment (see Figure 9). Previous studies have indicated the detrimental effects of increased temperature on concrete. Elevated temperatures cause physicochemical changes in the cement paste and the aggregates and thermal incompatibility between aggregate and cement paste leading to a decrease in strength and explosive spalling [14], [17-20]. It has been reported that up to about 100 °C a series of hydrothermal reactions occur within the concrete matrix, resulting in a loss of free, adsorbed, and chemically bonded water and an increase in permeability. The severity of spalling after being subjected to high temperatures depends on the type of aggregate, quality of concrete, moisture content, and permeability of the concrete. Around 300 °C, permanent strength loss begins and dehydration of fine aggregate may take place.



Figure 9. Control Mix Pullout Specimen after Being Subjected to 700 °C

Expansion of aggregate and, at the same time, shrinkage of the cement paste would introduce internal stresses and subsequent cracking with calcium hydroxide dissociation and calcium carbonate dissociating at around 700 °C [14]. Khoury [14] and Khoury et al. [17] reported an increase in creep in both cement pastes and concrete around 500 °C, with spalling showing at a higher degree as the temperature increases. The control mix with no fiber reinforcement showed the most dramatic behavior, in terms of widespread cracking and their size, consequence of the expansion of concrete beyond the elastic limit, increase in the water vapor in the pore structure, and decomposition of the cement hydration product. In general, all mixes containing fiber reinforcement developed smaller-size cracking. Mix 3 showed slightly less concentration and smaller-size cracking than Mix 2; however, Mix 3 showed more spalling than Mix 2. This behavior is attributed to the presence of the steel fibers in Mix 3, which increased the rate of absorbing heat and producing an expansion of the steel, thereby introducing tensile stresses in the concrete and, as a consequence, the spalling; similar results were reported by Haddad and Shannis [18].

Inspection of the specimens performed after the pullout tests revealed loss of bond between the fibers and concrete, which explains why fibers had only a small effect in reducing cracking caused by heat treatment. The propylene fibers tended to melt and be absorbed into the cement paste, explaining why Mix 2 showed small amounts of spalling, since the melting of the fibers leaves behind voids, which act as expansion chambers, where steam can be stored, decreasing the water vapor pressure and, as a result, decreasing the amount of internal stresses introduced into the pore structure [29].

Rebar Evaluation

Regarding the observation on the bars, as expected, at 350 °C, the epoxy coating on the exposed section of the rebar started to acquire a darker color with the surface getting rougher and the coating getting thinner, as the heat treatment temperature increased (see Figure 10). After the pullout testing, the section of the rebar covered by concrete was also visually inspected and on which deterioration of the epoxy coating was noticed. Figure 10 shows a comparison of bar specimen starting on the left with the control specimen kept at room temperature, and farther to the right showing the rebar of specimen subjected to 700 °C. Jau and Huang [29] reported that the temperature at the center of the concrete specimen subjected to heat continued to increase two to three hours after the fire was stopped, helping to explain the damage occurring on the coating of the covered section of the steel rebars.



Figure 10. Epoxy-Coated Rebars after Heat Treatment and Pullout Tests

Bond Strength

For all mixes, the bond strength between epoxy-coated rebars and concrete decreased as the heat treatment temperature increased (see Table 5 and Figures 7 and 8). As mentioned earlier, the concrete showed losses in strength when subjected to heat. Therefore, the bond strength decreases when the reduction in the compressive strength of the concrete was added to the possible plastic deformation of the steel within the concrete. These effects may be considered individually or together as responsible for the loss of bond strength observed after heat treatment. Similar results were obtained by Haddad and Shannis [18]. Cracking of the heat-treated specimens was inspected before and after pullout testing. During pullout testing, as an increasing load was applied, the cracks that were already formed during the heat-treatment process increased in size, thereby reducing the concrete confinement around the rebar and showing a decrease in the bond strength.

Failure appeared to have occurred first because of the local crushing of concrete at the tips of the bar ribs, followed by the concrete splitting along the steel rebar. All specimens showed splitting failure along the steel rebar and radial cracking on their cross-section. The deterioration of the epoxy coating also appeared to weaken the bond with the surrounding concrete. The deterioration of the epoxy coating most likely created gaps between the steel rebar and the surrounding concrete.

Effect of Fibers on Bond Strength

The addition of fibers to the concrete matrix also had an effect on the residual bond strength of the specimens. Figures 11 and 12 show the results of pullout testing for the four mixes at room temperature. For this case, the bond strength for both the steel fibers and propylene fibers appeared to increase with the epoxy-coated rebar. This is most likely the result of the added tensile strength that the presence of fibers provides to the concrete mix. Similar results were reported by Haddad and Shannis [18].

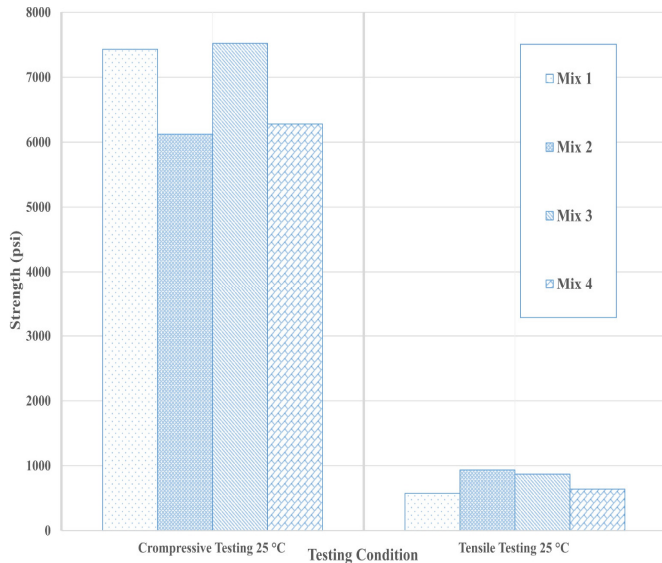


Figure 11. Comparison of Strength (compressive versus tensile) at 25 °C

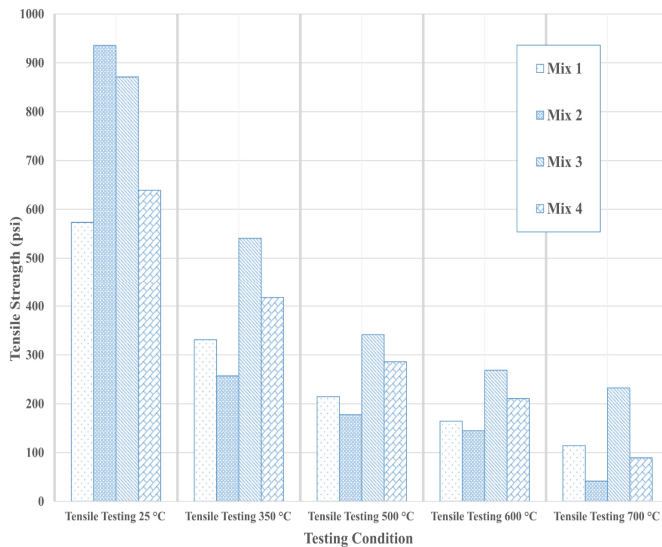


Figure 12. Comparison of Tensile (pullout) Strength for All Mixes

The mixes that included the *Novocon XR* steel fibers had much higher residual strengths during the pullout tests (Figure 12). This behavior is likely the result of the steel fibers limiting the cracking in the concrete caused by heat. Meanwhile, Mix 2, containing *Fibermesh 150* propylene fibers, showed consistently lower residual bond strengths than that of the control mix. These were surprising results because the propylene fibers were shown to limit the amount of damage caused by heat. This loss in bond strength may have been a result of the propylene fibers reacting at high temperatures and weakening the bond between the epoxy-coated rebar and the surrounding concrete. Mix 4, having both steel and propylene fibers, still had consistently higher bond strengths than the control mix at all temperatures.

This was most likely the result of the steel fibers limiting concrete damage caused by heat. This mix was consistently lower at all temperatures than Mix 3 containing steel fibers only. This appears to have been a result of the negative effects the propylene fibers had on the residual bond between epoxy-coated rebar and concrete. In all mixes, as the temperature increased, the residual bond strength decreased. This was most likely a result of the damage caused by heat to the concrete cover. It also may have been caused by the deterioration of the epoxy coating on the steel rebar.

Conclusions

Based on the results of the test program, it can be concluded that:

1. In general, an epoxy coating on the steel reinforcement embedded in concrete will start to show signs of deterioration around 350 °C.
2. The addition of propylene and/or steel fibers to the concrete mix will tend to decrease the cracking and spalling in concrete subjected to high temperatures.
3. The presence of steel fibers in the concrete mix appears to increase the bond strength between epoxy-coated rebars and concrete at all temperatures.
4. The addition of propylene fibers in concrete appears to decrease the bond between epoxy-coated rebars and concrete, when subjected to heat treatment.
5. The higher the temperature, the lower the bond strength between epoxy-coated rebars and concrete. This decrease in strength must be considered when designing slabs in the steel manufacturing industry that may be subjected to both harsh corrosive environments and elevated temperatures.

References

- [1] Mamlouk, M., & Zaniewski, J. (2011). *Materials for Civil and Construction Engineer*. (3rd ed.). Prentice Hall.
- [2] Mindess, S., Francis Young, J., & Darwin, D. (2003). *Concrete*. (2nd ed.). Prentice Hall.
- [3] Tuuti, K. (1995). *Corrosion of Reinforcement: Field and Laboratory Studies for Modelling and Service Life*. University of Lund, Lund Institute of Technology.
- [4] Michel, A., Solgaard, A., Pease, B. J., Geiker, M. R., Stang, H., & Olesen, J. F. (2013). Experimental Investigation of the Relationship between Damage at the Concrete-Steel Interface and Initiation of Reinforcement Corrosion in Plain and Fiber Reinforced Concrete. *Corrosion*, 77, 308-321.
- [5] Mohammadi, Y., Carkon-Azad, R., Singh, S. P., & Kaushik, S. K. (2009). Impact Resistance of Steel Fibrous Concrete Containing Fibers of Mixed Aspect Ratio. *Construction and Building Materials*, 23(1), 183-189.
- [6] Ramakrishna, G., & Sundararajam, T. (2005). Impact Strength of a Few Fiber Reinforced Cement Mortar Slabs: A Comparative Study. *Cement and Concrete Composites*, 27(5), 547-553.
- [7] Alavi Nia, A., Hedayatian, M., Nili, M., & Afrough Sabet, V. (2012). An Experimental and Numerical Study on How Steel and Polypropylene Fibers Affect the Impact Resistance in Fiber-reinforced Concrete. *International Journal of Impact Engineering*, 46, 62-73.
- [8] Zollo, R. F. (1997). Fiber-Reinforced Concrete: An Overview after 30 Years of Development. *Cement and Concrete Composites*, 19(2), 107-122.
- [9] Ding, Y., Azevedo, C., Aguiar, J. B., & Jalali, S. (2012). Study of Residual Behaviour and Flexural Toughness of Fiber Cocktail Reinforced Self Compacting High Performance Concrete after Exposure to High Temperature. *Construction and Building Materials*, 26(1), 21 -31.
- [10] Khaliq, W., & Kodur, V. (2011). Thermal and Mechanical Properties of Fiber Reinforced High Performance Self-Consolidating Concrete at Elevated Temperatures. *Cement and Concrete Research*, 41(11), 1112-1122.
- [11] Carloni, C., Subramaniam, K., Savoia, M., & Rouhi, J. (2012). Experimental Determination of FRP- Concrete Cohesive Interface Properties under Fatigue Loading. *Composite Structures*, 94(4), 1288-1296.
- [12] Zhu, J., Sun, C., Qian, Z., & Chen, J. (2011). The Spalling Strength of Ultra-Fiber Reinforced Cement Mortar. *Engineering Failure Analysis*, 18(7), 1808-1817.
- [13] American Galvanizers Association. (n.d.). In Concrete. Retrieved April 23, 2011, from <http://www.galvanizeit.org/hot-dip-galvanizing/how-long-does-hdg-last/in-concrete>
- [14] Khoury, G. A. (2001). Effect of Fire on Concrete and Concrete Structures. *Progress in Structural Engineering and Materials*, 2(7), 429-447.
- [15] Fletcher, I., Welch, S., Torero, J., Carvel, R., & Usmani, A. (2007). Behaviour of Concrete Structures in Fire. *Thermal Science*, 11(2), 37-52.
- [16] Bilow, D., & Kamara, M. (2008). Fire and Concrete Structures. *Proceedings of the ASCE Conference Structures 2008: Crossing Borders*. Vancouver, Canada.
- [17] Khoury, G. A., Sullivan, P. J. E., & Grainger, B. N. (1985). Strain of Concrete during First Heating to 600°C under Load. *Magazine of Concrete Research*, 37(133), 195-215.
- [18] Haddad, R., & Shannis, L. (2004). Post-Fire Behavior of Bond between High Strength Pozzolanic Concrete and Reinforcing Steel. *Construction Building Materials*, 18(6), 425-435.
- [19] Haddad, R. H., Al-Saleh, R. J., & Al-Akhras, N. M. (2008). Effect of Elevated Temperature on Bond between Reinforcement and Fiber Reinforced Concrete. *Fire Safety Journal*, 43(5), 334-343.
- [20] Alani, F., & Samali, B. (2013). Predicting the Bond Strength between Concrete and Reinforcing Steel at Elevated Temperatures. *Structural Engineering and Mechanics*, 48(5), 643-660.
- [21] ASTM International. (2009). *Standard Test Method for Compressive Strength of Cylindrical Concrete Specimens*. (C39/39M). West Conshohocken, PA.
- [22] ASTM International. (2009). *Standard Test Method for Bulk Density (Unit Weight) and Voids in Aggregate*. (ASTM C29). West Conshohocken, PA.
- [23] ASTM International. (2007). *Standard Test Method for Density, Relative Density (Specific Gravity), and Absorption of Coarse Aggregate*. (ASTM C127). West Conshohocken, PA.
- [24] ASTM International. (2012). *Standard Test Method for Density, Relative Density (Specific Gravity), and Absorption of Fine Aggregate*. (ASTM C128). West Conshohocken, PA.
- [25] ASTM International. (2005). *Standard Test Method for Sieve Analysis of Fine and Coarse Aggregates*. (ASTM C136). West Conshohocken, PA.
- [26] Chapman, R. A., & ad Shah, S. P. (1987). Early Bond Strength in Reinforced Concrete. *ACI Materials Journal*, 84(6), 501-510.

-
- [27] ASTM International. (2007). *Standard Practice for Making and Curing Concrete Test Specimens in the Laboratory*. (ASTM C192). West Conshohocken, PA.
- [28] ASTM International. (2005). *Standard Test Method for Slump of Hydraulic Cement Concrete*. (ASTM C143). West Conshohocken, PA.
- [29] Jau, W., & Huang, K. (2008). A Study of Reinforced Concrete Corner Columns after Fire. *Cement and Concrete Composites*, 30(7), 622-638.

Biographies

JOSÉ A. PEÑA is an Associate Professor of Civil Engineering Technology in the Department of Construction Management and Organizational Leadership at Purdue University Calumet. Dr. Peña may be reached at penaj@purduecal.edu

DREW OPPENHUIS is a graduate student in the Construction Management and Engineering Technologies Department at Purdue University Calumet. Mr. Oppenhuis may be reached at drew.oppenhuis@madisonconstruction.net

A COMPARATIVE STUDY ON THE MICROMACHINING PERFORMANCE OF COPPER, BRASS, AND ALUMINUM

Muhammad P. Jahan, Western Kentucky University; Gregory K. Arbuckle, Western Kentucky University;
Abdulhameed Dawood, Western Kentucky University

Abstract

Besides steel, aluminium, brass, and copper are the three most frequently used engineering materials for various applications. Because of the ease of machinability and excellent mechanical and electrical properties, these materials are extensively used in manufacturing of micro-scale parts and components for the electronics and packaging industries. Micro-milling is the most popular machining process for fabricating micro-parts and components with excellent surface finish and dimensional accuracy. In this study, the authors investigated the micro-machining performance of copper, aluminium, and brass under the micro-milling process based on the machined surface quality at optimum machining speeds. The comparative machining performance study was conducted by machining reverse pyramid-shaped micro-features in all three materials using the same parameter settings. The objective during the trial-and-error experiments was to achieve the highest possible machining speed for different materials without any tool breakage.

In order to compare the performance, a suitable parameter setting was identified at which all three materials could be machined successfully at the maximum possible speed without any tool breakage. The surface quality of the machined slot was evaluated qualitatively, based on the surface finish of the slot, burr formation around the edges of the slots, and presence of any surface defects. The tool surface after machining was also evaluated for differences in tool wear for machining aluminium, copper, and brass. It was found that aluminium and brass could be machined at comparatively higher cutting speeds and depth of cut compared to copper. There was more frequent tool breakage when machining copper at higher speeds and depth of cut, due to the ductility of copper resulting in adhesion of materials around the tool edge. Brass was found to be comparatively easier to machine, due to the smaller chips generated and no visible adhesion to the cutting tool. At the same parameter settings, brass was found to generate a better surface finish with smooth edges and fewer surface defects compared to copper and aluminium. Finally, a feed rate of 30 mm/min, depth of cut of 0.3 mm, and a tool rotational speed of 2800 rpm were found to provide successful machining in three materials without any tool breakage, in addition to providing acceptable surface finish.

Introduction

In recent years, micro-scale devices and components made of different materials have become an integral part of many plastics, electronics, and semiconductor industries. Among the various manufacturing processes, machining is a well-established process used extensively in these industries for fabricating parts and components [1-4]. Micro-milling is one of the sustainable micro-machining processes that are used for manufacturing three-dimensional (3D) features on metals and ceramics [5-9]. Micro-milling is able to produce high material removal rates (MRR) and achieve high-quality surface finishes and dimensional accuracy with a new generation of miniaturized machine tools [9]. Because of the acceptable performance and reputation of mechanical micro-machining, various research studies have been conducted on the micro-milling processes and improvement of productivity in micro-milling. Several researchers have investigated the differences between conventional milling and micro-milling processes in terms of productivity [10], [11].

While conventional milling and micro-milling are operationally the same, the basic and essential differences between these processes are due to scale of operation [10], [11]. Özel et al. [10] evaluated the ratio of feed per tooth to radius of the cutter in both types of milling and concluded that it is much greater in micro-milling than conventional milling. The formation of the burr at the end of a cut is a similar phenomenon to chip formation. Burrs are unwanted because they can affect further assembly operations. Therefore, burrs should be removed in a de-burring process [12]. The burr removal process can be more easily applied to conventional milling than micro-milling. The de-burring process in micro-milling machining is very hard, as burr removal could harm the workpiece. Recently, micro-milling has been miniaturized to as small as 20 μm ; as such, the conventional de-burring process cannot be conveniently applied to the micro-burrs. The scaled-down end mills and conventional machine tools have the same cutter geometries. Lee et al. [12] investigated the size and type of burrs formed in aluminium 6061-T6, stainless steel 304, and copper 110. They looked at five different types of burrs formed during processing such as entrance-side burrs at the down-milling side, top burrs from up- and down-milling, exit burrs at the bottom of the slot, and exit-side burrs at the up-milling side [12]. These kinds of burrs were important in the

micro-milling process, because they could help the investigation of cutting parameters on burr formation.

There have been several research studies on the micro-milling of aluminium, copper, and brass, individually. Chu [13] conducted a series of experiments on micro-milling of aluminium 6061-T6 to study burr formation. He found that large feeds per tooth were responsible for large burrs in the feed direction, and that the cutting speed did not have an effect on burr formation. Mougo et al. [14] investigated the effect of the width of cut on the micro-milling performance of aluminium. They varied the width of cut to identify the influence of the minimum chip thickness on the resultant forces, and reported that width of cut lower than the tool diameter generated lower cutting forces and produced smoother surface finishes with fewer burrs. Liu and Wang [15] developed a new technology, micro-turn-milling, and applied it in the machining of aluminium alloy 2A12. It was reported that the surface roughness of micro-turn-milling was close to micro-turning and the surface profile of up-turn milling was better than that of down-turn milling. Monroy-Vázquez et al. [16] compared the superficial and dimensional quality of micro-features machined in aluminium, titanium alloys, and stainless steel. They reported that the micro-milling process was capable of offering quality features required on the micro-channeled devices. However, they also found that, among the three materials, stainless steel produced better surface quality in terms of burr formation and surface roughness.

Huo and Cheng [11] performed a series of experiments on micro-milling of oxygen-free, high-conductivity copper using tungsten carbide (WC), chemical vapour deposition (CVD) diamond, and single-crystal diamond micro-milling tools of 0.4 mm diameter. The purpose of the research was to study the influence of cutting parameters such as feed rate, cutting speed, and axial depth of cut on burr formation and surface roughness. Those authors reported that the optimal feed rate induced the best surface roughness. Filiz et al. [17] conducted a series of tests on 99.99% pure copper using the micro-milling process. Four feed rates (0.75, 1.5, 3, and 6 $\mu\text{m}/\text{flute}$) and three cutting speeds (40, 80, and 120 m/min) were considered for that study. It was found that the most important parameters in micro-milling were spindle speed, feed rate, and feed per tooth, which have a significant influence on micro-milling machining performance [17]. Prakash et al. [18] evaluated the effects of various parameters: axial depth of cut, cutting speed, and feed rate on tool life and flank wear. They found that feed rate did not influence tool life or flank wear; whereas, the depth of cut and cutting speed were effective on flank wear. Another study was performed by Mayor and Sodemann [19] to identify optimal parameters for maximum tool life. During that

study, the authors used 100 μm end mills necked to 600 μm , with the workpiece under flood-like applications of an oil-based cutting fluid. The axial depth of cut and feed rate were varied with other parameters held constant, including radial depth of cut. The mean and variance calculated for each set of parameters and analysis of variance were performed. The analysis of variance revealed that tool life had a significantly stronger correlation with cutting parameter variations and maximum material removal from a distance or time [19].

Fard and Bordatchev [20] used the micro-milling of brass on ball-end mills to investigate the influence of tool direction on final surface geometry and quality in five-axis micro-milling. According to their findings on final surface geometry, changing the tool orientation can decrease the rubbing of the material at the bottom of the grooves. It was observed that the surface roughness at the bottom of the grooves improved significantly when a tool inclinational angle of 15 degrees was used in micro-milling. Similar findings were reported by the Copper Development Association [21], in which they suggested that the clearance behind the cutting edge should be enough to prevent a rubbing or burnishing action as an overall rule for copper alloys. Typically during micro-milling, having too much rake or clearance angle at high speeds produces extreme vibrations and digging in the workpiece [21]. Liu et al. [22] investigated micro-milling of brass to study the existence of minimum chip thickness. They conducted a comparative study between normal chip volume with different feed rates and brass chips with specific feed rates. They found that for low feed rates, the measured chip volume was much larger than the supposed chip volume, which showed that a chip could not be shaped with each pass of the cutting tooth. They also concluded that the chips were not formed with each pass of the tool. Egashira and Mizutani [23] investigated the micro-scale machinability of brass using both micro-drilling and micro-milling processes with a 10 μm diameter tool. They were able to drill micro-holes of 50 μm and micro-slots of 100 μm (length) x 20 μm (width), and reported that micro-features can be machined successfully in brass using both micro-machining processes.

Although there has been extensive research on the micro-milling of aluminium, brass, and copper, most of those studies have focused on machining performance of a single material. As all three materials are widely used in the micro-milling process, a comparative study on the machining performance of three materials will provide helpful insight and guidelines in the selection of suitable materials for different applications. Therefore, the authors of the current study conducted a comparative experimental investigation on the machining performance of copper, brass, and aluminium for

machining micro-slots. The machining performance was evaluated in terms of machining speed, surface finish of the micro-slots, tool breakage, tool wear, and burr formation. An optimal parameter setting was identified that would provide improved machining performance for all three materials at the highest possible speed with considerably better surface finish and without tool breakage.

Experimental Detail

A desktop micro-milling machine tool from “Denford” was used in this study to perform the experiments. The desktop milling machine was a compact, 3-axis CNC milling machine with totally enclosed interlocking guards. Figure 1 shows a photograph of the MicroMill with its different components. Variable spindle speeds and feed rates make the MicroMill ideal for cutting resistant materials such as wax, plastic, acrylic, aluminium, and free-cutting alloys. The travels of the machine bed in the X, Y, and Z directions were 228 mm, 130 mm, and 160 mm. The maximum values of spindle speed and feed rate were 2800 rpm and 750 mm/min, respectively. In this study, the depth of cut and feed rate were varied, while keeping the spindle speed at its maximum value 2800 rpm. As the higher cutting speed provides faster machining and the rotational speed of this desktop machine was limited, the maximum spindle speed was used. In order to machine copper, brass, and aluminium workpieces, tungsten carbide cutting tools with a diameter of 0.8 mm were used. Table 1 shows the machining conditions used in this study. After machining the micro-slots, the cutting tools were investigated using digital, reflected light, and scanning electron microscopes. Table 2 shows the sets of machining parameters used in this study and the comments on whether they resulted in successful or unsuccessful machining of a pyramid in copper, brass, and aluminium.

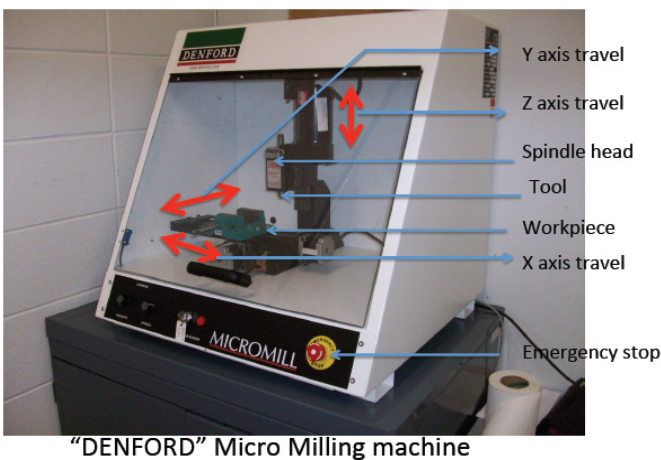


Figure 1. Photograph of the Desktop Micro-milling Machine Used in This Study

Table 1. Machining Conditions Used for Micro-milling of Aluminium, Copper, and Brass

Workpieces	Copper, Brass, Aluminium
Cutting tool	Tungsten Carbide (ϕ 1/32 inch or 0.8 mm)
Coolant	No coolant
Feed rate (mm/min)	20, 30, 40
Depth of cut (mm)	0.2, 0.3, 0.4
Spindle speed (rpm)	2800 (max. capacity)

Table 2. Sets of Machining Parameters Used on a Trial-and-error Basis and Their Outcomes

Run	RPM	Feed Rate	Depth	Cutter	Material	Successful
1	2800	40mm/min	0.4mm	0.8mm	Al	No
2	2800	30mm/min	0.4mm	0.8mm	Al	Yes
3	2800	30mm/min	0.4mm	0.8mm	Cu	No
4	2800	20mm/min	0.2mm	0.8mm	Cu	Yes
5	2800	30mm/min	0.2mm	0.8mm	Cu	Yes
6	2800	20mm/min	0.2mm	0.8mm	Brass	Yes
7	2800	30mm/min	0.2mm	0.8mm	Brass	Yes
8	2800	30mm/min	0.4mm	0.8mm	Brass	Yes
9	2800	40mm/min	0.4mm	0.8mm	Brass	No
10	2800	30mm/min	0.3mm	0.8mm	Brass	Yes
11	2800	30mm/min	0.3mm	0.8mm	Al	Yes
12	2800	30mm/min	0.3mm	0.8mm	Cu	Yes

Results and Discussion

Effect of Operating Parameters

In this study, the experiments were designed on a trial-and-error basis in order to determine a set of machining parameters for successful micro-milling of copper, brass, and aluminium. A reversed pyramid containing four square-shaped micro-channels was designed using CAD with the respective CNC codes generated such that the machine would run automatically. The objective was to identify a set of machining parameters that could successfully machine the materials at possibly higher machining speeds with im-

proved surface finish. For all three materials, the machining conditions providing the highest possible productivity without any tool breakage, as well as the smoothest and most burr-free surface were identified. Table 2 shows the machining conditions of the 12 experimental runs used sequentially to find the most successful and optimum parameter settings for the micro-milling of copper, brass, and aluminium.

The primary objective of this current study was to identify parameters for successful machining of three materials at the highest possible speeds. Therefore, the rotational speed of the tool was set at the maximum capacity of the low-powered desktop micro-milling setup. As can be seen, the experiments started with the selection of the higher settings of depth of cut and feed rate, 0.4 mm and 40 mm/min, respectively. It can also be seen from run numbers 1 and 9 (see Table 2) that the parameter settings of 2800 rpm, 0.4 mm d.o.c., and 40 mm/min were not able to complete the machining of all of the slots successfully in aluminium and brass. Figures 2 and 3 show the optical images of the machined surfaces and cutting tools for machining aluminium and brass using settings of 2800 rpm, 0.4 mm, and 40 mm/min. Each figure includes the image of the target pyramid, a magnified image of the individual micro-slots, and an image of the cutting tool showing tool wear/breakage. It can be seen that the selection of a high depth of cut and feed rate was able to complete three out of four micro-slots successfully in aluminium, compared to two in brass. The topography of the individual slots in aluminium were also found to be better, when compared to those of brass as shown in Figures 2 and 3.

The machined surface of the individual slots in both aluminium and brass workpieces showed feed marks from the cutting tools, in addition to some form of surface defects. The burrs formed around the edge of the slots were found to be very irregular and rough. One common trend was observed in the failure of the cutting tool. For the machining of both aluminium and brass, the cutting tool was found to break in the middle of machining. This suggests that there was some reduction of tool sharpness while machining at the higher feed rate and depth of cut. The chipping from the cutting tool face can be confirmed from both Figures 2 and 3. For both cases, the tool wear mechanism was almost similar.

On the other hand, copper was found to be more difficult to machine, even at lower settings. As can be seen from Figure 4, an experimental run with spindle speed (s.s.) = 2800 rpm, $f = 30$ mm/min, and d.o.c. = 0.4 mm (run #3 in Table 2) was unable to complete the feature with five micro-slots. The cutting tool broke at the middle of the third slot (see Figure 4). Moreover, it can be seen from the image of

the cutting tool that the wear mechanism of the cutting tool was also different for micro-milling of copper compared to that of aluminium and brass. Unlike cutting tool wear for machining aluminium and brass at higher settings of federate and depth of cut, no chipping from the cutting tool surface was observed in the cutting tool during the machining of copper. Instead, the cutting tool became very blunt, thus breaking the cutting tool tip. This was probably due to the higher amount of adhesion of the chips to the tool tip that prohibited the sharper cutting surface to come in contact during machining.

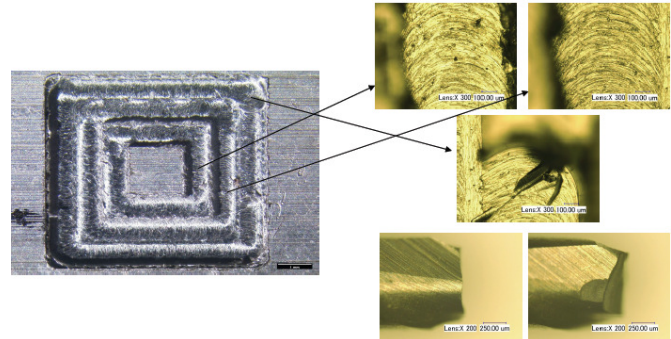


Figure 2. Machining of Aluminium at $f = 40$ mm/min, D.O.C. = 0.4 mm (Run #1 in Table 2): Image of Pyramid Shaped Structure (at left), and the Magnified images of Micro Slots (top right), and Cutting Tool (bottom right)

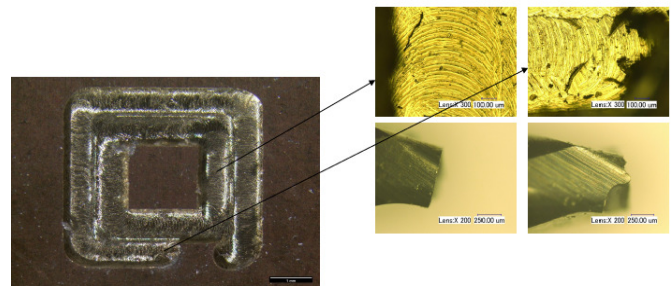


Figure 3. Machining of Brass at $f = 40$ mm/min, D.O.C. = 0.4 mm (Run #9 in Table 2): Pyramid Shaped Structure (at left) and Micro Slots and Cutting Tool (at right)

As copper is known to be very ductile, the heat generated during the dry machining of copper caused the copper chips to get attached to the cutting tool edges. As a result, the sharp cutting edge could not come in contact with the workpiece, resulting in breakage of the cutting tool. In addition, the chips were also found to get attached to the machined surface, due to the high ductility of copper, as can be seen from Figure 4. Besides the burrs at the edges, there was some adhesion of chips on the micro-slot surface for all of the individual slots. The chip analysis described in the following section also supports the adhesion of chips on the cutting tools and machined surface during the machining of copper.

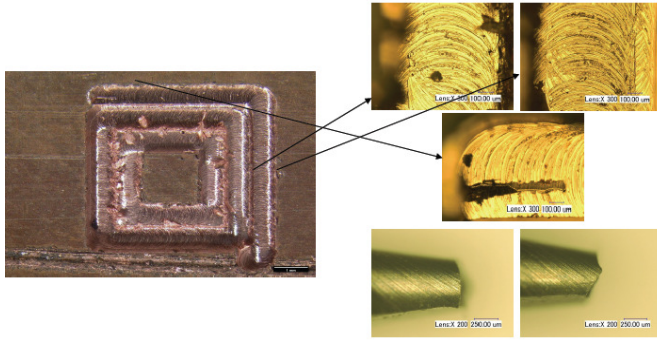


Figure 4. Machining of Copper at $f = 30$ mm/min and D.O.C. = 0.4 mm (Run #3 in Table 2): Pyramid-shaped Structure (at left) and Micro-slots and Cutting Tool (at right)

Although an experimental condition of $s.s. = 2800$ rpm, $f = 30$ mm/min, and $d.o.c. = 0.4$ mm were not able to machine copper successfully, it was able to machine both aluminium and brass without tool failure (see Figures 5 and 6). It can be seen from Figures 5 and 6 that between the two materials, brass provided a comparatively smoother surface on the micro-channels. There was burr formation around the edges of the micro-channels in both the brass and aluminium workpieces. No significant tool wear was observed in the tungsten carbide tool after machining four $5\text{ mm} \times 5\text{ mm}$ square micro-slots in the brass workpiece. On the other hand, some adhesion of chips around the rake face of the cutting tool was observed after machining the same number of micro-slots in aluminium.

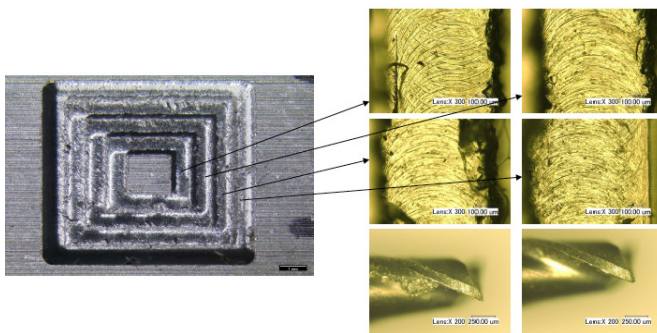


Figure 5. Machining of Aluminium at $f = 30$ mm/min and D.O.C. = 0.4 mm (Run #2 in Table 2): Pyramid Shaped Structure (at left) and Micro Slots and Cutting Tool (at right)

In order to obtain better surface finishes, the feed rate and the depth of cut were reduced to 20 mm/min and 0.2 mm without changing the spindle speed. It was found that the surface quality was improved significantly. It can be seen from Figures 7 and 8 that the machined slots had fewer burrs in both copper and brass. In addition, no significant tool wear was observed for machining both materials at the setting of 2800 rpm, 20 mm/min, and 0.2 mm. Brass produced a smooth and defect-free surface with fewer burrs

around the edges. Although copper produced a comparatively poorer surface finish at 20 mm/min and 0.2 mm, the surface finish improved by increasing the feed rate one step. Figure 9 shows the improved surface finish of the slots, while machining copper at $f = 30$ mm/min and $d.o.c. = 0.2$ mm. On the other hand, increasing the feed rate to 30 mm/min, while keeping depth of cut unchanged at 0.2 mm during machining of brass (see Figure 10), resulted in a slight deterioration of the machined surface. This phenomenon can be explained by copper's higher ductility. Due to the higher ductility of copper, very low feed rates were not able to generate a smoother surface, whereas moderately higher feed rates at a lower depth of cut could generate better surface finishes during micro-machining of copper.

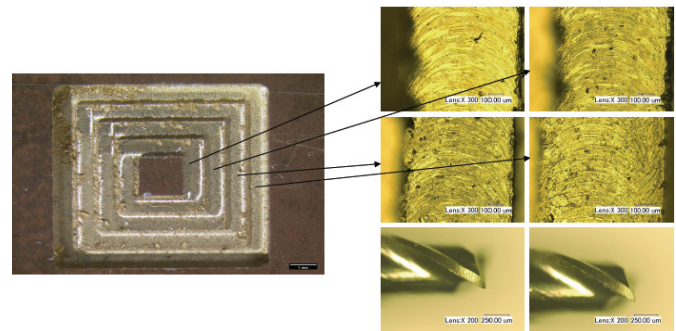


Figure 6. Machining of Brass at $f = 30$ mm/min and D.O.C. = 0.4 mm (Run #8 in Table 2): Pyramid Shaped Structure (at left) Micro Slots and Cutting Tool (at right)

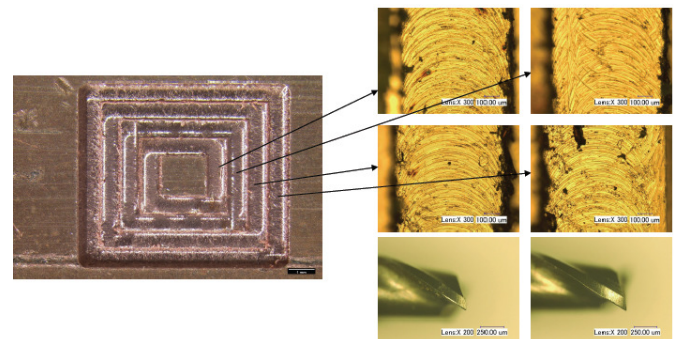


Figure 7. Machining of Copper at $f = 20$ mm/min and D.O.C. = 0.2 mm (Run #4 in Table 2): Pyramid Shaped Structure (at left) Micro Slots and Cutting Tool (at right)

Finally, it was found that all three materials could be machined successfully without any tool failure via any combination of parameters up to a feed rate of 30 mm/min and a depth of cut of 0.3 mm. It was found the surface finish of the micro-slots in copper started to deteriorate at the settings of 2800 rpm, 30 mm/min, and 0.3 mm (see Figure 11), whereas the surface quality of slots were still acceptable in brass and aluminium (see Figures 12 and 13). Therefore,

considering all the performance parameters, a spindle speed of 2800 rpm, $f = 20$ mm/min, and D.O.C. = 0.2 mm were found to be the optimum parameters capable of machining all three materials successfully with less burr formation and a defect-free surface finish. Copper was able to generate slightly better surface finishes at 2800 rpm, $f = 30$ mm/min, and D.O.C. = 0.2 mm, whereas brass and aluminium were found to produce slightly poorer quality surface finishes compared to those produced using the optimum parameters noted above.

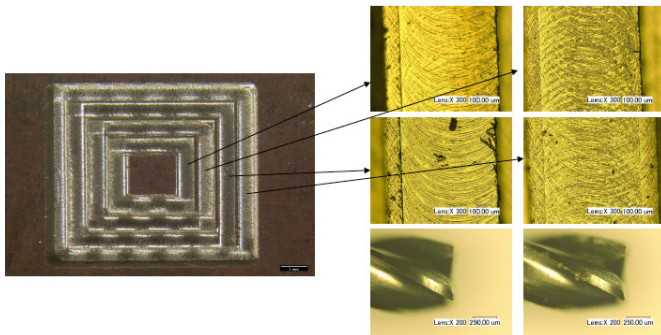


Figure 8. Machining of Brass at $f = 20$ mm/min and D.O.C. = 0.2 mm (Run #6 in Table 2): Pyramid Shaped Structure (at left) and Micro slots and Cutting Tool (at right)

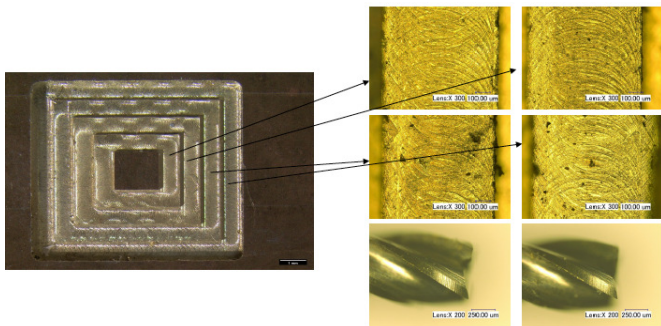


Figure 9. Machining of Brass at $f = 30$ mm/min and D.O.C. = 0.2 mm (Run #7 in Table 2): Pyramid Shaped Structure (at left) and Micro Slots and Cutting Tool (at right)

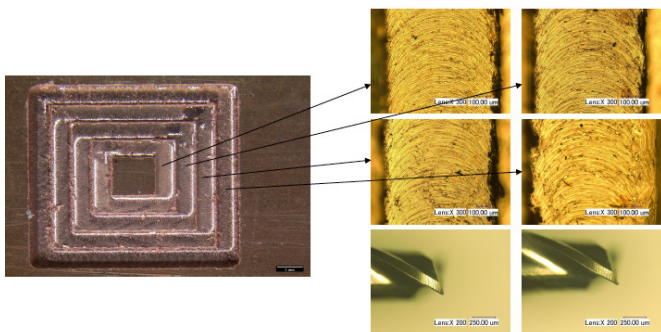


Figure 10. Machining of Copper at $f = 30$ mm/min and D.O.C. = 0.2 mm (Run #5 in Table 2): Pyramid Shaped Structure (at left) and Micro Slots and Cutting Tool (at right)

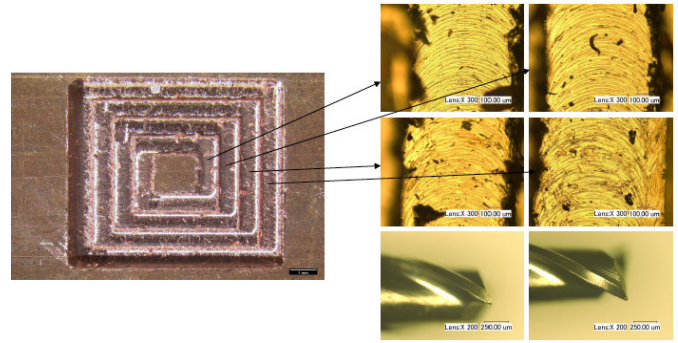


Figure 11. Machining of Copper at $f = 30$ mm/min and D.O.C. = 0.3 mm (Run #12 in Table 2): Pyramid Shaped Structure (at left) and Micro Slots and Cutting Tool (at right)

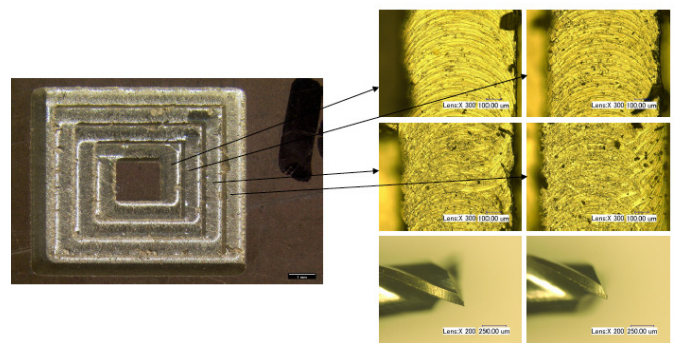


Figure 12. Machining of Brass at $f = 30$ mm/min and D.O.C. = 0.3 mm (Run #10 in Table 2): Pyramid Shaped Structure (at left) and Micro Slots and Cutting Tool (at right)

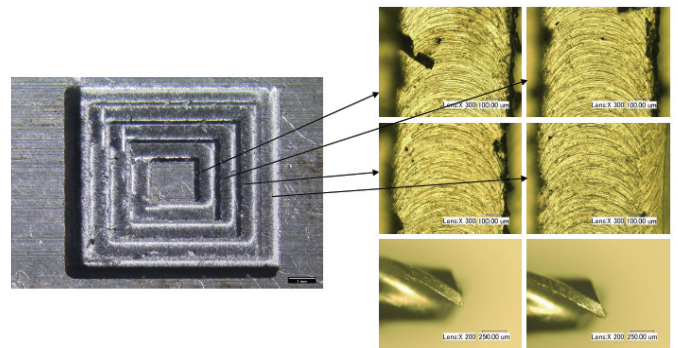


Figure 13. Machining of Aluminium at $f = 30$ mm/min and D.O.C. = 0.3 mm (Run #11 in Table 2): Pyramid Shaped Structure (at left) Micro Slots and Cutting Tool (at right)

Study of Chip Morphology

In this study, the chips were collected at different settings of cutting parameters to investigate the chip morphology and correlation to surface finish and tool wear. It was observed that for almost all settings of parameters, the chips generated during the micro-milling of copper and aluminium

um were continuous type, whereas the chips produced during the machining of brass were mostly discontinuous type. Figure 14 shows the optical images of the chips formed at a tool rotational speed of 2800 rpm, $f = 30$ mm/min, and depth of cut of 0.3 mm. The most important reason for the continuous nature of chips in copper is its ductility. During the dry machining of copper at higher feed rates and depth of cut, a significant amount of heat was generated, due to the friction between cutting tool and workpiece surface. Due to this heat, the copper became more ductile, thus promoting the continuous chips with the travel of cutting tool along a path.

However, as more and more continuous chips were formed, they tended to attach to the cutting tool edge, due to the heat generated during the machining process. As a result, the sharp edges of the cutting tools could not come in contact with the workpiece surface, resulting in digging and rubbing actions rather than cutting. The rubbing and digging action of the cutting tool resulted in significant tool wear and/or tool breakage. This is why copper was found to be the most difficult material to cut in micro-milling using higher cutting speeds, feed rate, and depth of cut. On the other hand, discontinuous nature of chips during the micro-milling of brass made it suitable for successful machining at comparatively higher machining speeds.

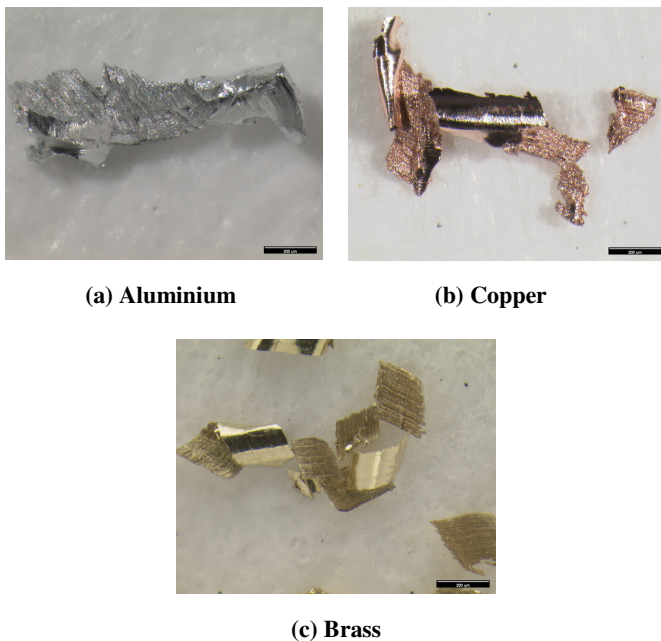


Figure 14. Optical Images of Chips Generated in Different Materials, while Machining at a Parameter Setting of Spindle Speed of 2800 rpm, $f = 30$ mm/min, and Depth of Cut of 0.3 mm

The chip morphology was also found to be influenced by the depth of cut. It was found that the continuity of the chips decreased with a reduction in the depth of cut, thereby reducing the chance of chip adhesion to the cutting tool. As a result, premature tool failure was significantly reduced at lower settings of depth of cut. With the reduction of the depth of cut, the chip became less continuous for all three materials. Although the chips formed in copper and aluminium were still found to be continuous, as can be seen in Figure 15, the adhesion of chips to the cutting tool was not common at reduced settings of depth of cut.

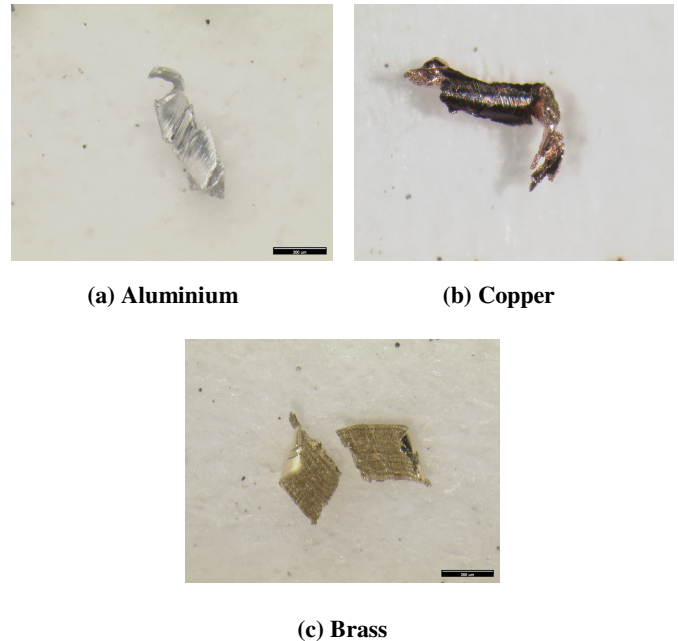


Figure 15. Optical Images of Chips Generated in Different Materials at a Spindle Speed of 2800 rpm, $f = 20$ mm/min, and Depth of Cut of 0.2 mm

Conclusions

The following conclusions can be drawn from this experimental study of the micro-milling of copper, brass, and aluminium:

- Among the three different materials, brass produced the best surface finish, followed by aluminium and copper at the same parameter settings. Copper was able to produce comparable surface finishes at comparatively lower machining speeds, feed rates, and depth of cut.
- Brass was found to be more easily machined by maintaining improved surface finish at comparatively higher cutting speeds and depth of cut. Brass showed

good machinability in micro-milling, due to its discontinuous chip formation and minimum adhesion to the tool.

- Copper was found to be comparatively difficult to machine by micro-milling, due to the buildup of chips and adhesion of chips to the tool edges. The higher ductility of copper was found to be responsible for the poor machinability of copper.
- Tool wear and, hence, tool breakage increased with the increase of cutting speed and depth of cut for all three materials. With the increase of depth of cut and feed rate, more rubbing or digging action took place rather than cutting, resulting in more frequent tool breakage.
- The chips became more continuous at higher depth of cut for all three materials, increasing the chance of adhesion to the edge of the cutting tools. The adhesion phenomenon prohibited the sharp rake surfaces to come in contact with the workpiece, thereby increasing premature tool failure.
- The chip morphology analysis suggests that brass produces discontinuous types of chips during the micro-milling operation, making it better than copper and aluminum. However, by selecting appropriate machining parameters, copper and aluminum can also be machined with comparable surface finishes.

Future Research

This research provides useful information in the field of mechanical micro-machining and opens up the field for more extensive and in-depth research on micro- and nano-scale machining of these three materials. Future research should focus on the modelling of cutting forces for micro-milling of brass, copper, and aluminium and establish the co-relationship with this experimental investigation. An in-depth analysis of the findings of this study should be conducted by investigating the changes of materials at the atomic and molecular levels. The study of molecular structural changes of materials before and after machining could explain the machinability of the materials. In addition, the mechanical property changes of the materials at the micro- and nano-scale, due to machining, should also be investigated in future studies.

Acknowledgment

The authors would like to acknowledge Dr. John Andersland of the Biology department for his support with the microscopy facilities. The authors would also like to acknowledge the partial support via an internal grant from WKU: RCAP 1 Award #: 13-8044.

References

- [1] Gittens, A., & Chowdary, B. V. (2007). A Study on Machining of Sculptured Surfaces, *International Journal of Modern Engineering*, 8(1), 56-68
- [2] Rosentrater, K. A., & Otieno, A. W. (2008). Determining machining parameters of corn byproduct filled plastics, *International Journal of Modern Engineering*, 9(1), 13-18
- [3] Zhang, J. Z., Rao, P. N., & Eckman, M. (2012). Experimental evaluation of a bio-based cutting fluid using multiple machining characteristics, *International Journal of Modern Engineering*, 12(2), 35-44
- [4] Lee, S. S. (2010). Tool condition monitoring System in turning operation utilizing wavelet signal processing and multi-learning ANNS algorithm methodology, *International Journal of Engineering Research & Innovation*, 2(1) 49-55
- [5] Cardoso, P., & Davim, J. P. (2011). A brief review on micromachining of materials. *Advanced Study Center*, Department of Mechanical Engineering, University of Aveiro, Campus Santiago, 30, 98-102
- [6] Cardoso, P., & Davim, J. P. (2012). Micro milling of metallic materials - A brief overview, *Transactions of FAMENA XXXVI-2* (2012), 79-85
- [7] Vogler, M. P., DeVor, R. E., & Kapoor, S. G. (2004). On the modelling and analysis of machining performance in micro-endmilling, Part I: Surface generation. *Journal of Manufacturing Science and Engineering*, 126(4), 685-694.
- [8] Filiz, S., Xie, L., Weiss, L., & Ozdoganlar, O. B. (2008). Micromilling of microbarbs for medical implants, *International Journal of Machine Tools and Manufacture*, 48, 459 - 472.
- [9] Iwata, K., Moriwaki, T., & Okuda, K., (1987). A Study of Cutting Temperature in Ultra-high Precision Diamond Cutting of Copper, *Transaction of the NAMRI/SME*, 15, 510-515.
- [10] Özel, T., Liu, X., & Dhanorker, A. (2007). Modeling and Simulation of Micromilling Process. CIRP 4th *International Conference and Exhibition on Design and Production of Machines and Dies/Molds*, Çeşme, Turkey, June 21-23.
- [11] Huo, D., & Cheng, K. (2009). Experimental investigation on micro-milling of oxygen-free, high-conductivity copper using tungsten carbide, chemistry vapour deposition, and single-crystal diamond micro tools, *Journal of Engineering Manufacture*, 224(B6), 995-1003.
- [12] Lee, K., Essel, I., & Dornfeld, D. (2001). Burr formation in micromilling, In *American Society for Precision Engineering Proceedings* (pp. 10-15).

-
- [13] Chu, C. H. (2000). *Integrated Edge Precision Machining*, Ph.D. dissertation, Department of Mechanical Engineering, University of California at Berkeley.
- [14] Mougou, A. L., Campos, F. D. O., & Araujo, A. C. M. D. (2013). A study of the influence of the width of cut on micro milling aluminum alloy, *Proceedings of 22nd International Congress of Mechanical Engineering (COBEM 2013)*, November 3-7, 2013, Ribeirão Preto, SP, Brazil (pp. 7840-7850)
- [15] Liu, Z., & Wang, X. (2009). Characteristic of surface profile and roughness in micro turn-milling of aluminum alloy 2A12, *Proceedings of International Technology and Innovation Conference 2009 (ITIC 2009)*, Xian, China (pp. 1-4)
- [16] Monroy-Vázquez, K. P., Attanasio, A., Ceretti, E., Siller, H. R., Hendrichs-Troeglen, N. J., & Giardini, C. (2013). Evaluation of Superficial and Dimensional Quality Features in Metallic Micro-Channels Manufactured by Micro-End-Milling, *Materials*, 6, 1434-1451
- [17] Filiz, S., Conley, C. M., Wasserman, M. B., & Ozdoganlar, O. B. (2007). An experimental investigation of micro-machinability of copper 101 using tungsten carbide micro end mills, *International Journal of Machine Tools and Manufacture*, 47(7), 1088-1100.
- [18] Prakash, J. R. S., Rahman, M., Senthil, K. A., & Lim, S. C. (2002). Model for predicting tool life in micro-milling of copper, *Chinese Journal of mechanical engineering*, 15, 115-120.
- [19] Mayor, J. R., & Sodemann, A. A. (2009). Investigation of the parameter space for enhanced tool life in high aspect-ratio full-slotting micromilling of copper. In *Proceedings of the 6th International Conference on Multi-Material Micro Manufacture*, 10.3850/4M2009RP001_9064
- [20] Fard, M. J. B., & Bordatchev, E. V. (2013). Experimental study of the effect of tool orientation in five-axis micro-milling of brass using ball-end mills, *The International Journal of Advanced Manufacturing Technology*, 67(5-8), 1079-1089.
- [21] Copper Development Association. (1992). *Cost-Effective Manufacturing machining brass, copper and its alloys*, retrieved from www.cda.org
- [22] Liu, X., DeVor, R. E., Kapoor, S. G., & Ehmann, K. F. (2004). The mechanics of machining at the micro-scale: assessment of the current state of the science, *Journal of Manufacturing Science and Engineering*, 126(4), 666-678.
- [23] Egashira, K., & Mizutani, K. (2010). Microdrilling and micromilling of brass using a 10 μm diameter tool, Retrieved from: http://www.cis.kit.ac.jp/~egashira/pdf/10um-diameter_tool.pdf (last accessed on March 10, 2015)

Biographies

MUHAMMAD P. JAHAN is an Assistant Professor in the Architectural and Manufacturing Sciences Department at Western Kentucky University. He earned his B.S. degree from Bangladesh University of Engineering & Technology (Mechanical Engineering, 2004), and Ph.D. (Mechanical Engineering, 2010) from the National University of Singapore. Dr. Jahan is currently teaching at Western Kentucky University. His interests are in advanced manufacturing, micro and nano manufacturing, lean manufacturing, and materials characterizations. Dr. Jahan may be reached at muhammad.jahan@wku.edu

GREGORY K. ARBUCKLE is an Associate Professor in the Architectural and Manufacturing Sciences Department at Western Kentucky University. He earned his B.S. degree (Mechanical Technology, 1996) from Indiana State University; M.S. (Industrial Technology, 1999) from Eastern Illinois University; and, Ph.D. (Technology Management, 2004) from Indiana State University. Dr. Arbuckle is currently teaching at Western Kentucky University. His interests are in quality assurance, robotics, automation, and 2+2 program development. Dr. Arbuckle may be reached at greg.arbuckle@wku.edu

ABDULHAMEED DAWOOD is a graduate student at Western Kentucky University, where he is earning a Master of Science Degree in Engineering Technology Management. He earned his B.S. degree (Optoelectronics Engineering, 2008) from the University of Technology, Baghdad, Iraq. His interests include sustainable machining and advanced manufacturing. Mr. Dawood may be reached at abdulhameed.dawood566@topper.wku.edu

RAMP RATE EFFECT ON MAXIMIZING PROFIT OF A MICROGRID USING A GRAVITATIONAL SEARCH ALGORITHM

F. Safdarian, Amirkabir University of Technology (Tehran Polytechnic); M.M. Ardehali, Amirkabir University of Technology (Tehran Polytechnic); G.B. Gharehpetian, Amirkabir University of Technology (Tehran Polytechnic)

Abstract

In this study, the short-term operation planning of a typical microgrid (MG) consisting of different units was optimized for achieving maximum profit, considering technical and economic constraints over a 24-hour period. Also investigated was the effect of ramp rate. The MG consisted of a diverse variety of power system components such as a wind turbine, microturbine, photovoltaic cell, fuel cell, electrolyzer, hydrogen storage tank, reformer, boiler, and electrical and thermal loads. Moreover, the MG was connected to an electrical grid for the exchange of power. The MG was managed and controlled through a central controller. The system costs included operation and maintenance costs, the cost of purchasing the natural gas for the required thermal energy, purchasing energy from the local grid, and the penalty costs in the curtailment strategy. The problem was a mixed-integer, nonlinear program that contained both real and binary parts. As such, metaheuristic methods were suitable and a gravitational search algorithm (GSA) was proposed.

The total profit obtained from the MG, based on the GSA but without considering ramp rate was \$2272.60; the total profit considering ramp rate was about \$2260.92. That is why the ramp rate constraint confined optimum performance of the binary section of the algorithms, which determined whether the units should be on or off and if that would cause a decrease in the final profit. Moreover, the results from the proposed algorithm were compared to a kind of improved genetic algorithm (GA) that is commonly used for these problems. Although the number of required iterations for the convergence of the problem using the GSA was lower, it took more computational time compared to the GA. Using the GA, the total profit not considering the ramp rate was \$2268.91, compared to \$2259.98 for the calculation taking into account the ramp rate limitations.

Introduction

In microgrids (MGs), energy management systems (EMSs) provide decision making for the generation of electric power and heat, storage systems, loading, and the

power exchanges with the local grid. MGs are low voltage distribution networks comprising electrical and thermal loads, energy storage systems (ESSs), and distributed generation sources (DGs), which are operated with a common controller. The main benefit of MGs is improving system reliability and demand supply. The significance of an MG is that the power generation is distributed so as to be closer to the end users. MGs can be either connected to the network or be operated independently in the island mode. When connected to the network, a MG may act either as a load or a small power source. MGs have many benefits that include: a) providing reliable, secure, efficient, and sustainable energy from renewable energy sources (RESs), while reducing transmission losses; and, b) reducing capital risk and supply growth in the demand based on a small investment. Moreover, low capital costs potentially enable low-cost entry into competitive markets [1-4].

Several studies have focused on optimizing the energy and operation management of MGs. Chen et al. [5] presented a smart energy management system in order to optimize the operation of a MG. They studied the characteristics of the photovoltaic (PV) output under different weather conditions and then presented a day-ahead power forecasting module. Zhang et al. [6] applied a performance metric to a MG's operation as stand-alone, grid-tied, and networked modes. Mohamed and Koivo [7] presented a general formulation to determine the optimal operating strategy and cost optimization scheme and to reduce the emissions from a MG. Mohamed and Mohammed [8] proposed an effective algorithm for optimizing the operation of the distribution system in a smart grid, from a cost and system stability point of view. They applied mathematical techniques to build accurate forecasting models for different sources and loads. Quashie and Joos [9] studied a general methodology for determining the optimal configuration of a MG and maximizing associated benefits. A hybrid smart-grid management system based on multiagents was examined by Ricalde et al. [10] in order to measure and control the loads inside a building, while power generation was forecasted using neural networks. Hatziargyriou et al. [11] described the main functions of the MG's central controller, required for optimization of the operation for the efficient participation in future real-time markets following different policies.

Khodaei and Shahidehpour [12] proposed a MG plan for the simultaneous optimization of the generation and transmission expansion in the power systems.

Shimoda et al. [13] showed a load forecast method and an optimized operation plan for DGs in a MG considering the heat sources, which run according to the thermal load prediction. The aim of Watanabe et al. [14] was to promote green energy usage, discuss concerns regarding energy supply during disasters, and improve the efficiency of the waste heat usage. Moreover, the optimal capacities of the solar cell, fuel cell (FC), electrolyzer (EL), and heat pumps were computed, while operating independently. Korpås and Holen [15] studied the operation of a hybrid plant consisting of wind turbines and hydrogen storage, while forecasts of the wind power were used for maximizing the expected profit from the power exchange in a day-ahead market; a penalty cost for un-provided hydrogen demand was also taken into account. Basu et al. [16] focused on how tracking electrical demand was economically shared between micro-turbines and diesel generators, on the basis of the multi-objective optimization of fuel costs and emissions. Niknama et al. [17] presented a new multi-objective, modified honey bee mating optimization algorithm for investigating the distribution feeder reconfiguration problem, assuming that RESs were connected to the distribution network.

Celli et al. [18] focused on the development of a novel EMS based on the application of neural networks. Mohanty et al. [19] developed an optimal design and plan for a MG containing different distributed-energy technology options such as PV, WT, a biomass gasified system, and diesel generator and battery storage for different applications and characteristics. In their study, the break-even distance for connecting the MG with the main grid was determined, as compared with the cost of the isolated MG. Bracco et al. [20] focused on the development of a mathematical model to optimally manage a smart, poly-generation MG, which contained combined heat and power (CHP) and considered thermal demand in order to minimize daily operational costs. Colas et al. [21] presented the aggregation and implementation of a determinist energy management method for business customers in a MG power system. Kanchev et al. [22] presented a MG energy management optimization method with the presence of PV-based active generators. To accommodate the high demand of renewable energy and the environmental policy, the planning and operation of micro-source generators was studied by Su et al. [23]. Alabedin et al. [24] studied the scheduling of power generation in a MG that had a group of dispatchable and non-dispatchable generators. Narayanaswamy et al. [25] evaluated hedging strategies for renewable resource integration and uncertainty management in the smart grid.

Carpinelli et al. [26] formulated an optimization model to solve the problem of the day-ahead optimal scheduling of a DC MG. Logenthiran and Srinivasan [27] studied a three-step method for the optimal generation scheduling of a MG in island-operation mode by solving the thermal unit commitment problem. Garcia and Bordons [28] addressed the short-term regulation service optimization linked to the long-term economical dispatch of a grid-connected MG. Logenthiran et al. [29] developed a distributed multi-agent system for the generation scheduling and monitoring of energy resources for optimized MG operation. Laera et al. [30] proposed a tool for the day-ahead operation plan of a grid-connected MG including distributed generators, electrical and thermal loads, and storage devices. The focus of the work by Chen et al. [31] was to perform an economic analysis, formulate an optimization model, and determine optimal operating strategies for smart MG systems. Mashhour and Tafreshi [32] developed a multi-period optimization model for an interconnected MG that participated in the wholesale energy market in order to maximize total profit.

In this current study, the authors investigated the short-term operation planning of a typical MG with diverse units and optimized it for achieving maximum profit, considering technical and economic constraints over a 24-hour period along with the effect of ramp rate.

System Description

The MG in this study was connected to the network for the exchange of power, where it was managed and controlled through a central controller. In this MG model, energy suppliers included: two DG units, which were managed or owned independently; DG units that were owned by the MG manager including WT, PV, three conventional microturbines (MTs), controllable loads, and thermal loads provided by a boiler that recovered heat from MTs and FC. The storage system included the EL, hydrogen storage tank, FC, and reformer. Furthermore, there were four types of loads: thermal, critical, controllable, and price-sensitive. The MG model is depicted in Figure 1. In this study, parameters such as price, capacity, and characteristics and demands of DGs were extracted from the work by Bagherian and Tafreshi [1].

Problem Formulation

The objective function for the operation of an EMS is to maximize the profit of a MG owner over the next 24-hour period, which is defined as income minus cost and is expressed by Equation (1). The total income of the MG includes the income from the sale of electrical energy to the local grid as well as consumers inside the MG control area

and the income from the sale of thermal energy. The operational costs consist of the cost of the purchased electrical energy from independent DG units, the cost of purchased energy from the local grid, the cost of purchased gas for thermal loads, while the production of thermal energy is not sufficient, and the cost of energy production through MG generation units such as MTs and FC. Moreover, a penalty is considered when load shedding is applied to controllable loads. The bids from independent DGs depend on many parameters such as startup, operation and maintenance costs of the units, consumer demand, energy price in the power market, and weather forecast data.

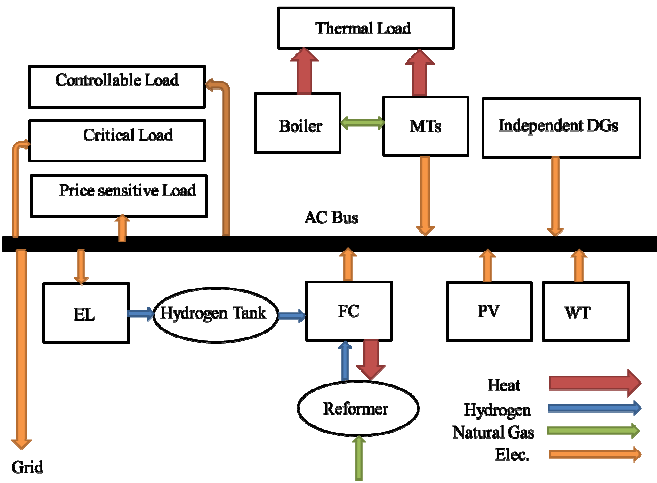


Figure 1. MG Schematic Diagram

$$\begin{aligned}
 OF = & \sum_{t=1}^{24} \{P_G(t) \times p_G(t) + P_d(t) \times p_d(t) + \\
 & P_{therm}(t) \times P_{therm}(t) - \sum_{j=1}^2 u_j(t) \times P_j(t) \times p_j(t) \\
 & - \sum_{k=1}^3 C_{mt-k}(P_{mt-k}(t)) - C_{fc}(t) - C_{el}(t) \\
 & - C_{therm}(P_{therm}(t)) - C_L(P_{sh}(t))\} \quad (1)
 \end{aligned}$$

Cost components are described by Equations (2)-(5). Equation (2) contains the operational and startup costs of MT units. The first term of Equation (3) is the cost of hydrogen production in the reformer unit that depends on the natural gas price, C_{NG} , and the natural gas consumption rate, G . The second term refers to the startup cost, while the third term indicates the operational costs of the FC. Hydrogen costs are not considered in Equation (3) because the FC consumes the hydrogen that is produced in the EL. Since operation and maintenance costs are assumed constant, they do not depend on the performance of the EL and the FC. Equation (4) contains the operational costs of the EL. It must be noted that C_{fc} and C_{el} do not depend on

the power because the useful life of EL and FC are considered as not dependent on the power. The penalty factor that is considered when a MG cannot supply the load demand and has to shed a P_{sh} amount of controllable loads, is modeled as a convex quadratic cost function, as given in Equation (5).

$$\begin{aligned}
 C_{mt-k} = & a_{mt-k} + \beta_{mt-k} P_{mt-k} + \gamma_{mt-k} P_{mt-k}^2 \\
 & \frac{t_{off}}{(a_{stmt-k} + \beta_{stmt-k}(1 - e^{-\tau}))} \\
 & \times u_{mt-k}(t)(u_{mt-k}(t) - u_{mt-k}(t-1)) \quad (2)
 \end{aligned}$$

$$\begin{aligned}
 C_{fc} = & C_{NG} \times G + (a_{fc} + \beta_{fc}(1 - e^{-\tau})) \\
 & \times u_{fc}(t)(u_{fc}(t) - u_{fc}(t-1)) + OM_{fc} \quad (3)
 \end{aligned}$$

$$\begin{aligned}
 C_{el} = & (a_{el} + \beta_{el}(1 - e^{-\tau})) \\
 & \times u_{el}(t)(u_{el}(t) - u_{el}(t-1)) + OM_{el} \quad (4)
 \end{aligned}$$

$$C_L = \beta_L P_{sh} + \gamma_L P_{sh}^2 \quad (5)$$

Case Studies

The active and thermal power balances require two equality constraints each hour; this is given by Equation (6):

$$\begin{aligned}
 P_d + P_{el} = & P_G + \sum_{j=1}^2 P_j + \sum_{k=1}^3 P_{mt-k} \\
 & + P_{wt} + P_{pv} + P_{fc} \quad (6)
 \end{aligned}$$

P_{therm} is supplied from the boiler (P_{boiler}) and the heat from the MT is given by Equation (7):

$$P_{boiler} + \sum_{k=1}^3 P_{mt-k} = P_{therm} \quad (7)$$

Power produced by the system is limited according to the particular capacity and demand of the system and is always more than a certain amount. There are also some limitations regarding the unit's minimum on and off times. The load shedding time should not exceed a certain period in the day. Ramp rate effect was investigated in this study and results with and without this limitation were compared. Unequal constraints are expressed by Equations (8)-(15).

$$P^{\min} \leq P_{mt-k} \leq P^{\max} \quad (8)$$

$$P^{\min} \leq P_{fc} \leq P^{\max} \quad (9)$$

$$P^{\min} \leq P_{el} \leq P^{\max} \quad (10)$$

$$(T_{i-1}^{on} - MUT)(u_{i-1} - u_i) \geq 0 \quad (11)$$

$$(T_{i-1}^{off} - MDT)(u_i - u_{i-1}) \geq 0 \quad (12)$$

$$P^{\min} \leq P_d \quad (13)$$

$$T_{shed} \leq T^{\max} \quad (14)$$

$$-DR \leq P(t) - P(t-1) \leq +UR \quad (15)$$

Since the WT and PV produce power from free inputs, it was assumed that the optimized production would yield the highest possible amount that is predicted. Hence, the power of these units was not considered in the optimization function. However, they were considered in the power balance equality constraint. The power that is generated by the WT was predicted, while considering the wind speed, the output power, PV output, and the temperature and solar radiation. The power predicted from the PV and WT is depicted in Figure 2 and the connected grid load in Figure 3 [1].

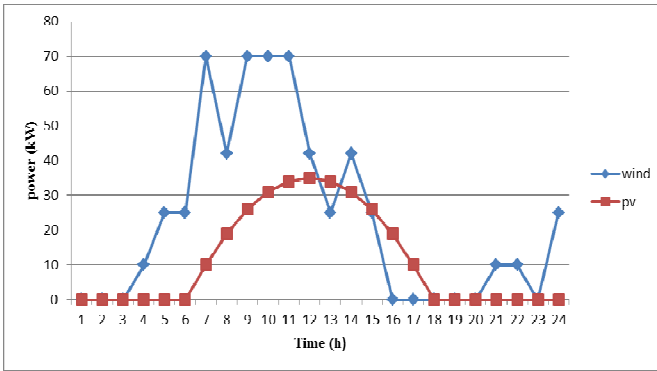


Figure 2. PV and WT Predicted Power (kW)

Solution Methodologies

The case studied was a Mixed-Integer Nonlinear Programming (MINLP) case that contained both real and

binary parts. There are few methods that can solve this kind of problem and classic methods usually have shortages. Exact optimization algorithms are not able to provide an appropriate solution for solving optimization problems with a high-dimensional search space. In these problems, the search space grows exponentially with the problem size; therefore, an exhaustive search was not practical. Also, classical approximate optimization methods make several assumptions to solve the problems. Sometimes, the validation of these assumptions is difficult in each problem. However, metaheuristic algorithms are robust and can adapt solutions with changing conditions and environments; they can be applied in solving complex multimodal problems and may incorporate mechanisms for avoiding getting trapped in local optima. Furthermore, these algorithms are able to find promising regions in a reasonable time, due to exploration and exploitation abilities. Hence, metaheuristic algorithms, which make few or no assumptions about a problem and can search very large spaces of candidate solutions, have been extensively developed to solve optimization problems. Among these algorithms, population-based metaheuristic algorithms are proper for global searches, due to global exploration and local exploitation abilities [33].

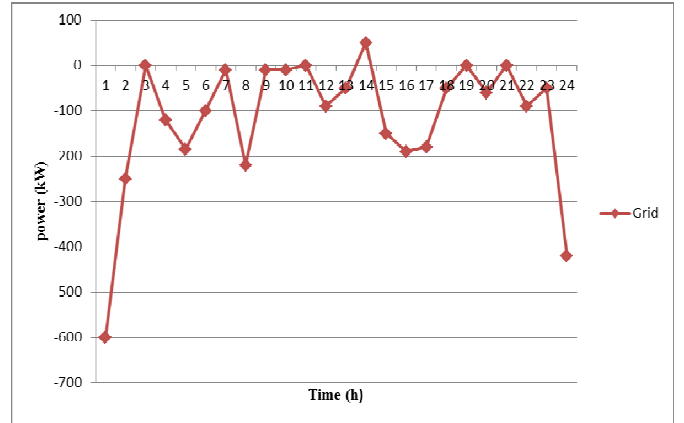


Figure 3. Predicted Grid Load (kW)

Scheduling problems represent a large class of combinatorial optimization problems. In most of these cases, finding the optimal solution is very difficult. In fact, with few exceptions, the only known method for solving the problem of optimality would be to enumerate an exponential number of possible solutions. Under these conditions, a metaheuristic method is necessary in order to find a good quality solution in a reasonable amount of time. [34] Thus, metaheuristic methods were proposed for this problem.

The Gravitational Search Algorithm (GSA) is a rather novel metaheuristic algorithm that has proved to have an appropriate performance in many optimization problems [35 -41] and the Genetic Algorithm (GA) is a commonly used

metaheuristic algorithm [2], [42-50]. Hence, the GSA was used to optimize MG planning for the next 24-hour period and the results were compared with the GA. The objective function contains both real and binary parameters; real parts determine the optimum power and binary parts decide whether the units should be on or off. Binary and real parts must be optimized simultaneously and hybrid algorithms are used for this problem.

Gravitational Search Algorithm

The GSA is based on the laws of gravity and mass interactions. Each mass (agent) has four specifications including: position, inertial mass, active gravitational mass, and passive gravitational mass. Every position of the mass corresponds to one solution of the problem, and gravitational and inertial masses are determined via a fitness function. In fact, the GSA is navigated by properly adjusting the masses. For this reason, the masses obey the Newtonian laws of gravitation and motion. According to the law of gravity, each mass attracts other masses. The gravitational force between two particles is directly proportional to the product of their masses and inversely proportional to the distance between them, R . Here R is used instead of R^2 because the experiment proves that R provides better results than R^2 . Masses must be attracted by the heaviest one, which presents an optimum solution in the search space.

Considering a system with N agents, the position of the i th agent is defined by Equation (16):

$$X_i = (X_i^1, \dots, X_i^d, \dots, X_i^n) \text{ for } i = 1, 2, \dots, N \quad (16)$$

The force acting on mass i from mass j is defined by Equation (17):

$$F_{ij}^d(t) = g(t) \frac{M_{pi} \times M_{aj}}{R_{ij}(t) + \varepsilon} (X_j^d(t) - X_i^d(t)) \quad (17)$$

$R_{ij}(t)$ is the Euclidian distance between agents i and j , as given by Equation (18):

$$R_{ij}(t) = \left\| X_i(t), X_j(t) \right\|_2 \quad (18)$$

To give a stochastic characteristic to the algorithm, the total force that acts on agent i , in dimension d , F_i^d , which is shown in Equation (19), is the randomly weighted sum of the d th components of the exerted forces from other agents. To improve the performance of the GSA by controlling exploration and exploitation, it was assumed that only the K best agents would attract the others. K best is a function of

time, with the initial value, $K0$, at the beginning and decreasing with time. At the beginning, all agents apply the force but, as time passes, K best is decreased linearly and, at the end, only 2% of the agents apply force to the others. Thus, K best is the set of first K agents with the best fitness value and the biggest mass, as shown in Equation (19):

$$F_i^d(t) = \sum_{j \in Kbest, j \neq i} rand_j F_{ij}^d(t) \quad (19)$$

where, $rand_j$ is a random number in the interval $[0,1]$. According to the law of motion, the acceleration of the agent i at time t , and in the d th direction (a_i^d), is calculated by Equation (20):

$$a_i^d(t) = \frac{F_i^d(t)}{M_{ii}(t)} \quad (20)$$

The next position and velocity can be calculated using Equations (21)-(22):

$$v_i^d(t+1) = rand_i \times v_i^d(t) + a_i^d(t) \quad (21)$$

$$x_i^d(t+1) = x_i^d(t) + v_i^d(t+1) \quad (22)$$

where, $rand_i$ is used to give a randomized characteristic to the search.

The gravitational factor, g , is initialized at the beginning and reduced with the time in order to control search accuracy. In other words, g is a function of the initial value and time, and is shown in Equation (23):

$$g(t) = g(g_0, t) \quad (23)$$

Gravitational and inertia masses are calculated by the fitness evaluation. A heavier mass is a more efficient agent. Assuming the equality of masses, they are calculated using the map of fitness. The gravitational and inertial masses are updated in each iteration by Equations (24)-(26):

$$M_{ai} = M_{pi} = M_{ii} = M_i, \quad i = 1, 2, \dots, N \quad (24)$$

$$m_i(t) = \frac{fit_i(t) - worst(t)}{best(t) - worst(t)} \quad (25)$$

$$M_i(t) = \frac{m_i(t)}{\sum_{j=1}^N m_j(t)} \quad (26)$$

For maximization problems, Equations (27)-(28) are used [51-52]:

$$best(t) = \max\{fit_j(t)\} \quad j \in \{1, \dots, N\} \quad (27)$$

$$worst(t) = \min\{fit_j(t)\} \quad j \in \{1, \dots, N\} \quad (28)$$

In this study, the GSA population and the number of GSA iterations were considered 500 and 200, respectively.

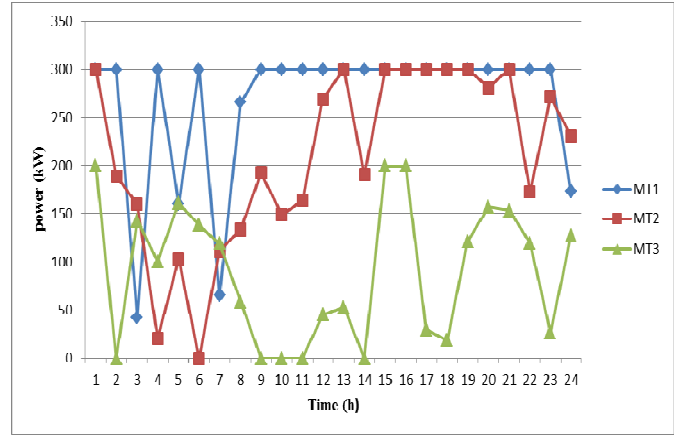
Genetic Algorithm

The GA is a conventional optimization method that is inspired from the evolution and heredity of living organisms. It has six steps including generating the initial population, ranking and probability calculations, selection, crossover, mutation, replacement, and checking the final conditions. There are different ways to choose each step, depending on the optimization problem. In this study, the exponential function was used for ranking. After calculating the probability of the intervention of each chromosome in developing the next generation, the Roulette Wheel method was used for the selection. In the crossover step, the Affin method, which is a combination of the arithmetic and linear crossover, was employed. Also, the dynamic mutation and generational replacement were utilized. In order to optimize the GA method, the most competent members were sorted and kept in any repetition, and which replaced the previous members. In this study, the probability of mutation was assumed to be 0.03; the probability of crossover to be 0.8; the GA population to be 500; and, the number of GA iterations to be 1000 [53].

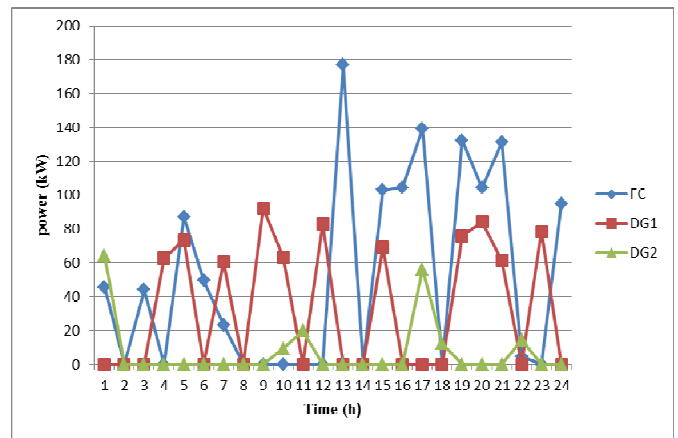
Results

The results from optimum MG planning for units without ramp rate were compared with the results of optimum planning of the units with ramp rate; the proposed plan is illustrated in Figures 4 and 5, respectively. The total obtained profit from the objective function of the given MG using the GSA was \$2272.60 without considering ramp rate, and estimated to be about \$2260.92 with considering ramp rate limitations in generation plants.

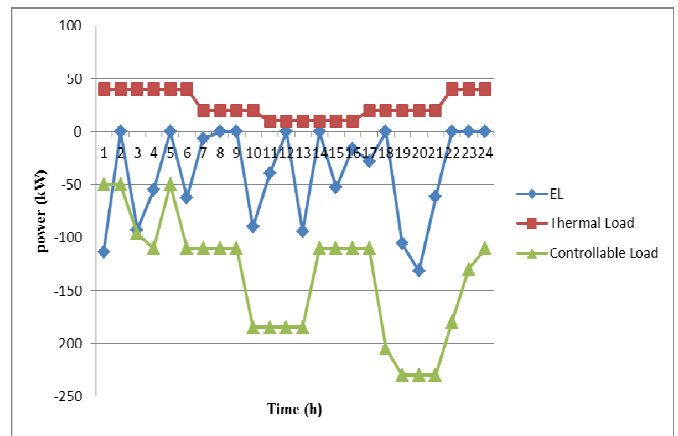
In order to compare the efficiency of the proposed algorithm with a commonly used method, the GA was applied to the problem. The results showed that, using the GA, the total gained profits from the objective function of the given MG was \$2268.91 disregarding ramp rate and \$2259.98 considering ramp rate limitations. The proposed plan is depicted in Figures 6-7.



(a) Microturbines

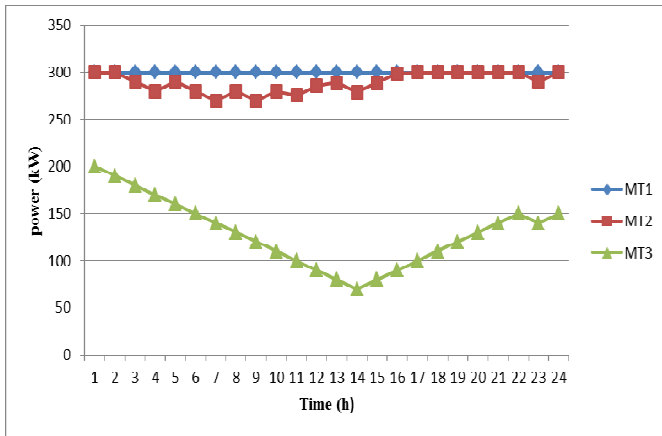


(b) Fuel Cell and Independent DGs

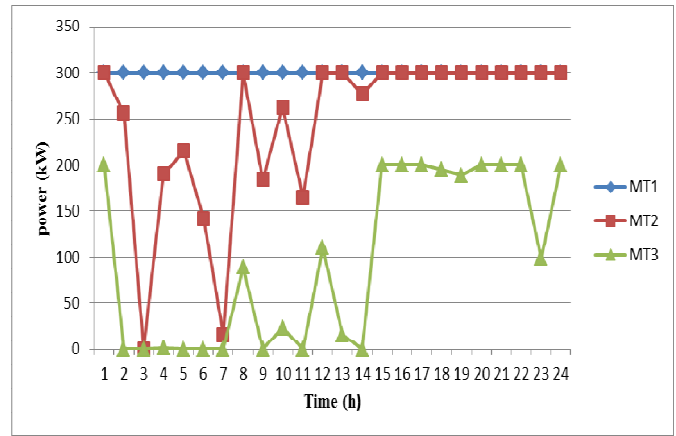


(c) Electrolyzer, Thermal Load, and Controllable Load

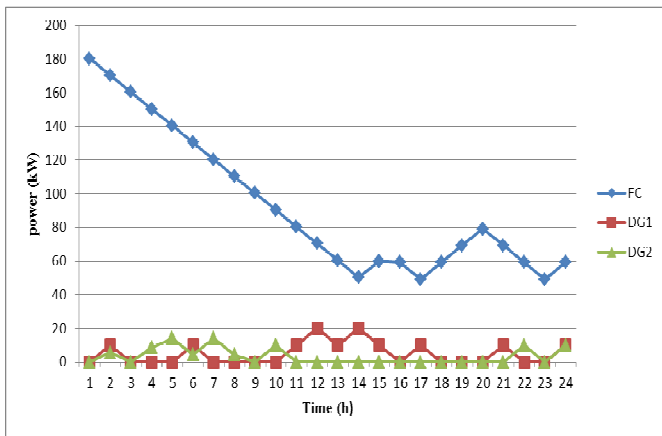
Figure 4. MG's Optimum Planning via the GSA for Units without Ramp Rate



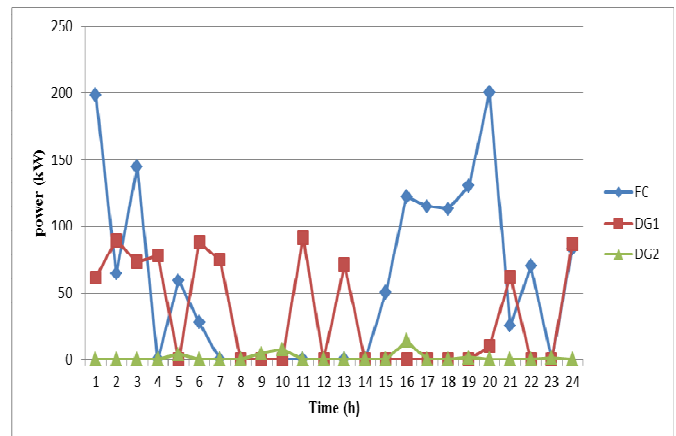
(a) Microturbines



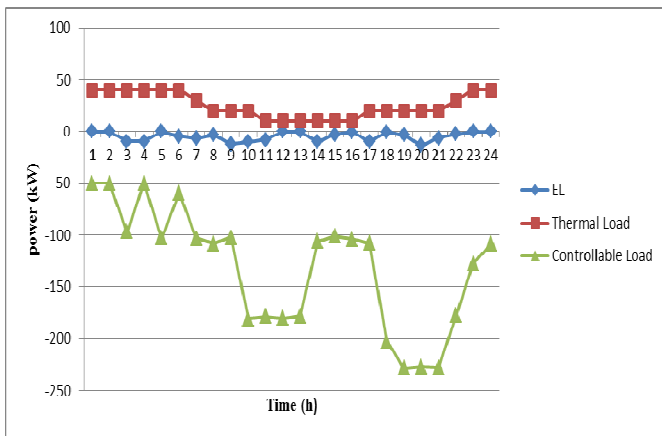
(a) Microturbines



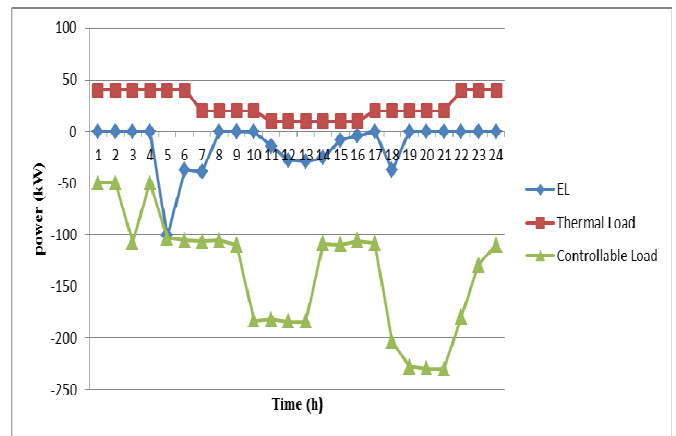
(b) Fuel Cell and independent DGs



(b) Fuel Cell and Independent DGs



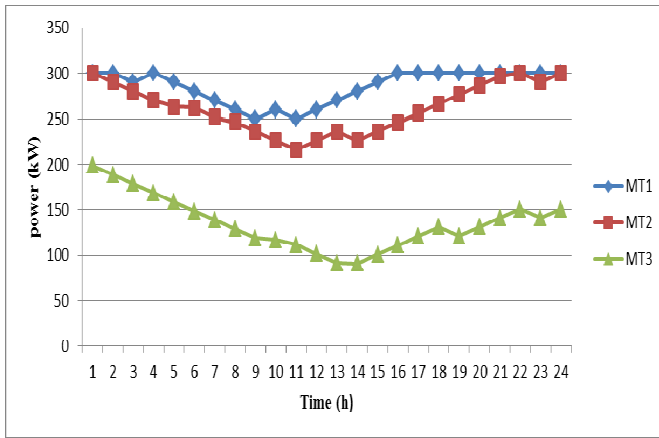
(c) Electrolyzer, Thermal Load and Controllable Load



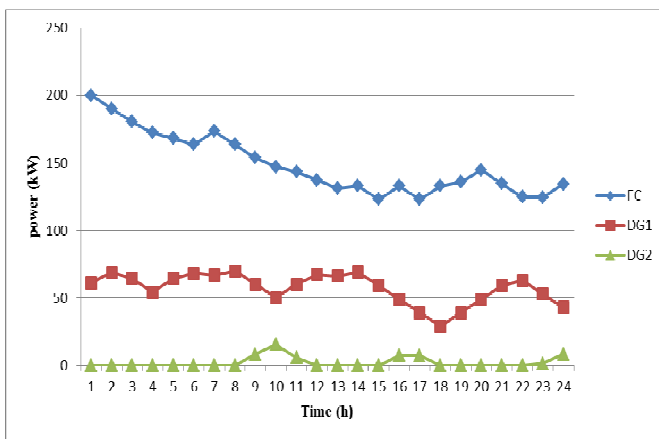
(c) Electrolyzer, Thermal Load, and Controllable Load

Figure 5. MG's Optimum Planning via GSA for Units with Ramp Rate

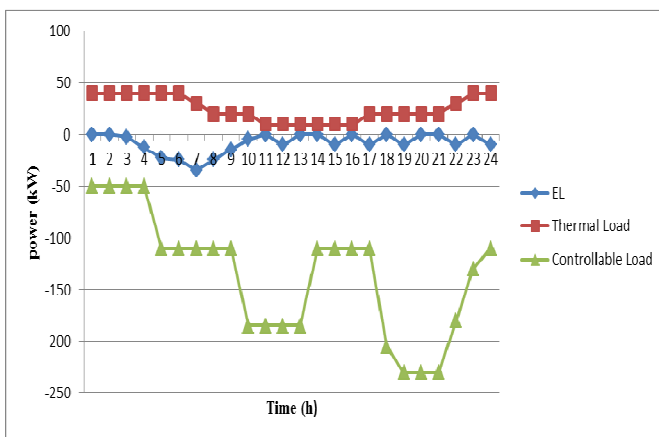
Figure 6. MG's Optimum Planning via the GA for Units without Ramp Rate



(a) Microturbines



(b) Fuel Cell and Independent DGs



(c) Electrolyzer, Thermal Load, and Controllable Load

Figure 7. MG's Optimum Planning via the GA for Units with Ramp Rate

The results showed that, despite the fact that the number of required iterations for convergence to the optimal solution via the GSA was less than the GA, it performed slower than the GA. Hence, the GSA is suggested for cases in which the accuracy is more important.

Conclusions

In this study, the optimum operation of a MG was presented over the next 24-hour period. The studied MG contained a diverse variety of possible MG components including: electrical and thermal loads, three MTs, FC, PV arrays, WT, EL, hydrogen storage tank, boiler, and reformer. Moreover, the MG was connected to the network that allowed the power exchange with the local grid. Some constraints were considered in the optimization problem in order to take into account the limitations that are usually found in the power generation of MGs. It was found that considering ramp rate caused an additional limitation, which hindered the optimal performance of the binary part to a certain extent and, thus, decreased the total profit. Furthermore, although the GSA performed slower than the GA in this problem and required more computational time, it gave a more optimized solution for maximizing the profit.

References

- [1] Bagherian, A., & Tafreshi, S. M. M. (2009). A Developed Energy Management System for a Microgrid in the Competitive Electricity Market. *IEEE Power Tech Conference*, (pp. 1-6). Bucharest.
- [2] Mohammadi, M., Hosseinian, S. H., & Gharehpetian, G. B. (2012). GA-based Optimal Sizing of Microgrid and DG Units under Pool and Hybrid Electricity Markets. *Electrical Power and Energy Systems*, 35 (1), 83-92.
- [3] Braun, M., & Strauss, P. (2008). A Review of Aggregation Approaches of Controllable Distributed Energy Units in Electrical Power Systems. *International Journal of Distributed Resources*, 4(4), 297-319.
- [4] Pilo, F., Pisano, G., & Soma, G. G. (2011). Optimal Coordination of Energy Resources with a Two Stage On-line Active Management. *IEEE Transactions on Industrial Electronics*, 58(10), 4526-4537.
- [5] Chen, C., Duan, S., Cai, T., & Liu, B. (2011). Smart Energy Management System for Optimal Microgrid Economic Operation. *Renewable Power Generation, IET*, 5(3), 258-267.
- [6] Zhang, L., Gari, N., & Hmurcik, L. V. (2014). Energy Management in a Microgrid with Distributed Energy Resources. *Energy Conversion and Management*, 78, 297-305.

- [7] Mohamed, F. A., & Koivo, H. N. (2007). System Modelling and Online Optimal Management of Micro Grid using Multiobjective Optimization. *International Conference on Clean Electrical Power*, (pp. 148-153). Capri.
- [8] Mohamed, A., & Mohammed, O. (2013). Real-time Energy Management Scheme for Hybrid Renewable Energy Systems in Smart Grid Applications. *Electric Power Systems Research*, 96, 133-143.
- [9] Quashie, M., & Joos, G. (2013). A Methodology to Optimize Benefits of Microgrids. *Power and Energy Society General Meeting (PES)*, (pp. 1-5). Vancouver, BC.
- [10] Ricalde, L. J., Ordonez, E., Gamez, M., & Sanchez, E. N. (2011). Design of a Smart Grid Management System with Renewable Energy Generation. *IEEE Symposium on Computational Intelligence Applications in Smart Grid (CIASG)*, (pp. 1-4). Paris, France.
- [11] Hatziaargyriou, N. D., Dimeas, A., Tsikalakis, A. G., Lopes, J. A. P., Karniotakis, G., & Oyarzabal, J. (2005). Management of Microgrids in Market Environment. *International Conference on Future Power Systems*, (pp. 1-7). Amsterdam.
- [12] Khodaei, A., & Shahidehpour, M. (2013). Microgrid-based Co-optimization of Generation and Transmission Planning in Power Systems. *IEEE Transactions on Power Systems*, 28(2), 1582-1590.
- [13] Shimoda, E., Numata, S., Baba, J., Nitta, T., & Masada, E. (2012). Operation Planning and Load Prediction for Microgrid using Thermal Demand Estimation. *IEEE Power and Energy Society General Meeting*, (pp. 1-7). San Diego, CA.
- [14] Watanabe, S., Obara, S., & Rengarajan, B. (2011). Operation Planning of an Independent Microgrid for Cold Regions by the Distribution of Fuel Cells and Water Electrolyze using a Genetic Algorithm. *International Journal of Hydrogen Energy*, 36(22), 14295-14308.
- [15] Korpås, M., & Holen, A. T. (2006). Operation Planning of Hydrogen Storage Connected to Wind Power Operating in a Power Market. *IEEE Transactions on Energy Conversion*, 21(3), 742-749.
- [16] Basu, A. K., Chowdhury, S., & Chowdhury, S. P. (2010). Operational Management of CHP-based Microgrid. *International Conference on Power System Technology*, (pp 1-5). Hangzhou.
- [17] Niknama, T., Kavousifarda, A., Tabatabaei, S., & Aghaei, J. (2011). Optimal Operation Management of Fuel Cell/Wind/Photovoltaic Power Sources Connected to Distribution Networks. *Journal of Power Sources*, 196(20), 8881-8896.
- [18] Celli, G., Pilo, F., Pisano, G., & Soma, G. G. (2005). Optimal Participation of a Microgrid to the Energy Market with an Intelligent EMS. *The 7th International Power Engineering Conference, IPEC*, (pp. 663-668). Singapore.
- [19] Mohanty, P., Bhuvanewari, G., & Balasubramanian, R. (2012). Optimal Planning and Design of Distributed Generation Based Micro Grids. *7th IEEE International Conference on Industrial and Information Systems (ICIIS)*, (pp 1-6). Chennai.
- [20] Bracco, S., Delfino, F., Pampararo, F., Robba, M., & Rossi, M. (2014). A Mathematical Model for the Optimal Operation of the University of Genoa Smart Polygeneration Microgrid: Evaluation of Technical, Economic and Environmental Performance Indicators. *Energy*, 61, 912-922.
- [21] Colas, F., Lu, D., Lazarov, V., Francois, B., & Kanchev, H. (2011). Energy Management and Power Planning of a Microgrid with a PV-based Active Generator for Smart Grid Applications. *IEEE Transactions on Industrial Electronics*, 58(10), 4583-4592.
- [22] Kanchev, H., Lazarov, V., & Francois, B. (2012). Environmental and Economical Optimization of Microgrid Long Term Operational Planning Including PV-based Active Generators. *15th International Power Electronics and Motion Control Conference (EPE/PEMC)*, (pp. 1-8). Novi Sad, Serbia.
- [23] Su, W., Yuan, Z., & Chow, M.-Y. (2010). Microgrid Planning and Operation: Solar Energy and Wind Energy. *IEEE Power and Energy Society General Meeting*, (pp. 1-7). Minneapolis, MN.
- [24] Zein Alabedin, A. M., El-Saadany, E. F., & Salama, M. M. A. (2012). Generation Scheduling in Microgrids under Uncertainties in Power Generation. *IEEE Electrical Power and Energy Conference (EPEC)*, (pp. 1-6). London, ON.
- [25] Narayanaswamy, B., Jayram, T. S., & Yoong, V. N. (2012). Hedging Strategies for Renewable Resource Integration and Uncertainty Management in the Smart Grid. *IEEE PES Innovative Smart Grid Technologies Europe (ISGT Europe)*, (pp. 1-8). Berlin, Germany.
- [26] Carpinelli, G., Bracale, A., & Caramia, P. (2013). The GREAT Project: Integer Linear Programming-based Day-ahead Optimal Scheduling of a DC Microgrid. *12th International Conference on Environment and Electrical Engineering (EEEIC)*, (pp. 1-6). Wroclaw.
- [27] Logenthiran, T., & Srinivasan, D. (2009). Short Term Generation Scheduling of a Microgrid. *TENCON 2009 - 2009 IEEE Region 10 Conference*, (pp 1-6). Singapore.
- [28] Garcia, F., & Bordons, C. (2013). Regulation Service for the Short-term Management of Renewable Energy Microgrids with Hybrid Storage using Model Predictive Control. *39th Annual Conference of the IEEE*

- Industrial Electronics Society*, (pp. 1-6). Vienna, Spain.
- [29] Logenthiran, T., Srinivasan, D., Khambadkone, A. M., & Aung, H. N. (2010). Multi-agent System (MAS) for Short-Term Generation Scheduling of a Microgrid. *IEEE International Conference on Sustainable Energy Technologies (ICSET)*, (pp. 1-6). Kandy, Sri Lanka.
- [30] Laera, M., Roggia, S., Dicorato, M., Forte, G., & Trovato, M. (2013). A Procedure for Day-ahead Optimal Operation Planning of a MicroGrid. *4th IEEE/PES Innovative Smart Grid Technologies Europe (ISGT Europe)*, (pp. 1-21). Lyngby, Copenhagen.
- [31] Yen-Haw Chen, Su-Ying Lu, Yung-Ruei Chang, Ta-Tung Lee, & Ming-Che Hu. (2013). Economic Analysis and Optimal Energy Management Models for Microgrid Systems: A Case Study in Taiwan. *Applied Energy*, 103, 145-154.
- [32] Mashhour, E., & Tafreshi, S. M. M. (2010). Integration of Distributed Energy Resources into Low Voltage Grid: A Market-based Multiperiod Optimization Model. *Electric Power Systems Research*, 80(4), 473-480.
- [33] Beheshti, Z., & Shamsuddin, S. M. H. (2013). A Review of Population-based Meta-Heuristic Algorithms. *ICSRs Publication*, 5(1), 1-35.
- [34] Lopez, P., & Roubella, F. (2010). Metaheuristics and Scheduling. In M. Widmer, A. Hertz, & D. Costa (Eds.), *Production Scheduling* (pp. 33-68). Hoboken, ISTE Ltd and John Wiley & Sons, Inc.
- [35] Mohamed Shuaib, Y., Surya Kalavathi, M., & Christopher Asir Rajan, C. (2015). Optimal Capacitor Placement in Radial Distribution System using Gravitational Search Algorithm. *Electrical Power and Energy Systems*, 64, 384-397.
- [36] Bhattacharyya, B., & Kumar, S. (2015). Reactive Power Planning with FACTS Devices using Gravitational Search Algorithm. *Ain Shams Engineering Journal*. doi:10.1016/j.asej.2015.02.002
- [37] Sarker, J., & Goswami, S. K. (2014). Solution of Multiple UPFC Placement Problems using Gravitational Search Algorithm. *Electrical Power and Energy Systems*, 55, 531-541.
- [38] Chatterjee, A., Roy, K., & Chatterjee, D. (2014). A Gravitational Search Algorithm (GSA) Based Photovoltaic (PV) Excitation Control Strategy for Single Phase Operation of Three Phase Wind-turbine Coupled Induction Generator. *Energy*, 74, 707-718.
- [39] Marzband, M., Ghadimi, M., Sumper, A., & Dominguez-Garcia, J. L. (2014). Experimental Validation of a Real-time Energy Management System using Multi-period Gravitational Search Algorithm for Microgrids in Islanded Mode. *Applied Energy*, 128, 164-174.
- [40] Niknam, T., Golestaneh, F., & Malekpour, A. (2012). Probabilistic Energy and Operation Management of a Microgrid Containing Wind/ Photovoltaic/Fuel Cell Generation and Energy Storage Devices Based on Point Estimate Method and Self-adaptive Gravitational Search Algorithm. *Energy*, 43, 427-437.
- [41] Kumar Rout, U., Kumar Sahu, R., & Panda, S. (2013). Gravitational Search Algorithm Based Automatic Generation Control for Interconnected Power System. *International Conference on Circuits, Power and Computing Technologies (ICCPCT-2013)*, (pp. 1-6). Nagercoil.
- [42] Obara, S. Y., & El-Sayed, A. G. (2009). Compound Microgrid Installation Operation Planning of a PEFC and Photovoltaics with Prediction of Electricity Production using GA and Numerical Weather Information. *International Journal of Hydrogen Energy*, 34, 8213-8222.
- [43] Obara, S. Y., Watanabe, S., & Rengarajan, B. (2011). Operation Planning of an Independent Microgrid for Cold Regions by the Distribution of Fuel Cells and Water Electrolyzers using a Genetic Algorithm. *International Journal of Hydrogen Energy*, 36, 14295-14308.
- [44] Alonso, M., Amaris, H., & Alvarez-Ortega, C. (2012). Integration of Renewable Energy Sources in Smart Grids by Means of Evolutionary Optimization Algorithms. *Expert Systems with Applications*, 39, 5513-5522.
- [45] Guo, L., Liua, W., Cai, J., Hong, B., & Wanga, C. (2013). A Two-stage Optimal Planning and Design Method for Combined Cooling, Heat and Power Microgrid system. *Energy Conversion and Management*, 74, 433-445.
- [46] Provata, E., Kolokotsa, D., Papantoniou, S., Pietrini, M., Giovannelli, A., & Romiti, G. (2015). Development of Optimization Algorithms for the Leaf Community Microgrid. *Renewable Energy*, 74, 782-795.
- [47] Kuznetsova, E., Li, W. F., Ruiz, C., & Zio, E. (2014). An Integrated Framework of Agent-based Modeling and Robust Optimization for Microgrid Energy Management. *Applied Energy*, 129, 70-88.
- [48] Obara, S. Y., & Watanabe, S. (2012). Optimization of Equipment Capacity and an Operational Method Based on Cost Analysis of a Fuel Cell Microgrid. *International Journal of Hydrogen Energy*, 37, 7814-7830.
- [49] Xu, Z., & Dong, Z. Y. (2004). Market-based Planning of Transmission Network using Genetic Algorithm. *8th International Conference on Probabilistic Methods Applied to Power Systems*, (pp. 1-6). Iowa State University, Ames, Iowa.
- [50] Safaei, N., Sadjadi, S. J., & Babakhani, M. (2006).

An Efficient Genetic Algorithm for Determining the Optimal Price Discrimination. *Applied Mathematics and Computation*, 181, 1693-1702.

- [51] Sarafrazi, S., Nezamabadi-pour, H., & Saryazdi, S. (2011). Disruption: A New Operator in Gravitational Search Algorithm. *Journal of Computer Science & Engineering and Electrical Engineering, Scientia Iranica, Sharif University of Technology*, 18(3), 539-548.
- [52] Shamsudin, H. C., Irawan, A., Ibrahim, Z., Abidin, A. F. Z., Wahyudi, S., Rahim, M. A. A., et al. (2012). A Fast Discrete Gravitational Search Algorithm. *4th International Conference on Computational Intelligence, Modelling and Simulation*, (pp. 1-5). Kuantan.
- [53] Nezamabadi-pour, H. (2010). *Genetic Algorithm*. Bahonar University of Kerman, Inc.

Biographies

F. SAFDARIAN is a graduate student in MSc and a member of the Energy Systems Laboratory in the Power and Energy Management Division of the Department of Electrical Engineering at Amirkabir University of Technology (Tehran Polytechnic), Iran. Her research interests include Power Management, Smart Grids, HVDC Systems, FACTS Devices, DGs, Renewable Energy, and Power Electronics. She may be reached at farnaz.safdarian@aut.ac.ir

M.M. ARDEHALI Ph.D., P.E., is an Associate Professor and the Director of the Energy Systems Laboratory in the Department of Electrical Engineering at Amirkabir University of Technology (Tehran Polytechnic), Iran. He received his Ph.D. in energy conversion from the University of Iowa in 1995 and completed postdoctoral studies at Iowa State University in 1997. With numerous publications and patents, Dr. Ardehali is a registered professional engineer in several states in the U.S. and specializes in control and applications of Artificial Intelligence for Energy Systems including power generation facilities.

G. B. GHAREHPETIAN was an Assistant Professor at Amirkabir University of Technology, Tehran, Iran, from 1997 to 2003; an Associate Professor from 2004 to 2007; and, Professor since 2007. He was selected by the ministry of higher education as the distinguished professor of Iran and by IAEEE as the distinguished researcher of Iran and was awarded the National Prize in 2008 and 2010. He is the author of more than 700 journal and conference papers. His teaching and research interests include Smart Grids, DGs, Monitoring of Power Transformers, FACTS Devices, HVDC Systems, and Power System Transients.

Appendix A

Nomenclature

t	time (hour)
j	the number of independent DG units
k	microturbine numbers
p	the related prices (ϵ)
u	the on/off state of each unit
OM	the operation and maintenance costs of each unit
P_G	the exchanged power with the local grid (kW)
P_d	the electrical load demand (kW)
P_{el}	the power produced from the electrolyzer (kW)
P_j	the power produced from independent DGs (kW)
P_{therm}	the thermal load demand (kW)
P_{boiler}	the power produced from the boiler (kW)
P_{mt-k}	the power produced from the k th microturbine (kW)
P_{wt}	the power produced from WT (kW)
P_{pv}	the power produced from PV (kW)
P_{fc}	the power produced from fuel cell (kW)
C_{therm}	the thermal load cost (ϵ)
C_{mt-k}	the costs of generation in the k th microturbine (ϵ)
α_{smt-k} and β_{smt-k}	the startup factors of the microturbine
t_{off}	the off-time
τ	time constant for the cooling
C_{fc}	generation costs of the fuel cell (ϵ)
C_{el}	generation costs of the electrolyzer (ϵ)
C_{NG}	the cost of purchasing the natural gas
C_L	costs of the curtailment strategy
β_L and γ_L	cost factors of the curtailment strategy
P_{sh}	the curtailed power at controllable load (kW)
T_{i-1}^{on}	on-time of the i th unit
T_{i-1}^{off}	off-time of the i th unit
MUT	the minimum up-time
MDT	the minimum down-time
T_{shed}	the maximum shedding duration
DR and UR	the minimum and maximum ramp rate
x_i^d	the position of the i th agent in the d th dimension
F_{ij}^d	the force acting on mass i from mass j in the d th direction
v_i^d	the velocity of the i th agent in the direction d th
a_j^d	acceleration of agent j in the direction d th
F_i^d	the total force that acts on agent i in dimension d
M_{aj}	active gravitational mass related to agent j
M_{pi}	the passive gravitational mass related to agent i
g	the gravitational constant
R_{ij}	the Euclidian distance between two agents i and j
M_{ii}	the inertial mass of the i th agent
fit_i	the fitness value of agent i
α_{fc} and β_{fc}	hot and cold startup factors of the fuel cell
α_{el} and β_{el}	hot and cold startup factors of the electrolyzer
G	natural gas consumption rate (m^3/h)

ANALYSIS OF WIND-POWER GENERATION WITH A WIND-GUIDE ATTACHMENT

Ulan Dakeev, University of Michigan–Flint; Connie Lam, University of Michigan–Flint; James Pung, University of Michigan–Flint

Abstract

In this study, the authors developed a new empirical method for a wind tunnel apparatus that can be used to improve the efficiency of power output by a small-scale wind turbine. A custom-designed wind tunnel attachment was constructed to record, analyze, and interpret both incoming and outgoing wind velocity readings. A number of case studies were performed in order to obtain power output versus wind velocity characteristics. The case studies included normal operation of the wind turbine at variable values of wind velocity with and without the proposed wind tunnel. The statistical t-Test and one-way ANOVA analyses resulted in a 60% increase in wind power output with the use of the custom design.

Introduction

The use of wind energy continues to grow significantly around the world. Along with solar, wind dominates the investment in new renewable capacity and is becoming the main form of renewable energy. For this reason, the development of wind turbines has been in great demand to enhance the usages and efficiencies. Unfortunately, wind turbines have limited features in low-level efficiencies [1]. Wind is the process whereby the movement of air flows from an area of high pressure to an area of low pressure [2]. This course of movement exists because the heat of the sun is unevenly distributed along the surface of the Earth. When hot air rises, the cooler air travels into the vacuum. As long as the sun continues to shine, the wind will continue to blow. With that, wind power is produced. A wind turbine will capture the energy of the movement of air and convert that to power. The blades of the wind turbine are aerodynamically designed to spin when wind is blowing.

A case study was carried out in Iran by Pourrajabian et al. [3], where they structured an experiment on the effects of air flow on the performance of an experimental wind turbine blade. That study aimed to improve the performance of the turbine at low wind speeds by considering factors such as density and altitudes, and then optimizing the structure of the blade. The wind turbine was tested in four different locations in Iran with altitudes up to 3000 m. The results showed that the blade, that was designed to be optimized for sea level, degrades for other locations and that degradation

was more significant for the initial performance than the power coefficient. The blade of the wind turbine was adjusted in two steps in order to develop optimization at varying altitudes. Adjustments to its geometry were made on the blade to optimize it for air density at elevations for power coefficient at the start of rotation. Another step was to optimize the tip speed ratio along with the blade. Optimizing the blade aimed to make the most of the output power.

Another study by Jureczko et al. [4] was an optimization of wind turbine blades. In their research, the authors determined the optimal shape of a blade and the optimal composite material. The goal was to advance a computer database package that would allow optimization of wind turbine blades. They considered the properties of the blade, aerodynamic loads, status of the load on the blade, and the selection of composite materials of the blade. Previous studies encouraged this current study to initialize the design of the wind tunnel attachment. The cone was designed and inserted to allow for a greater power output. The cone was shaped and constructed to allow the incoming air to flow from the wind turbine hub toward the tips of the wind turbine blades. In order to increase and maximize the low wind speeds going into the wind turbine, a custom-designed cone-shaped wind guide attachment was introduced.

In this customized design of a wind tunnel attachment, a wind guide apparatus, shown in Figure 1, was attached to the front of the small-scale wind turbine. It was fit in so that the enclosed space inside the wind tunnel would compose the wind when coming into the wind tunnel, allowing a higher wind output going out from it. Power produced by a wind turbine depends on the turbine and the parameters of the wind [5]. Several other factors needed to be accounted for in this experiment, but sometimes detailed data are not available, such as the streamline flow of the wind.

To avoid some limitations, the need to choose the appropriate location to test the wind tunnel was crucial [6]. A high, flat, and empty location was important because the properties and speeds of the wind must be exact in order to accurately measure the wind velocities entering and exiting the wind tunnel. In this case, turbulence, wind shear, and acceleration were considered. Being in a higher wind speed area would allow the best chances of receiving higher wind speeds because there would be no buildings causing turbulence and decreasing the output of wind power from the

wind turbine. Also, wind slows down when it is close to the ground [7]. The purpose of this current study was to experiment with a wind guide apparatus to the wind tunnel attachment in order to observe the differences in wind velocities going from the inlet to the outlet. This would help determine a way to develop increased power output from the wind turbine with lower wind speeds going into the turbine. The proposal, then, is a solution to wind turbines producing power at low-wind velocities.

Methodology

The current study consisted of a set of procedures that would test and analyze a wind turbine attachment to assess the performance of an experimental wind turbine at different wind velocities. A customized wind tunnel attachment was transported to a highly elevated field for the experiment. Construction was contracted to an outside vendor with the specification that the inlet section (larger diameter) be 1.45 times larger than the tube (smaller diameter). Additionally, the inlet section was constructed at a 30-degree angle from the horizontal surface of the tube. This angled section was not tested to compare how different angles would behave in terms of wind flow rate. Two anemometers were placed in order to measure the wind velocities at the inlet and outlet sections of the WTA (see Figure 2).



Figure 2. Wind Data Collection

The results of the 45 data points obtained were recorded into IBM's SPSS Statistics 20 package. A t-Test and analysis of variance were performed to observe the level of significance. The location that was chosen for the testing site was at the University of Michigan-Flint on the top level of the East parking garage. The average wind velocity at the test site was 10 mph, annually. The height of the testing point, approximately thirty feet above ground level, granted the team access to optimal wind conditions.



Figure 1. Wind Tunnel Attachment (WTA)

Experimental Analyses

The controllable variable during the field test was the wind guide apparatus mounted inside the wind tunnel attachment. A Pearson Correlation Coefficient (R) in Table 1 was calculated to be 0.963, where 1.0 is a perfect positive correlation. This showed a consistent wind velocity increase as wind exited the attachment [8]. In this case, the “Wind In” (x-axis) was compared to the “Wind Out” (y-axis) calculated with the number of sample data (n). Based on the results from the data collected, a strong correlation (0.963) existed between the velocity of the wind- in and the velocity of the wind out, when the wind guide apparatus was used. This reveals that the group was receiving consistent results from wind out data. R^2 is a statistical measure of how close the data are to the fitted regression line. Table 1 shows the model summary in which the standard deviation error of the estimate was 1.31598. The R^2 value is also known as the coefficient of determination; Figure 3 shows the R^2 value for the wind velocity. The adjusted R^2 value indicates the generalizability of variables in the regression equation [8].

Table 1. Model Summary

Model	R	R ²	Adjusted R ²	Std. Error of the Estimate
1	.963	.927	.926	1.31598

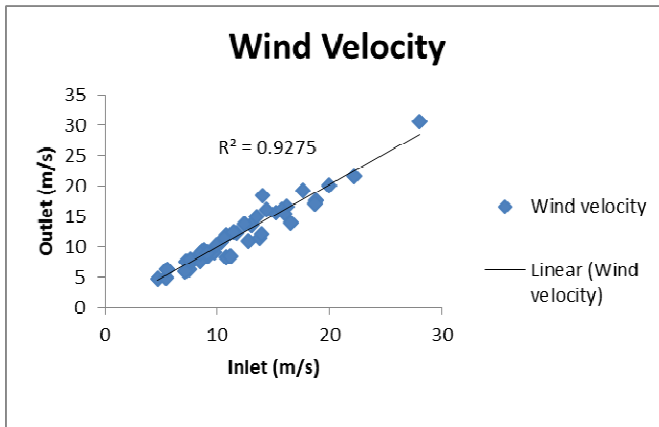


Figure 3. Wind Velocity

Table 2 shows the collection of wind data for all 45 points. It was sectioned in order to portray the mean, standard deviation, and standard error mean of the velocity for wind going in and wind going out. The test data points were used to perform an independent sample t-Test (see Table 3). The Levene’s Test showed a value of 0.034, less than $p=0.05$, to indicate the consideration of unequal variances. The calculated t-Test analysis for the difference of the wind velocity change in relation to incoming wind speed influ-

enced by the wind guide attachment to support the study objective is presented below. The categories wind in and wind out represent the incoming and outgoing wind, respectively [9].

Table 2. Group Statistics for Wind Data

Groups	N	Mean	Std. Deviation	Std. Error Mean
Wind In	45	7.8578	3.38791	0.50504
Wind Out	45	11.9622	4.82999	0.72001

Table 3. Levene’s Test for Equality of Variances

Levene’s Test for Equality of Variances	F	Sig.
Equal Variances Assumed	4.629	0.034
Equal Variances not assumed		0.034

The t-Test in Table 4 shows that the mean of the wind in was approximately Mean 1 = 7.85 mph, while the mean of wind out was approximately Mean 2 = 11.9 mph. Table 5 represents the chosen confidence interval of 95%. The p-value obtained from the analysis was $p = 0.034$, less than the alpha level of 0.05, which indicated that there was a significant difference between the average means of the wind velocities with the use of the custom WTA with the cone-shaped wind guide attachment and uncontrolled wind speed [10]. Figure 2 displays a better visual of individual wind velocities, taken at the time of data collection.

Table 4. t-Test for Equality of Means

t-Test for equality of means	t	df	Sig. (2-tailed)	Mean difference	Std. error
Equal variances assumed	-4.667	88	.000	-4.10444	.8794
Equal variances not assumed	-4.667	78.858	.000	-4.10444	.8794

Table 5. t-Test at 95% Confidence Interval of Difference

t-Test for equality of means	Lower	Upper
Equal variances assumed	-5.85222	-2.35667
Equal variances not assumed	-5.85505	-2.35384

A one-way analysis of variance was conducted in order to examine the effect of the WTA on differences in wind velocity changes for statistical significance. Table 6 shows the one way analysis of variance (ANOVA) test results for the wind velocity output to validate the t-Test analysis. The ANOVA table shows that there was still a significant difference between the incoming and outgoing wind velocity means. The F-statistic (F) of Table 6 is the ratio of the sum of squares between the samples divided by the degrees of freedom between all divided by the sum of squares within divided by the degrees of freedom of the sum of squares within. Since the numerator is much larger than the denominator, leaving us with a large F-statistic, one can conclude that the variation in the data is due mostly to the differences of the actual means and less to the actual variation within the means [11].

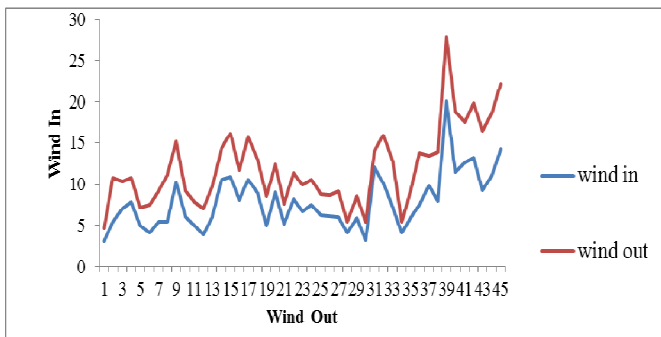


Figure 4. Comparison of Wind In and Wind Out

Table 6. One-way ANOVA

Wind Data	Sum of Squares	Df	Mean Square	F	Sig.
Between Groups	379.045	1	379.045	21.780	.000
Within Groups	1531.496	88	17.403		
Total	1910.541	89			

Conclusions

Based on the investigation that was conducted to evaluate the relationship between wind velocity outputs using a custom-designed wind tunnel apparatus (WTA) with wind guide attachment, a consistent increase in wind velocity was produced. According to the data accumulator run through Microsoft Excel, the mean wind velocity increase of approximately 60% was calculated based on the 45 wind data points collected at the University of Michigan-Flint on the

top level of the East parking garage. The calculated velocity increase confirms the hypothesis that containing wind particles and guiding them in a uniform direction will create a less turbulent wind flow, which will in turn enable a more uniform flow. This uniform flow will allow the wind particles to repel in the same direction inducing a greater wind velocity extracted from the WTA. This greater wind velocity generation will decrease the power generation starting point for a power-generating wind turbine.

Acknowledgements

This research was supported by the Undergraduate Research Opportunity Program at the University of Michigan-Flint.

References

- [1] Lucky, M., Ray, M., & Konald, M. (2013, July 30). Growth of Global Solar and Wind Energy Continues to Outpace Other Technologies. Retrieved March 8, 2014, from http://vitalsigns.worldwatch.org/sites/default/files/vital_signs_trend_growth_of_global_solar_and_wind_energy_continues_to_outpace_other_technologies_vital_signs_final_pdf.pdf
- [2] Wind 101: The basics of wind energy. (2013). Retrieved March 15, 2014, from <http://www.awea.org/Resources/Content.aspx?ItemNumber=900>
- [3] Pourrajabian, A., Mirzaei, M., Ebrahimi, R., & Wood, D. (2014). Effect of Air Density on the Performance of a Small Wind Turbine Blade: A Case Study in Iran. *Journal of Wind Engineering and Industrial Aerodynamics*, 126, 1-10. doi: 10.1016/j.jweia.2014.01.001
- [4] Jureczko, M., Pawlak, M., & Mężyk, A. (2005). Optimisation of Wind Turbine Blades. *Journal of Materials Processing Technology*, 167(2-3), 463-471. doi: 10.1016/j.jmatprotec.2005.06.055
- [5] Abed, K., & El-Mallah, A. (1997). Capacity Factor of Wind Turbines. *Energy*, 22(5), 487-491. doi: 10.1016/S0360-5442(96)00146-6
- [6] Beaucage, P., Brower, M. C., & Tensen, J. (2014). Evaluation of Four Numerical Wind Flow Models for Wind Resource Mapping. *Wind Energy*, 17(2), 197-208. doi: 10.1002/we.1568
- [7] Buckney, N., Pirrera, A., Green, S. D., & Weaver, P. M. (2013). Structural Efficiency of a Wind Turbine Blade. *Thin-Walled Structures*, 67, 144-154. doi: 10.1016/j.tws.2013.02.010
- [8] Illustration of regression analysis. (n.d.). Retrieved March 17, 2014, from <http://www.utexas.edu/>

courses/schwab/sw388r7/Tutorials/
IllustrationofRegressionAnalysis_doc_html/061_
Interpreting_Adjusted_R_Square.html

- [9] Residual Sum of Squares - RSS. (n.d.). Retrieved March 17, 2014, from <http://www.investopedia.com/terms/r/residual-sum-of-squares.asp>
- [10] Lane, D. M., Scott, D., Hebl, M., Osherson, D., & Ziemer, H. (n.d.). *Introduction to Statistics*. Retrieved March 17, 2014, from http://onlinestatbook.com/Online_Statistics_Education.pdf
- [11] ANOVA 3: Hypothesis test with F-statistic. (n.d.). Retrieved March 17, 2014, from <https://www.khanacademy.org/math/probability/statistics-inferential/anova/v/anova-3--hypothesis-test-with-f-statistic>

Biographies

ULAN DAKEEV received his Bachelors in Industrial Engineering in Georgia, Masters in Industrial Management in Iowa, and Doctorate in Technology in Iowa. He worked as a continuous improvement design engineer for John Deere Waterloo Works for 3.5 years. He is currently a faculty member in the Engineering Department at the University of Michigan-Flint. Dr. Dakeev may be reached at dakeev@umflint.edu

CONNIE LAM is a senior at the University of Michigan–Flint receiving a dual degree in Mechanical Engineering and Managerial Engineering with a minor in General Business. Connie has participated and presented posters for ASEE and other conferences in the U.S. and Canada. She is currently the President of University of Michigan–Flint’s Chapter for American Society of Mechanical Engineers and the Vice–President for the Society of Automotive Engineers. Ms. Lam may be reached at colam@umflint.edu

JAMES TRISTEN PUNG is a senior Mechanical Engineering student. James has been actively involved in proposal development for project funding. Some of his funded projects include support of local K-12 gyms. Mr. Pung may be reached at jpung@umflint.edu

VERTICAL AXIS WIND TURBINE PERFORMANCE PREDICTION MODELS USING HIGH AND LOW FIDELITY ANALYSES

Franklyn Kanyako, Masdar Institute of Science and Technology, UAE; Isam Janajreh, Masdar Institute of Science and Technology, UAE

Abstract

Vertical axis wind turbines have potential advantages for small domestic applications, as they can be effectively used in urban areas, where wind is intermittently unsteady and turbulent. In this paper, the authors highlight the progress made in the development of aerodynamic models for predicting the performance of straight-bladed, fixed-pitch vertical axis wind turbine blade profiles. An improved low-fidelity blade element momentum algorithm using a hybrid database was built to investigate the solidity of the turbine by analyzing the effect of blade chord, radius, and number of blades at different tip speed ratios. This was followed by a 2D numerical investigation to compare the performance prediction capability of computational fluid dynamics (CFD) and mathematical models. Both high- and low-fidelity analyses showed minimum/negative performance at low tip speed ratios, indicating the general inability of the fixed-pitch vertical axis turbine to self-start. The CFD analysis, though computationally intensive, showed better performance than the analytical solution and also captured important flow features such as vortex shedding, among other detailed flow field features.

Introduction

The development of wind turbine technologies has allowed wind energy to perform a relevant step forward in local production of clean electric power inside the built environment. The present technical design relies exclusively on horizontal axis turbines and is not yet adequate to develop reliable wind energy converters, particularly for conditions corresponding to low wind speeds and/or urban areas. This has renewed interest in Vertical Axis Wind Turbines (VAWT) like the Darrieus turbine, which appear to be particularly promising for such conditions. These VAWTs turbines can be used to power remote or off-grid applications such as homes, farms, refuges, or beacons. Intermediate-sized wind power systems (100 kW to 250 kW) can power a village or a cluster of small enterprises and can be grid-connected or off-grid. They can also be coupled with diesel generators, batteries, and other distributed energy sources for remote use, where there is no access to the grid design. However, the disadvantages of VAWTs stem from the fact

that there is cyclical variation in the angle of attack on the aerofoils as the rotor rotates. As a result, optimal loading cannot be sustained for all azimuthal angles, leading to inherently low aerodynamic efficiency compared to horizontal axis wind turbines (HAWT) [1]. The rotation of the turbine in 3D environments leads to several flow phenomena—such as dynamic stall, flow separation, and flow wake deformation—making the aerodynamic analysis and performance prediction of the Darrieus wind turbine very difficult. Currently, there are various computational models present, which have their own strengths and weaknesses, with the goal to accurately predict the performance of a wind turbine. Predicting wind turbine performance numerically offers a possibility to reduce the expensive and exhaustive wind tunnel and field experimental tests, the major benefit of which being that computational studies are more economical, versatile, and afford higher resolution than costly experiments.

Computational Models for VAWT

Despite the complexity of the aerodynamic behavior of the Darrieus VAWT, several mathematical models have been proposed for the performance prediction and design of the Darrieus VAWT. Based on a survey of aerodynamic models used for prediction of VAWT performance [1], [2], these models can be broadly classified into three categories, according to their increasing complexities: 1) momentum models, 2) vortex model, and 3) computational fluid dynamics (CFD).

The momentum model combines momentum theory with blade element theory [3]. It studies the behavior of the air flow on the blades and its forces. They can be further divided into single-stream tube, multiple-stream tube, and double-multiple stream tube models. In the single-stream tube model, first developed by Templin [4] for VAWTs, the turbine is placed inside a single-stream tube and its blades revolution is translated in an actuator disk. The effects of the stream tube outside are assumed negligible and the wind speed in the upstream and downstream sides of the turbine are assumed to be constant. This model suffers from performance accuracy prediction, due to the many assumptions and usually gives higher prediction values.

The multiple-stream tube model, developed by Strickland [5], is a variation of the single-stream tube model, where the single-stream tube is divided into several parallel adjacent stream tubes that are independent of each other and have their own undisturbed, wake and induced velocities. Several modifications/corrections have been incorporated into this model, where the drag forces, aerofoil geometry, curvature flow, etc., were added, while it provides relatively better accuracy than the single stream as it still lacks experimental validation. The double-multiple stream tube (DMS) model is a variation of the multiple-stream tube model, where the actuator disc is divided into two half cycles in tandem, representing the upstream and downstream sides of the rotor. This model was presented by Paraschivoiu [6].

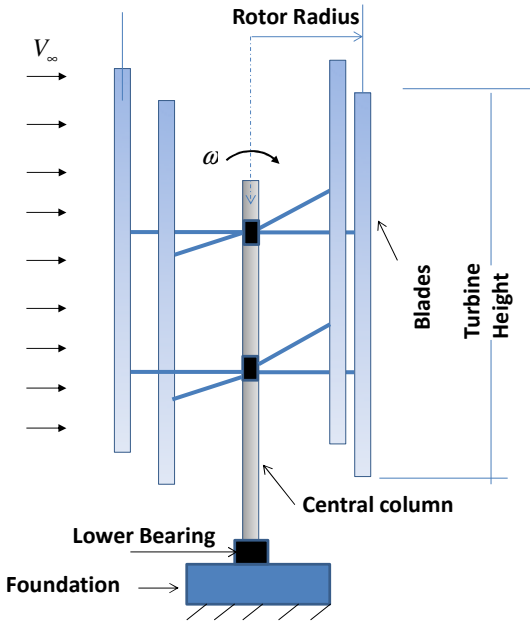
The vortex models are basically potential flow models based on the calculation of the velocity field about the turbine through the influence of vorticity in the wake of the blades. The turbine blades are represented by bound or lifting-line vortices whose strengths are determined using airfoil coefficient datasets and calculated relative flow velocity and angle of attack. Larsen [7] first introduced the idea of a vortex model for a single-blade element of a VAWT. He used the vortex model for the performance prediction of a cyclogiro windmill. The model is a two-dimensional one but, if the vortex trailing from the rotor blade tips is considered, it may be said that it is not strictly two-dimensional. However, in his model, angle of attack is assumed to be small; as a result, the stall effect is neglected. Strickland et al. [8] presented an extension of the vortex model, which is a three-dimensional one in which the aerodynamic stall is incorporated into the model. They presented the experimental results for a series of two-dimensional rotor configurations. Their calculated values showed good correlation with the experimental results for the instantaneous blade forces and the near wake flow behind the rotor. Strickland et al. also made improvements on the prior vortex model. The latest model is termed as the dynamic vortex model since, in this model, the dynamic effects are included. The improvements over the prior model are that it includes the dynamic stall effect, pitching circulation, and added mass effect. The main disadvantage of the vortex model is that it takes too much computation time. Furthermore, this model still relies on significant simplifications (e.g., potential flow is assumed in the wake and the effect of viscosity in the blade aerodynamics is included through empirical force coefficients) [9].

Computational fluid dynamics (CFD) is widely employed for VAWT performance analysis. It solves the Reynolds Averaged Navier-Stokes equation or the more advanced and costly Direct Numerical Simulation (DNS), Large Eddy Simulation (LES), and Detached Eddy Simulation (DES).

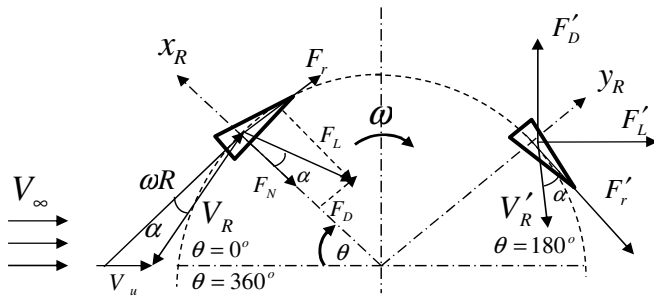
Dobrev and Massouh [10] conducted high-fidelity simulations to explore the possibility of using 3D Navier-Stokes solver Detached Eddy Simulation solver (DES)/ k - ω model and Particle Image Velocimetry (PIV) for experimental validation. The comparison of wake and shedding vorticity with experiments shows that the 3D/ k - ω modeling gives results quite similar to phase-averaged velocity. The power coefficient measured was very close to the experimental results, confirming the capability of the DES model to accurately capture the turbulent detached flow. Mohamed [11] carried out an aerodynamic investigation for 20 different airfoils using a 2D, unsteady Reynolds averaged Navier Stokes (RANS) simulation. He found the S-1046 profile for the H-Darrieus rotor very promising for wind energy generation, in particular in urban areas compared to symmetric airfoils. Many other studies have been done using RANS [12-14]; however, CFD is computationally intensive, as the aerodynamic performance of the turbine is a function of their instantaneous forces and moment coefficient. The objective of this current study was to investigate some of the most significant parameters that affect turbine performance such as turbine solidity, number of blades, airfoil selection, and turbine aspect ratio (H/D). In this paper, the authors focused on understanding the importance of these factors, specifically the first three to find the best configuration for the H-Darrieus turbines. This investigation was carried out by using a double-multiple stream model with a hybrid database of lift and drag coefficient prediction methodology from -180 °C to 180 °C, developed by Castelli et al. [15]. The result was compared with numerical simulations using the unsteady Reynolds averaged Navier stokes solver.

Aerodynamics Analysis of H-Darrieus VAWT

DMST Model: For the low-fidelity analysis, the DMST developed by Paraschivoiu [6] was adapted to a H-Darrieus based on the following assumptions: a) Unlike for the Troposkien/egg-shaped Darrieus turbine used by Paraschivoiu, it was assumed that no vertical variation of the induced velocity as straight vertical blade is subjected to the same flow velocity along its length—therefore, the angle δ that lies between the normal element to the blade element and horizontal XY plane is equated to zero ($\delta = 0$); b) It was assumed to be a fixed-pitch VAWT—therefore, using a symmetric airfoil section, the chord line is tangent to the circle of rotation (or blade flight path) and $a_0 = 0$. Illustration of the straight 4-bladed Darrieus type VAWT is shown in Figure 1(a) and the aerodynamic characteristics are depicted in Figure 1(b). The relative velocity component, V_R , can be obtained from the cordial velocity and normal velocity components, as given by Equation (1):



(a) Schematic of the Straight 4-bladed Darrieus Turbine



(b) Flow Within the Straight-bladed Darrieus Rotor

Figure 1. Illustration of the Flow Velocities of the Straight-bladed Darrieus Rotor

$$V_R = \sqrt{V_u^2 [(x - \sin \theta)^2 + \cos^2 \theta]} \quad (1)$$

where, V_u is the induced velocity, defined as the axial flow velocity through the rotor; θ is the azimuth angle; and, x is the local tip speed ratio (TSR), which is defined according to Equation (2):

$$x = \frac{\omega R}{V_u} \quad (2)$$

where, ω is the turbine's angular speed and R is the rotor radius. The fraction of the frontal swept area of the wind turbine covered by the blades represents the solidity, defined in Equation (3):

$$\sigma = \frac{NC}{R} \quad (3)$$

where, N is the number of blades; c is the chord length of the blades; and, R is the radius of the rotor. From the geometry in Figure 1, the expression for the local angle of attack may be derived by Equation (4):

$$\alpha = \sin^{-1} \left[\frac{\cos \theta}{\sqrt{(x - \sin \theta)^2 + \cos^2 \theta}} \right] \quad (4)$$

The normal and tangential force coefficients are expressed by Equations (5) and (6):

$$C_n = C_L \cos \alpha + C_D \sin \alpha \quad (5)$$

$$C_t = C_L \sin \alpha + C_D \cos \alpha \quad (6)$$

where, C_L is the lift coefficient and C_D is the drag coefficient for angle of attack α . Then the normal and tangential forces for a single blade at a single azimuthal location can be written according to Equations (7) and (8):

$$F_N = \frac{1}{2} \rho V_R^2 (h_c) C_n \quad (7)$$

$$F_T = \frac{1}{2} \rho V_R^2 (h_c) C_t \quad (8)$$

where, h is the blade height and c is the blade chord length. Referring to Figure 1, the force of the wind on the turbine, which is experienced by one blade element in the direction of the air flow, is denoted as the instantaneous thrust force, according to Equation (9):

$$T_i = \frac{1}{2} \rho V_R^2 (h_c) (C_n \sin \theta - C_t \cos \theta) \quad (9)$$

This is because the tangential force component creates the rotation of the wind turbine and generates the torque necessary to produce electricity. The instantaneous torque or the torque by a single blade at a single azimuthal location is described by Equation (10):

$$Q_i = F_T R \quad (10)$$

Substituting Equation (8) into Equation (10) yields Equation (11):

$$Q_i = \frac{1}{2} \rho V_R^2 (h_c) C_t R \quad (11)$$

Figure 2 shows a diagram of the DMS model [16]. The actuator disc is divided into two with each having its own induced velocity. The induced velocity decreases along the axial stream tube direction, so the induced velocity in the upstream, V_{aui} , is less than the undisturbed wind speed, V_{oi} , which arrives to the stream tube. Between the upstream and the downstream there is an equilibrium induced velocity, V_{ei} , that is less than the V_{aui} .

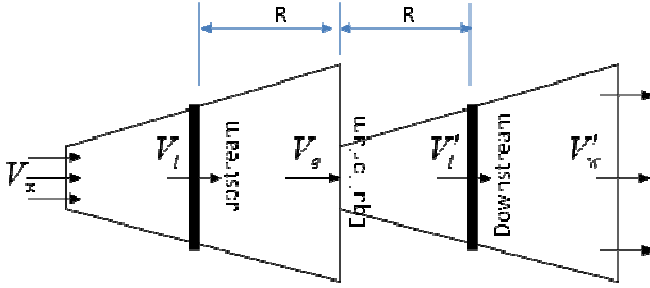


Figure 2. 2D Schematic of the DMST Model

The induced velocity in the downstream, V_{ad} , is less than V_{ei} . So Equation (12) yields the induced velocity in the upstream, V_{au} :

$$V_{au} = V_{\infty i} K_{us} \quad (12)$$

where, K_{us} is the interference factor for the upstream, which is less than one and is given by Equation (13):

$$K_{us} = \frac{V_{au}}{V_{\infty i}} \quad (13)$$

The induced velocity in the midstream, V_e , is influenced by the wake velocity of the upstream, which is given by Equation (14):

$$V_e = V_{\infty i} \left(2 \frac{V_{au}}{V_{\infty i}} - 1 \right) = V_{\infty i} (2K_{us} - 1) \quad (14)$$

The induced velocity in the downstream, V_{ad} , is given by Equation (15):

$$V_{ad} = K_{ds} V_e = K_{ds} (2K_{us} - 1) V_{\infty i} \quad (15)$$

where, K_{ds} is the interference factor for the downstream and is given by Equation (16):

$$K_{ds} = \frac{V_{ad}}{V_e} \quad (16)$$

As can be seen, the aerodynamic behavior of the blades on the upstream side of the wind turbine will influence the induced velocity on the blades in the mid- and downstream regions. The undisrupted wind velocity, $V_{\infty i}$, is defined by the wind velocity profile and typically increases along the wind turbine height, according to a given local atmospheric boundary layer velocity profile. By applying the DMS model with the VAWT performance equations presented previously, it is possible to predict the turbine performance. The torque and power coefficients are found by integrating the aerodynamic behaviors of the various stream tubes. These iterative procedures, which are used in the DMST analysis, are illustrated in Figure 3. For the entire process, 36 stream

tubes were used; and, evaluating the wind conditions at blade positions at five-degree increments, no significant difference was observed with an increase in the number of stream tubes. The induction factors a_u and a_d were calculated for the upstream and mid- and downstream tubes of the turbine, respectively.

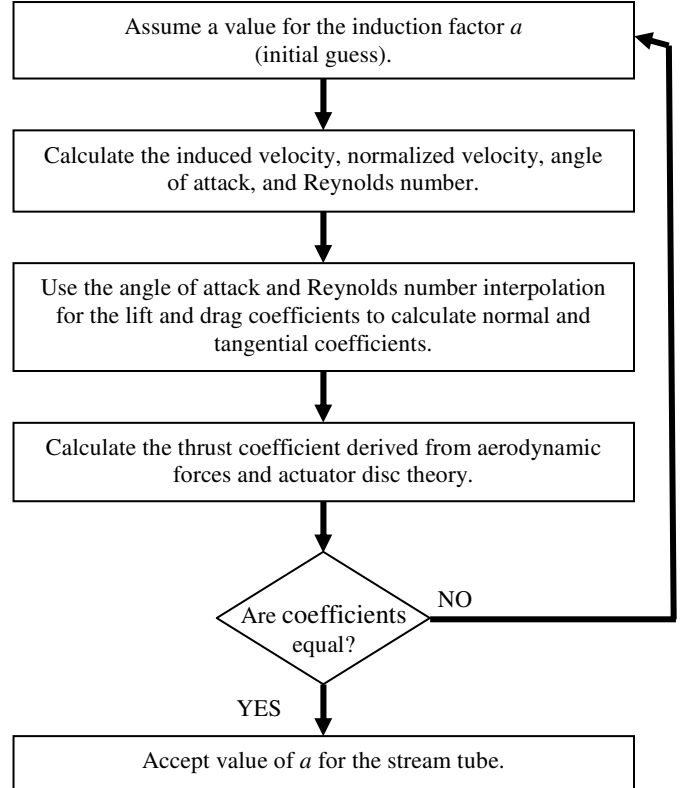
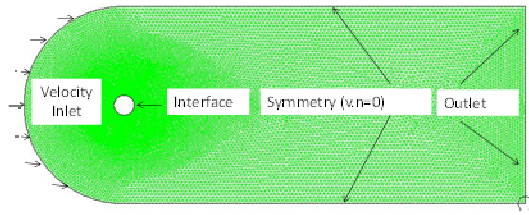


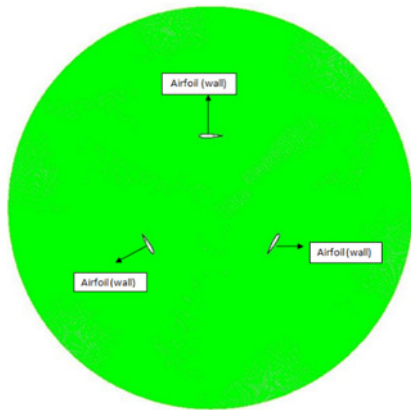
Figure 3. Iterative Procedure for Calculating the Flow Velocity in the DMST Model

CFD Model: The 2D wind turbine model was created using Gambit meshing software. The mesh and boundary conditions are shown in Figure 4, where the interior domain containing the wind turbine blades was considered as the moving mesh, while the outer domain was stationary. An unstructured grid was chosen for the moving and structured grid for the stationary domain. An interface was set between the interior sliding and outer stationary domain. The mesh on both sides of the interface had approximately the same characteristic cell size rendering the simulation more accurate and having faster convergence. The interior sliding domain rotated with a prescribed rotational velocity, ω . The inlet boundary was placed 5D upstream and the outlet placed at 20D downstream. The domain around the airfoil had to be wide enough to allow the vorticity and dynamic stall to fully develop. For both static and sliding models, the inlet boundary condition was velocity inlet. The upper and lower boundaries were assumed to be symmetrical, meaning

a zero normal gradient of pressure and velocity. The exit boundary was set as the pressure outlet in which the gauge pressure was set to zero gauge or atmospheric.



(a) The Fixed Domain of the Turbine



(b) The Rotating Domain of the Turbine Hub

Figure 4. Domain and Boundary Conditions for the 3-bladed VAWT

The boundary layer was placed on the blade profile, as shown in Figure 5, in order to capture the steep flow gradient at the airfoil surface and accurately determine lift, drag, and the separation of the flow from the blade surface. The average y^+ , which is the height of the first wall-adjacent cells inside the viscous sub-layer of the boundary layer, was set to $2E-5C$, which corresponded to $y^+ \leq 1$.

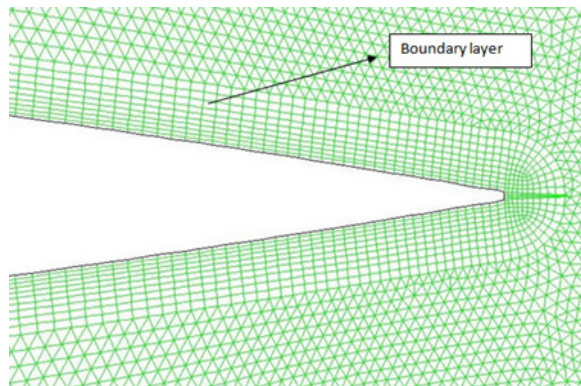


Figure 5. Boundary at the Trailing-edge of the Airfoil

For the simulation, Ansys Fluent was employed with a pressure-based segregated solver under the pressure correction SIMPLE algorithm, which accounted for the pressure-velocity coupling. A second-order spacial discretization scheme for the pressure derivative was used along with a second-order upwind discretization scheme for the advective velocity derivative and diffusive turbulent viscosity terms. A cell-based approach was used for the convective and diffusive gradients. A second-order implicit time integration was used for the temporal discretization at a minimum convergence criteria of $1e-07$. A relatively small time step was used (ensuring algorithm stability) to properly model the transient phenomena. An SST- $k-\omega$ turbulence model was deployed as a conjugate solution of the two transport equations for k and ω for the evaluation of the eddy viscosity [17].

Results and Discussion

Figure 6 shows the coefficient of performance, C_p , comparison between the qualitative accuracy of the algorithm compared with the reference turbine. The C_p was evaluated from the fraction of the captured turbine power to the total available incoming wind power. A good approximation of the turbine performance up to the TSR value of five was observed, along with a slight over-estimation beyond that value. It should be noted that the algorithm took into account a varying interference factor as a function of the azimuth angle, but did not consider the vertical variation of the free-stream velocity. This explains the difference between the two results.

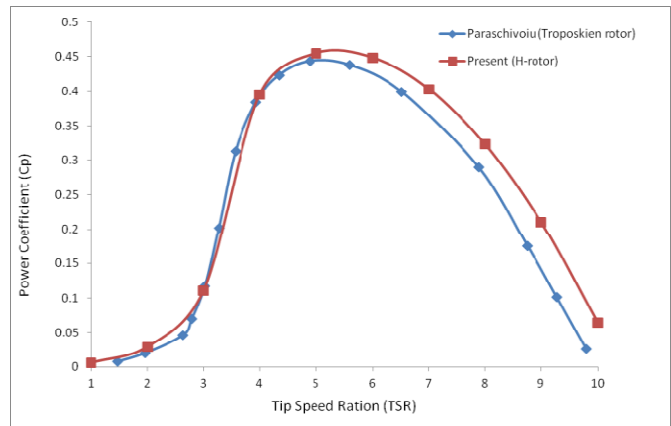


Figure 6. Comparison between the Current DMST Results and those found by Paraschivoiu et al. [17]

Figure 7 shows the C_p comparison between the CFD and DMST models. The C_p from the CFD analysis was found from the data file is reported here containing the dimensionless moment coefficient, C_m , per unit length. The torque and

power coefficients were calculated using Equations (17) and (18):

$$C_T = \frac{T}{\frac{1}{2}\rho U^2 AR} \quad (17)$$

$$C_p = \frac{T\omega}{\frac{1}{2}\rho U^3 A} \quad (18)$$

where, A and R are the area of the turbine and the radius, respectively; and, C_T and C_p are the torque and power coefficients.

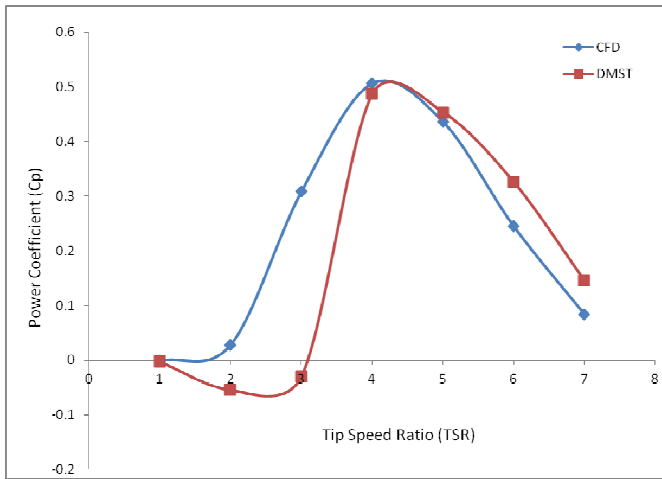


Figure 7. Power Coefficient Results for the DMST and CFD Models

As can be seen, both CFD and DMST model C_p curves show minimum torque for lower tip speed ratios. The DMST model underestimates the C_p value at lower tip speed ratios but predicted higher C_p values at higher tip speed ratios agree with results obtained by Salim and Cheah [17].

Effect of Blade profile: Darrieus VAWT has a positive angle of attack α at the front side of the rotor and a negative angle α at the back side, one has to use symmetrical airfoils. Three symmetric airfoils NACA 0015, NACA 0018, NACA 0021 which are frequently used for Darrieus VAWT are examined in this study. These airfoils have lower maximum lift coefficients if they are compared to asymmetrical airfoils of the same thickness. To realize a certain lift one must therefore use a larger chord.

From Figure 8, it can be seen that the self-starting behavior was improved with thicker airfoils (NACA 0021). The maximum efficiency of NACA 0021 is around 0.4657 at a TSR of 4; however, beyond TSR 4, the performance of the thicker blade becomes a disadvantage, as far as efficiency is

concerned. It can also be observed that the results of NACA 0015 and NACA 0018 are close to each other, but the NACA 0018 has better starting performance, due to its thicker section.

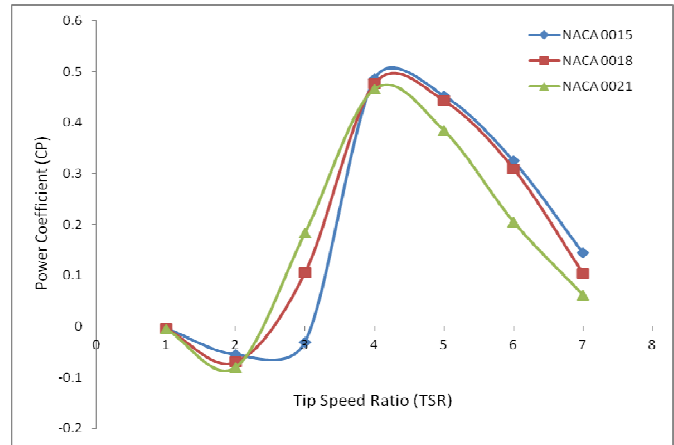


Figure 8. Power Coefficient for the Three Airfoils

Effect of number of blades: Figure 9 shows the effect of number of blades on C_p as a function of the tip speed ratio. As can be observed, the peak of C_p decreases as the number of blades increases. It can be said that a larger number of blades yields the maximum C_p for lower tip speed ratios, but yet are not as efficient compared to 3-bladed turbines. It can also be said that a larger number of blades improves starting performance of the turbine. For the 2-bladed turbines, though, it generates more power at higher tip speed ratios. Practically, then, the high rotational speed produces excessive vibration and, consequently, more noise and is not an optimal solution for urban installation. VAWTs with larger numbers of blades achieve maximum power at TSR; however, more blades will eventually decrease C_p .

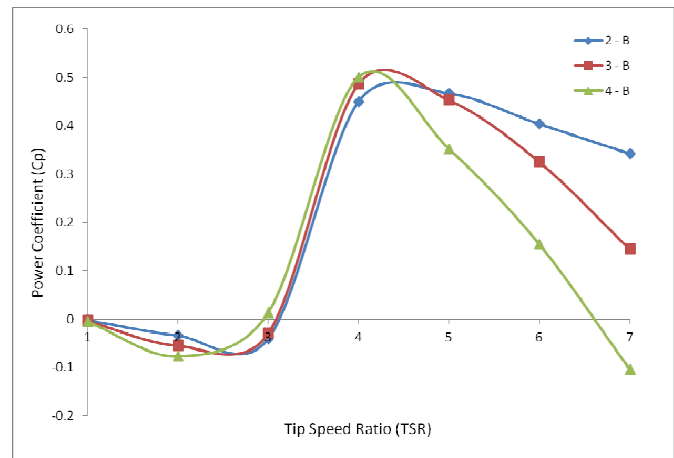


Figure 9. Power Coefficient as a Function of TSR for 2-, 3-, and 4-bladed Rotors

Figure 10 shows the evolution of instantaneous torque coefficient of the 2-bladed, 3-bladed, and 4-bladed turbines at a TSR of 3. It can be seen that, as the number of blades increases, the torque coefficient decreases. In a complete 360° rotation of the turbine, the number of periods becomes higher, as the number of blades increases, thereby creating a blocking effect and hindering air flow through the turbine. From the CFD analysis, the contour of vorticity, as shown in Figure 11, can be observed for 2- and 4-bladed turbines. This explains the decrease in the peak of the torque coefficient and power coefficient as the number of blades increases. It should be noted that this analysis was based on a 2D model, which is better suited to a straight-bladed turbine. Curved or twisted turbine blades mandate 3D treatment or a 2D piecewise layer-by-layer approach to account for the change in radius and angle of attack. Nevertheless, the 2D model captures the essence of the flow behavior and the trend, and considers a valuable conceptual design tool by avoiding the intensive computational demand and lead time of 3D preprocessing.

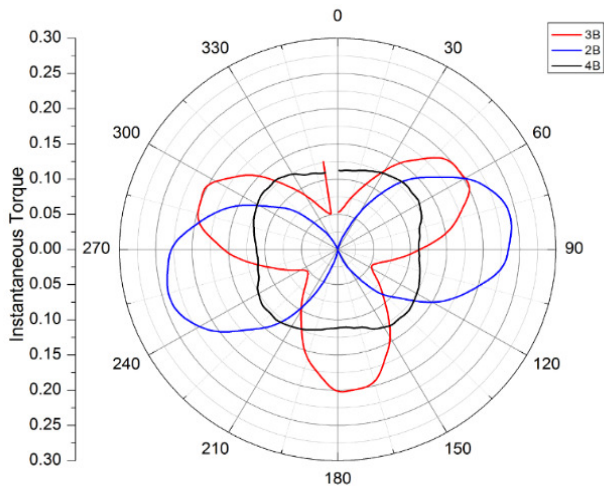
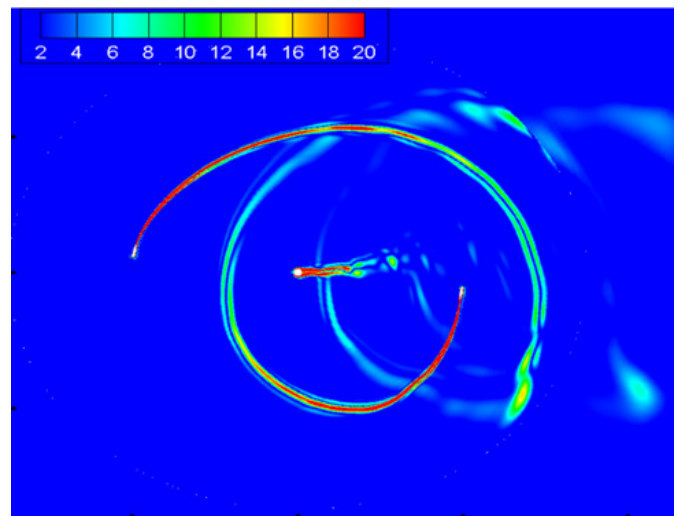


Figure 10. Instantaneous Torque Coefficient at TSR 3 for 2-, 3-, and 4-bladed Rotors

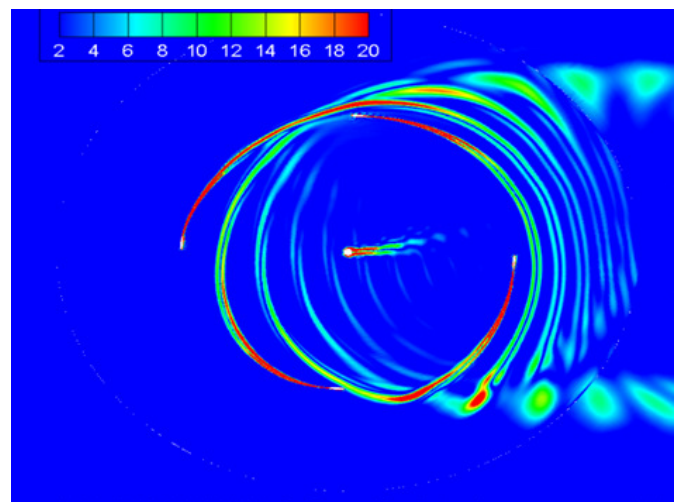
Conclusions

A low-fidelity analysis tool based on a double-multiple stream model was built using an extended airfoil database. It was validated using existing literature and a high fidelity numerical simulation based on Unsteady Reynolds Averaged Navier-Stokes equation. The results showed that the double-multiple stream tube (DMST) model was not suitable for high-solidity turbines and most suitable for low-solidity wind turbines. The disadvantage is that low-solidity turbines are not very applicable for built-in environments, due to its large radius, the anticipated high rotational speed,

and associated noise. When the C_p values obtained from DMST and CFD analyses were compared, they showed that negative and/or minimum C_p and torque values are generated at lower tip speed ratios, which implies that NACA 0015, NACA 0018, and NACA 0021 airfoils are not self-starting. Nevertheless, NACA 0021 was shown to have better starting performance than the other two airfoils, due to its thicker section. CFD results were found to be more accurate and the flow physics like vorticity could be easily visualized. One major advantage of a low-fidelity analysis is that it can be used to determine an appropriate parameter for turbine performance before performing timely and expensive computations and experiments.



(a) Two-bladed Turbine Wake



(b) Four-bladed Turbine Wake

Figure 11. Vorticity Contours of 2- and 4-bladed Rotating Turbines

References

- [1] Bhutta, M. M., Hayat, N., Farooq, A. U., Ali, Z., Jamil, S. R., & Hussain, Z. (2012). Vertical Axis Wind Turbine – A Review of Various Configurations and Design Techniques. *Renewable and Sustainable Energy Reviews*, 16(4), 1926–1939.
- [2] Islam, M., Ting, D., & Fartaj, A. (2008). Aerodynamic Models for Darrieus-type Straight-bladed Vertical Axis Wind Turbines. *Renewable and Sustainable Energy Reviews*, 12(4), 1087–1109.
- [3] Paraschivoiu, I. (2002). Chapter 6: Double Actuator Disk Theory. In S. Schettini (Ed.), *Wind Turbine Design: With Emphasis on Darrieus Concept* (1st ed.), (pp. 147-259). Montreal, Canada: Presses Internationales Polytechnique.
- [4] Templin, R. (1974). *Aerodynamic Performance Theory for the NRC Vertical-Axis Wind Turbine*. United States.
- [5] Strickland, J. (1975). *The Darrieus Turbine: A Performance Prediction Model Using Multiple Streamtubes*. Albuquerque.
- [6] Paraschivoiu, I. (1981). Double-Multiple Streamtube Model for Darrieus in Turbines. *NASA Lewis Research Center Wind Turbine Dynamics*, 19-25.
- [7] Larsen, H. (1975). Summary of a Vortex Theory for the Cyclogyro. *Proceeding of the Second US National Conferences on Wind Engineering Research*, (pp. 1-3). Colorado.
- [8] Strickland, J., Webster, B., & Nguyen, T. (1979). A Vortex Model of the Darrieus Turbine: An Analytical and Experimental Study. *Journal of Fluids Engineering*, (5), 101-500.
- [9] Pawsey, N. (2002). *Development and Evaluation of Passive Variable-Pitch Vertical Axis Wind Turbine*. The University of New South Wales, Mechanical and Manufacturing Engineering.
- [10] Dobrev, I., & Massouh, F. (2012). Exploring the Flow around a Savonius Wind Turbine. *International Symposium on Applications of Laser Techniques to Fluid Mechanics*, 16, 9-12.
- [11] Mohamed, M. (2012). Performance Investigation of H-rotor Darrieus Turbine with New Airfoil Shapes. *Energy*, 47(1), 522–530.
- [12] Howell, R., Qin, N., Edwards, J., & Durrani, N. (2010). Wind Tunnel and Numerical Study of a Small Vertical Axis Wind Turbine. *Renewable Energy*, 35(2), 412–422.
- [13] Janajreh, I., Talab, I., & Macpherson, J. (2010). Numerical Simulation of Tower Rotor Interaction for Downwind Wind Turbine. *Modelling and Simulation in Engineering*, 2010, 1-11.
- [14] Yao, Z. Q., & Yang, C. L. (2013). Numerical Simulation of Unsteady Flow for Variable-Pitch Vertical Axis Wind Turbine. *Applied Mechanics and Materials*, 291-294, 490-495.
- [15] Castelli, M. R., Englaro, A., & Benini, E. (2014). A Proposal for a New Xfoil-Based Hybrid Extended Polar for Wind Turbine Applications. *ASME Journal of Solar Energy Engineering*.
- [16] Paraschivoiu, I., Trifu, O., & Saeed, F. (2009). H-Darrieus Wind Turbine with Blade Pitch Control. *International Journal of Rotating Machinery*, 2009, 1-7.
- [17] Salim, S. M., & Cheah, S. C. (2009). Wall y+ Strategy for Dealing with Wall-bounded Turbulent Flows. *Proceedings of the International MultiConference of Engineers and Computer Scientists*, (pp. 2). Hong Kong.

Biographies

FRANKLYN KANYAKO is currently a Ph.D. candidate at Masdar Institute in Abu Dhabi, UAE. He is well-versed in wind turbine performance and analysis. His M.S. thesis work was on the development of low- and high-fidelity models for vertical wind turbines. Mr. Franklyn Kanyako may be reached fkanyako@masdar.ac.ae

ISAM JANAJREH is currently an Associate Mechanical Engineering Professor and the director of the wind and waste to energy lab at the Masdar Institute. He is an internationally recognized expert in the area of multiphysics flow, wind energy, and waste to energy, particularly in the feedstock characterization thermochemical pathways, including gasification and pyrolysis. He has authored more than 80 publications on the subject and appeared in over 80 conferences. Dr. Janajreh may be reached at ijana-jreh@masdar.ac.ae

SPACE PERCEPTION AND NAVIGATION ASSISTANCE FOR THE VISUALLY IMPAIRED USING DEPTH SENSORS AND HAPTIC FEEDBACK

Kumar Yelamarthi, Central Michigan University; Kevin Laubhan, Central Michigan University

Abstract

Lightweight and low-cost 3-dimensional depth sensors have gained much attention in the computer vision and gaming industry. While their performance has been proven to be successful in the gaming industry, these sensors have not been utilized successfully for assistive devices. Leveraging on this gap, this study focused on the design, implementation, and evaluation of a depth-sensor-based navigation assistive device for the visually impaired. The proposed portable embedded system interprets the field-of-view, converts it into a depth matrix, and processes the information in order to recognize objects, humans, and to provide relevant haptic feedback for navigation of the visually impaired. Through design and evaluation, the proposed system was shown to successfully identify, detect, and track the closest objects, including humans, and perform real-time distance measurements.

Introduction

The World Health Organization (WHO) estimates that 285 million people are visually impaired worldwide [1], and the U.S. Census Bureau reported that 54 million people live with disabilities [2]. While many of these individuals live and interact independently, it is reported that the majority lack the ability to live and function independently. One of the major issues these individuals face is their inability to interpret surroundings and identify obstacles in their path of commute. This challenge led to the introduction of many assistive devices for navigation assistance, with the two most common being white canes and guide dogs [3]. The white cane is only partially effective as it does not detect objects above about knee height, and does not provide cues in sufficient time to avoid a collision in a populated area. As for the guide dog, unfortunately, not all visually impaired individuals have access to dogs, due to an ongoing shortage of properly trained dogs.

Research has demonstrated that assistive technologies can be used to help more people with disabilities to become a part of regular learning environments [4]. This, when combined with the number of calls from blind individuals for impending action in the design of assistive devices [5]. This

current study focused on a depth-sensor-based haptic feedback system, as shown in Figure 1, which belongs to the category of vision substitution. This haptic feedback system helps blind people overcome challenges of dependence, and lets them participate in more social and civic activities to improve their quality of life.



Figure 1. Prototype of the Haptic Feedback System on a User

Literature Review

Over the past three decades, research has been conducted to design new navigation devices [6-29]. Benjamin et al. [7] built a laser cane that used optical triangulation with three laser diodes. The first laser pointed at the ground, detecting a drop in elevation; the second pointed straight in front of the user and parallel to the ground; the third pointed straight ahead at an angle of 45 degrees from the ground in order to protect the user from overhanging obstacles. Bissit and Heyes [8] developed a hand-held sonar device to give the

user auditory feedback with eight discrete levels. Bousbia-Salah et al. [9] proposed a method of detecting obstacles on the ground through an ultrasonic sensor integrated on the white cane and the user's shoulders. Shoval et al. [10] proposed a navigation belt made up of an array of ultrasonic sensor to detect obstacles, but it was not an ideal method for operation in dense and noisy environments. Na [11] proposed an interactive guide system for indoor positioning. Wong et al. [12] proposed using virtual reality technology to capture images of the house via cameras, and use this information for indoor navigation. Kulyukin et al. [13] proposed a robot-assisted navigation method for indoor environments.

Vision-based situational awareness and haptic feedback systems were proposed and implemented by many researchers. Castells et al. [14] used a vision sensor to detect possible obstacles in order to supplement the feedback provided by a traditional white cane. They used the images to detect sidewalk borders and obstacles in a predefined window, but the system had poor accuracy in dense environments. Sainarayanan et al. [15] presented a fuzzy-clustering-based algorithm to identify obstacles in the path and provide feedback to the user through stereo earphones, but their system required high computational power, and it was difficult for the user to comprehend signals in a noisy environment. Filipe et al. [16] presented a depth-sensor-based system but did not present any mechanism to provide feedback to the user for navigational assistance. Khoshelham and Elberink [17] presented the depth-sensor-based approach for indoor mapping of objects but did not include a feedback system for effective navigation. Han et al. [18] presented an overview of applications from a similar depth sensor but did not provide a solution for navigation and feedback. Zeng et al. [19] and Ishiwata et al. [20] presented an exploration and avoidance system with haptic feedback that used an expensive time-of-flight camera for obstacle detection, limiting its adoptability, due to economic constraints.

Also, many of these existing systems increase the user's navigation-related physical load, as they require the user to wear heavy body gear, contributing to physical fatigue. Based on the principles of universal design, the navigation-based assistive devices for the blind should encompass design characteristics such as equitable use and flexibility, be simple and intuitive, offer perceptible information, be portable, and allow for periodic updates.

Design and Implementation

Figures 2 and 3 show the architecture and data flow for the proposed haptic feedback system (HFS). The first module in the architecture was an ASUS Xtion Pro depth sensor

for scanning the environment for the user. It could also filter the visual scene to generate a depth profile. This was accomplished through PrimeSense's 3-D sensors, which used light coding to code the scene with the aid of active infrared illumination [23]. The coded light was processed through the built-in chip to obtain depth information of the environment [5]. With a horizontal field of view of 57 degrees and a vertical field of view of 43 degrees, a distance map across the user was generated in an image with a resolution of 640 x 480 pixels at 60 fps.

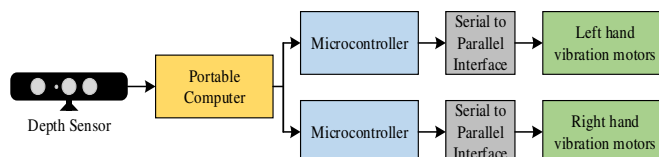


Figure 2. Architecture of the Haptic Feedback System

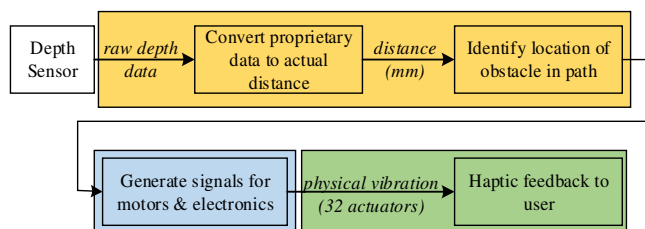


Figure 3. Data Flow and Manipulation

The second module in the proposed system was a portable computer that could decode the proprietary data from the sensor into a meaningful format through a custom java-based program running on the Processing Integrated Development Environment (PIDE) [30] and the open-source SimpleOpen NI library [31]. This portable computer obtained the depth images generated by the depth sensor and decoded them into a matrix of 640 x 480 elements, with each element representing the distance to the object with respect to the user. Upon generating this matrix, it divided this into eight smaller zones, four on the left (L1, L2, L3, and L4) and four on the right (R1, R2, R3, and R4), each corresponding to a respective column in the vibration module. Then, it used the nearest neighbor algorithm to find the location of the nearest obstacle with respect to the user and generated appropriate signals for the haptic feedback unit.

Furthermore, the system could also identify whether the obstacles were static or dynamic and provide real-time information to the user through an audio feedback system. Once the location and distance information of the nearest obstacle were found through the custom java program in PIDE, an Arduino microcontroller generated signals to actuate the appropriate vibration motors. As the number of vibration motors far exceeded the number of available output ports on the microcontroller, a 16-bit input/output (I/O) ex-

pander was used to decode the information from the I2C bus of the microcontroller. This I/O expander transmitted this information to the left-hand and right-hand vibration modules to activate the respective number of actuators.

The left-hand and right-hand vibration modules were arrays of shaftless, 8 mm motors woven into gloves, and served as a vibrotactile feedback delivery mechanism. Figure 4 shows the architecture of the haptic feedback system with 16 motors woven into the left-hand glove (one column of four motors into each finger sleeve). Figure 5 shows the prototype board with all of the electronics. Figure 6 shows the wiring connections of the motors in the glove. These motors vibrated based on the signal generated from the I/O expander, which inherently was generated based on the presence of the obstacle that was within the depth sensor's field of view. For instance, if a static obstacle were found in zones L1 and L2 of the sensor's field of view, motors in the first two columns of Figure 4 would vibrate, with the number of vibrating motors inversely proportional to the proximity of the obstacle. Also, while operating in a densely populated environment, this feedback system could be used to inform the blind user of the location of an open space or a direction to pursue in order to avoid a collision during a commute.

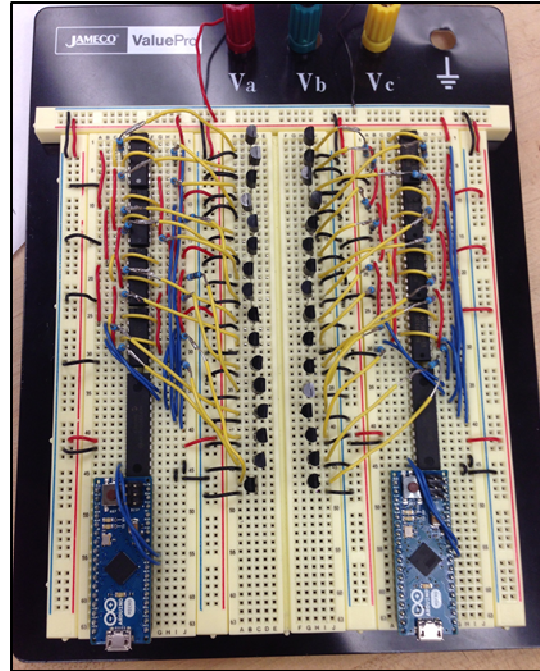


Figure 5. Prototype Board with the Electronics of the Proposed System

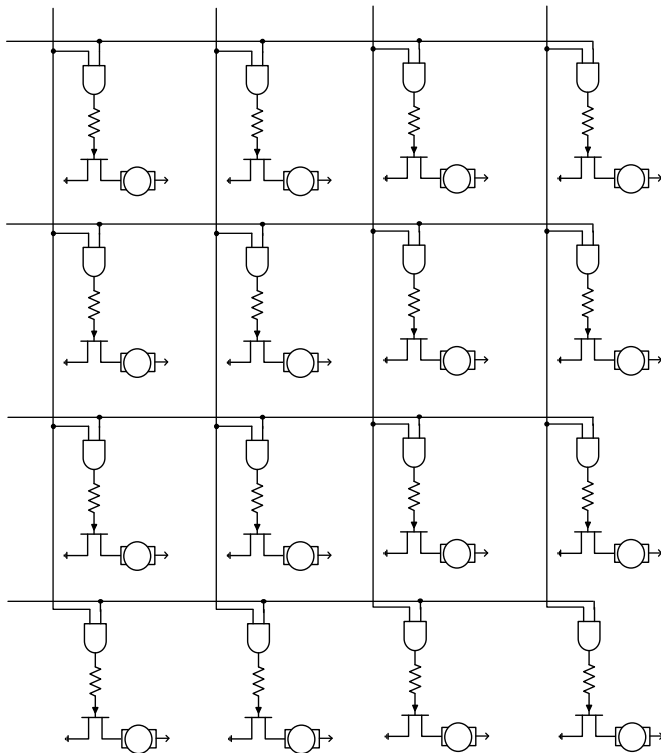


Figure 4. Architecture of the Haptic Feedback Array



Figure 6. Vibration Motors in the Left-hand Glove

Testing and Evaluation

To validate the fundamental operation and feasibility of the proposed system, it was subjected to multiple tests with different programs, each designed to perform a specific task. Any of these programs could be combined to perform a combination of tasks as well. Due to the infeasibility of visually demonstrating the operation of the vibration motors here, a simplified test system of motors replaced by LEDs is presented here.

Test 1: Identify the closest object

In this test, the system was programmed to obtain the depth matrix, filter the data to identify the closest single point in its field of view, and turn on the appropriate number of LEDs with respect to distance of closest object from the system. Figure 7 shows the depth image, as obtained from the sensor, and the zone partitions (L1, L2, L3, L4, R1, R2, R3, and R4). Upon filtering and data processing from this image, the closest single point (marked with a red dot) was detected in zone L3. This information was transmitted to the left-hand microcontroller, which activated two LEDs in zone L3 through the I/O expander, as presented in Figure 8. It should be noted that this test was designed to represent the system's ability to detect only the closest point in the field of view, not the whole object or a human, which will be performed in a future test. With the primary goal of this test being identification of closest object, when multiple objects at similar distances are identified in different zones, appropriate motors/LEDs in respective will be activated to inform the user accordingly.

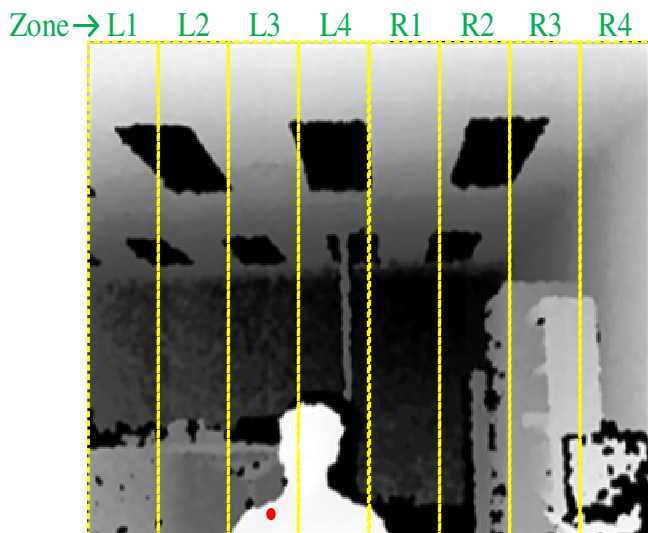


Figure 7. Depth Image for the Closest-object Detection Test

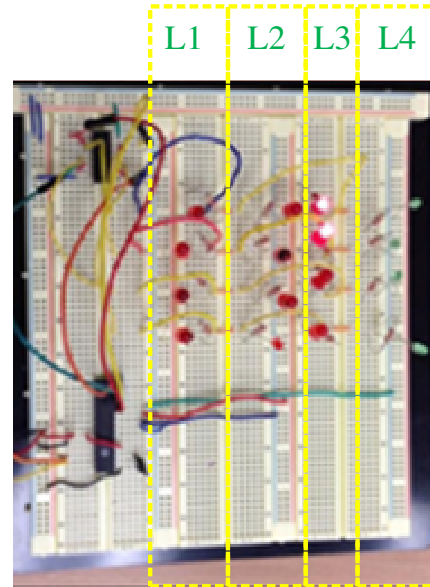


Figure 8. Verification of the Closest-object Detection Test

Test 2: Identify humans

While Test 1 was designed to merely identify an object, it cannot distinguish between a physical object and a human. With human detection being a fundamental requirement in navigation assistance devices, Test 2 was drafted to scan the field-of-view, distinguish between physical objects and humans, and inform the user about the proximity and location of a human. Figure 9 shows the depth image, as obtained from the sensor, zone partitions, human detected (marked with in blue), and their respective center of mass (marked with a red dot) in zone L3. This information was transmitted to the left-side microcontroller in order to activate three LEDs in zone L3 through the I/O expander, as presented in Figure 10. Furthermore, extended tests were performed to evaluate efficiency of the system in detecting both static and dynamic (walking) humans, as presented in Table 1. The total time from start of program to providing feedback through the motors/LEDs in this test was found to be approximately 2.5 seconds, an acceptable time in real-time navigation when compared to results from other studies [19, 32].

Test 3: Measure the distance between points

As it is not uncommon for humans to stretch their hands while walking, this test was designed to identify if any humans in the path of navigation had stretched their hands, and mark this region as a no-pass region. If so, the system identified the location of the human, measured the distance between the two hands, and informed the blind user so that he/she could navigate around the obstacle in his/her path. The depth image, obtained from this test, is shown in Figure 11, where the presence of a human is marked in blue, and

the red dots represents the location of the head, center of mass, left hand, and right hand, and the distance between the two hands, presented in mm on the left side (mag: 1373.8055), validating that the proposed system could identify movement of humans in real-time.

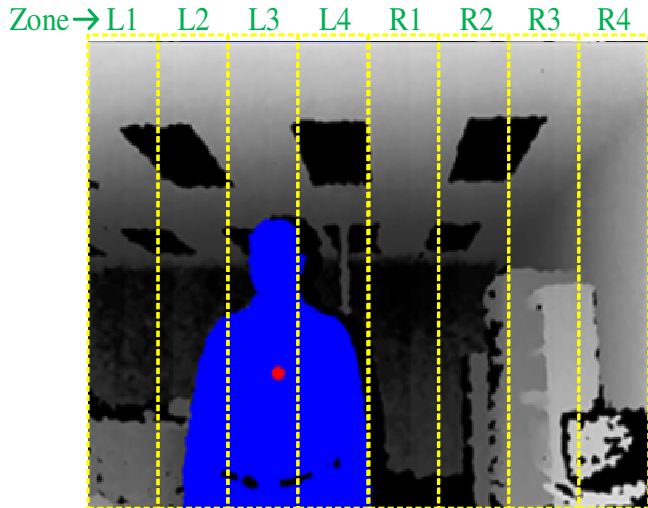


Figure 9. Depth Image for the Human Detection Test

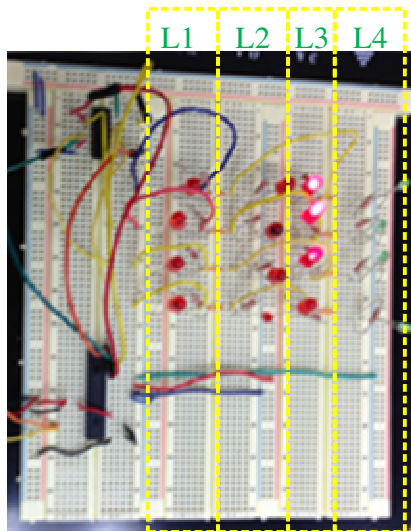


Figure 10. Verification of the Human Identification Test

Table 1. Human Detection Time Results

Distance to Human (m)	Average Detection Time (sec)	
	Static Human	Dynamic/Walking Human
1.0	1.144	0.859
2.0	2.114	0.529
3.0	2.572	1.660
4.0	1.517	1.568
5.0	2.535	1.254

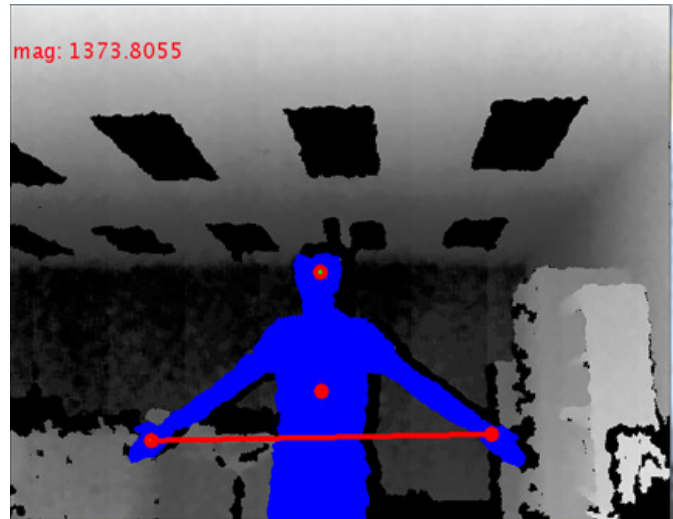


Figure 11. Depth Image for the Test of Distance Measurement between Two Points

Test 4: Dynamically find the closest objects

This test was designed to extend the results found in Test 1. A new algorithm was developed to dynamically detect multiple obstacles. Each motor in a column was designed to turn on when an object was found within a certain threshold, similar to Test 1. The depth image was scanned in order to detect the closest object in each zone, L1-L4 and R1-R4, and inform the user accordingly. Unlike the results in Test 1 (see Figure 7), this test could detect that the closest object was present in zones L3, L4, and R1, and would activate the LEDs accordingly. The number of LEDs that turn on for each zone varied, based on distance of the closest object in each zone (four LEDs for distances of less than 50.0 cm, three LEDs for 50.1- 61.0 cm, two LEDs for 61.1-91.5cm, and one LED for 91.6-122.0 cm).

Test 5: Detection probability for diverse objects

As detection of static objects is equally important as detecting humans, a different test was performed to evaluate the detection probability of diverse objects at various distances. Two key metrics in real-time navigation are the probability of detection accuracy and distance measured. Accordingly, diverse objects were placed at different distances (1 m, 2 m, 3 m, 4 m, and 5 m) and the test program was executed to obtain 1000 measurements for each object-distance combination. Results of the probability of detection and average error in distance measured from this test, presented in Table 2, clearly demonstrate the efficiency of the proposed system. While the system was able to detect objects of household materials such as Styrofoam, plastic, cotton, aluminum, and rubber with a probability of nearly 1.0, the nature of the infrared signals emitted by the depth sensor were absorbed by steel, thus drastically limiting its performance. Lastly, the processing latency of each of these tests was evaluated

and found to be in the range of 1.8 sec – 2.9 sec, with an overall average of 2.1 sec, an acceptable value when compared with previous studies [19, 30].

Table 2. Probabilities of Object Detection

Material	Probability of Detection					Average Distance Error (%)
	1m	2m	3m	4m	5m	
Styrofoam	1.00	1.00	1.00	1.00	1.00	3.67
Solid Plastic	1.00	1.00	1.00	1.00	0.98	1.02
Cotton	1.00	1.00	1.00	1.00	1.00	0.97
Aluminum	1.00	1.00	1.00	1.00	1.00	0.75
Rubber	1.00	1.00	1.00	0.87	0.02	0.73
Steel	1.00	0.40	0.80	0.91	0.00	1.45
Water Bottle	0.02	0.00	0.00	0.00	0.00	4.01
Trash Bag	1.00	1.00	0.32	0.03	0.00	5.70
Static Human	1.00	1.00	1.00	1.00	1.00	2.23

Conclusions

In this paper, the authors presented the design, implementation, and evaluation of a simple, light, and low-cost depth-sensor-based haptic feedback system. The proposed system proved that it could overcome challenges of computational power, comprehension of signals in noisy environments, and heavy body gear, as presented in the previous study. Through testing, the prototype was demonstrated to: i) detect the presence and location of obstacles in the path of navigation; ii) identify an obstacle-free path in the field of view for the user to follow for safe navigation in a crowded environment; and, iii) detect obstacles in the navigation path in real-time.

Further testing can be done to gather more qualitative and quantitative data on user reaction time to process the signals, as well as overall ability to navigate. This will be done upon obtaining approval from the Institutional Review Board (IRB), as it involves human subjects. Optimization of the proposed algorithms will be performed for implementation on a portable microcontroller, such as Raspberry Pi, to further improve portability. Overall, while designed and implemented as a navigation system for the blind, the proposed architecture has a broad range of applications including, but not limited to, body tracking for clinical assessment and monitoring, body tracking during rehabilitation, and touchless interaction in image-guided interventional medical treatment.

References

- [1] World Health Organization. (2013). Visual Impairment and Blindness, *Fact Sheet N°282*.
- [2] National Council on Disability. (2013). *National Disability Policy: A Progress Report*.
- [3] Kirchner, C. (1995). Alternate Estimate of the Number of Guide Dog Users. *Journal of Visual Impairment & Blindness, Part 2, JVIB News Service, 89(2)*, 4-6.
- [4] Cavanaugh, T. (2002). The Need for Assistive Technology in Educational Technology. *Educational Technology Review, 10(1)*.
- [5] Baldwin, D. (2003). Wayfinding Technology: A Road Map to the Future. *Journal of Visual Impairment & Blindness, 97(10)*, 612-620.
- [6] Parry, D., Jennings, H., Symonds, J., Ravi, K., & Wright, M. (2008). Supporting the Visually Impaired using RFID Technology. *Proceedings of the Health Informatics New Zealand Annual Conference and Exhibition*.
- [7] Benjamin, J. M., Ali, N. A., & Schepis, A. F. (1973). A Laser Cane for the Blind. *Proceedings of the San Diego Medical Symposium*.
- [8] Bissit, D., & Heyes, A. (1980). An Application of Biofeedback in the Rehabilitation of the Blind. *Applied Ergonomics, 11(1)*, 31-33.
- [9] Bousbia-Salah, M., Bettayeb, M., & Larbi, A. (2011). A Navigation Aid for Blind People. *Journal of Intelligent & Robotic Systems, 64(3)*, 387-400.
- [10] Shoal, S. S., Borenstein, J., & Koren, Y. (1998). Auditory Guidance with the Navbelt - A Computerized Travel Aid for the Blind. *IEEE Transactions on Systems, Man, and Cybernetics, 28(3)*, 459-467.
- [11] Na, J. (2006). The Blind Interactive Guide System using RFID-Based Indoor Positioning System. *Lecture Notes in Computer Science, 4061(2006)*, 1298-1305.
- [12] Wong, F., Nagarajan, R., & Yaacob, S. (2003). Application of Stereovision in a Navigation Aid for the Blind People. *Proceedings of ICICS-PCM*.
- [13] Kulyukin, V., Gharpure, C., Nicholson, J., & Osborne, G. (2006). Robot-Assisted Wayfinding for the Visually Impaired in Structured Indoor Environments. *Autonomous Robots, 21(1)*, 29-41.
- [14] Castells, D., Rodrigues, J. M. F., & du Buf, J. M. H. (2010). Obstacle Detection and Avoidance on Sidewalks. *Proceedings of the International Conference on Computer Vision, Theory and Applications, 2*, 235-240.
- [15] Sainarayanan, G., Nagarajan, R., & Yaacob, S. (2007). Fuzzy Image Processing Scheme for Autonomous Navigation of Human Blind. *Applied Soft Com-*

- puting, 7(1), 257-264.
- [16] Filipe, V., Fernandes, F., Fernandes, H., Sousa, A., Parades, H., & Barroso, J. (2012). Blind navigation support system based on Microsoft Kinect. *Procedia Computer Science*, 94-101.
- [17] Khoshelham, K., & Elberink, S. O. (2012). Accuracy and Resolution of Kinect Depth Data for Indoor Mapping Applications. *Sensors*, 12, 1437-1454.
- [18] Han, J., Shao, L., Xu, D., & Shotton, J. (2013). Enhanced Computer Vision With Microsoft Kinect Sensor: A Review. *IEEE Transactions on Cybernetics*, 43(5), 1318-1334.
- [19] Zeng, L., Prescher, D., & Weber, G. (2012). Exploration and avoidance of surrounding obstacles for the visually impaired. *Proceedings of the 14th international ACM SIGACCESS conference on Computers and accessibility*, 111-118.
- [20] Ishiwata, K., Sekiguchi, M., Fuchida, M., & Nakamura, A. (2013). Basic study on step detection system for the visually impaired. *IEEE International Conference on Mechatronics and Automation*, 1332-1337.
- [21] Yelamarthi, K., Haas, D., Nielsen, D., & Mothersell, S. (2010). RFID and GPS Integrated Navigation System for the Visually Impaired. *Proceedings of the IEEE MWSCAS*, (pp. 1149-1152).
- [22] Dancer, K., Martin, W., Rock, K., Zeleny, C., & Yelamarthi, K. (2009). The Smart Cane: An Electrical Engineering Design Project. *Proceedings of the ASEE NCS Conference*.
- [23] Shpunt, A., & Pesach, B. (2010). *Optical Pattern Projection*. (US Patent App.12/840,312).
- [24] Ando, B., Baglio, S., & Pitrone, N. (2008). A Contactless Haptic Cane for the Blind People. *Proceedings of the 12th IMEKO TCI & TC7 Joint Symposium*.
- [25] Moro, F., Fontanelli, D., & Palopoli, L. (2013). Vision-Based Robust Localization for Vehicles. *Proceedings of I2MTC*, (pp. 553-558).
- [26] Nazemzadeh, P., Fontanelli, D., & Macii, D. (2013). An Indoor Position Tracking Technique based on Data Fusion for Ambient Assisted Living. *Proceedings of CIVEMSA*, (pp. 7-12).
- [27] Prattichizzo, D., Chinello, F., Pacchierotti, C., & Malvezzi, M. (2013). Towards Wearability in Fingertip Haptics: A 3-DoF Wearable Device for Cutaneous Force Feedback. *IEEE Transactions on Haptics*, 6(4), 506-516.
- [28] Yelamarthi, K. (2014). An Autonomous Passive RFID-assisted Mobile Robot System for Indoor Positioning. *International Journal of Modern Engineering*, 14(2), 28-37.
- [29] Thamma, R., Kesireddy, L. M., & Wang, H. (2012). Centralized Vision-Based Controller for Unmanned Guided Vehicle Detection. *International Journal of Modern Engineering*, 12(2), 58-65.
- [30] Processing Development Environment (n.d.). Retrieved from <https://processing.org/>
- [31] Simple OpenNI (n.d.). Retrieved from <https://code.google.com/p/simple-openni/>
- [32] Ridwan, M., Choudhury, E., Poon, B., Amin, M. A., & Hong, Y. (2014). A Navigational Aid System for Visually Impaired using Microsoft Kinect. *Proceedings of the International Multi Conference on Engineers and Computer Scientists*.

Biographies

KUMAR YELAMARTHI received his Ph.D. degree from Wright State University in 2008. He is currently an Associate Professor of Electrical and Computer Engineering at Central Michigan University. His research interest is in the areas of embedded systems, robotics, computer vision, integrated circuit optimization, and engineering education. He has served as a technical reviewer for several international conferences and journals, and has published over 75 articles in archival journals and conference proceedings in these areas. He is a member of Tau Beta Pi engineering honor society and Omicron Delta Kappa national leadership honor society, and a senior member of IEEE. He may be reached at k.yelamarthi@ieee.org

KEVIN LAUBHAN is currently an undergraduate student currently working towards his Bachelor of Science degree in Computer Engineering at Central Michigan University, with an anticipated graduation in May, 2016. Mr. Laubhan may be reached at laubh1kc@cmich.edu

CAPSTONE PROJECT: PLC CONTROL SYSTEM WITH INTEGRATED PID CONTROLLER FOR CONTROL SYSTEM OPTIMIZATION

Abdullah Al Atwa, Michigan Technological University; Ian Bumgardner, Michigan Technological University; Mohammed Bushlaibi, Michigan Technological University; Steven Castello, Michigan Technological University; Joshua Erickson, Michigan Technological University; Aleksandr Sergejev, Michigan Technological University; Mohsen Azizi, Michigan Technological University

Abstract

A programmable logic controller (PLC) with a proportional-integral-derivative (PID) controller is a simple and effective way to increase the efficiency of a control system. In this paper, the authors discuss the development of a control system and the analysis of a PID controller used for system voltage regulation. The system was also to be used as an educational tool for PLC instruction. The system implemented PLC and PID control in order to increase the efficiency of LED lighting adjustments to voltage changes to keep the voltage level at a desired set point. The system in this study contained four key components that made up the control system, which included a solar panel, a stepper motor, LED lights and a PLC/HMI. The solar panel voltage was an input to the PLC, which reads the input voltage then calculated the desired LED output. As a result of the voltage changes, the illumination from the LEDs would try to compensate for the solar panel voltage change. The implementation of P, PI and PID controllers was used to optimize system performance.

Introduction

The capstone project course is an intrinsic part of the undergraduate education. The capstone projects are widely regarded as an excellent mechanism for assessing the outcomes of engineering and engineering technology programs and can serve as a direct measure of the quality of graduates. Capstone projects provide an opportunity for students to demonstrate their critical thinking skills, communication skills, as well as time and project management skills. The capstone course prepares students to better understand the professional roles in the engineering and technology community [1]. In many universities, senior-level capstone courses have been incorporated as an integral part of engineering and engineering technology education in an effort to correlate the practical aspect of engineering with the curriculum. In such courses, an experiential learning activity is provided in which the practice of engineering in a hands-on project is joined with the analytical knowledge gained from previous courses [2-4]. The development of capstone design courses and corresponding requirements have been influ-

enced by various sources, including the Accreditation Board for Engineering and Technology (ABET), industrial advisory boards (IAB), faculty leading capstone projects, numerous industrial companies, and engineering research.

Earlier research [4-15] showed the importance of industry engagement in capstone projects, which is more than just financial support. However, other kinds of support are common and in most cases necessary, such as equipment, materials, and technical consulting [6-8]. Most industrial sponsors assign a liaison engineer to follow the progress of the project and to assist the students [7], [10]. Other forms of industrial support include awarding meritorious designs and assisting in the evaluation of teams and projects [4]. More recent studies provide further in-depth analysis on the importance of the various benefits of capstone projects for the students' preparation for real-world jobs. These include, among other things, the importance of industry involvement [16-18], familiarizing students with product development process and system engineering [16], [19-23], improvement in the professional skills of students [16], [21], providing multidisciplinary training [16], [22], [24], [25], cultivating creative problem solving skills [16], [26], and preparing students for globalization [16], [27], [28].

Recently, a new trend in conducting capstone projects became noticeable. Some capstone projects are sponsored by faculty members instead of industrial partners playing an important role in support of some larger-scale, externally funded faculty research projects [16]. For example, at Texas A&M University, undergraduate students involved in these projects as a capstone team had to work with graduate students, faculty members, and potential customers. Software, hardware, interface, system integration, and testing all involved other researchers instead of just the capstone team [16]. These types of projects may resemble projects conducted in industrial settings, where multiple divisions have to collaborate on a single, large-scale project.

The intent of this study was to share the development at Michigan Tech of an effective approach for working on the sponsored SD projects. In this paper, the authors present a team of students engaged in the faculty sponsored project with the goal of the development and proof of concept

demonstration of integration of a programmable logic controller (PLC) with a human machine interface (HMI) to create an effective PID controller. Upon completion of the project, the system could be used as a standalone training solution to teach PLC, HMI concepts as well as the theory of the PID controllers in introductory and advanced PLC courses in the EET program at the university. Also described here are the project requirements, the significance of the project, specific project outcomes, and assessment tools used to effectively evaluate student success.

The implementation of a PID controller in a control system can increase the performance of the system. PID control is a control algorithm that is widely accepted and very common among industrial control systems. The PID control algorithm shown in Figure 1 is a closed-loop system in which an input is read and the desired output is computed based on the magnitude, duration, and the rate of change of the error. Three types of gains that are used to respond to the different types of errors: proportional, integral, and derivative. The controller uses these gains to minimize the overall error of the system, which is the difference of the set point and the system output. Proportional gain is related to the magnitude of the error, integral gain is related to the duration of the error, and the derivative gain is related to the rate of change of the error.

The combination of these three gain constants is used to obtain optimal system performance. Therefore, the goal of the system is to try and keep the output value at a desired value called the set point. When the output differs from the set point value, then the system should return the output to the set point as quickly and efficiently as possible. This study was only focused on the PID control objective to “track” a step function; other types of control objectives were outside of the scope of this project and, hence, left for future works. The optimized system should minimize the effect of system perturbations on the output value and keep the output constant at the value of the set point [29], [30].

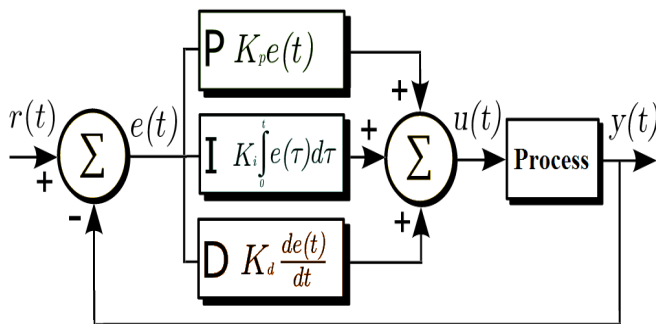


Figure 1. PID Control Algorithm

A PLC is a popular component in which PID control is implemented. A PLC uses inputs of a system to control various system outputs. The main objectives of the system for this study were to implement PID control and to function as a learning tool to teach the different aspects of PLCs and related components. Because of the wide use of PLCs in automated systems in industry, it is important for students to have hands-on experience with the equipment [31]. Systems developed for instructional use and testing of PID controllers are important for training and system improvements. In this study, a PID controller was designed to help illustrate controller effects and the proper settings for a seminar on process controls [32]. To try and improve the PID control an adaptive PID controller was developed using Matlab software [33]. Educational software aimed at PID control was used [34] to help students learn about PID controllers by simulating different processes and allowing the user to change the PID parameters of the controller. It is not always convenient for training to be done in the traditional laboratory environment, so a portable PLC system was developed for training which can be done closer to the job [35]. With systems and instructional tools aimed at the use of PLC and PID controllers, such as the system presented in this paper, users are able to understand and gain experience directly related to real-world applications.

System design included the integration of a solar panel, a stepper motor, and LEDs that were all controlled by a PLC. An HMI was used in the system to allow the user to control various functions. HMIs are popularly used along with PLCs for control systems, where an HMI allows the user to control and monitor the system remotely. The overall function of the current system consisted of the LEDs aimed at the solar panel to produce a measurable output voltage. The system consisted of three LEDs, two control LEDs that were controlled by the PID controller and a perturbation LED that was user-controlled. The system was perturbed by changes in solar panel position and the perturbation LED intensity and rate of change. As a result, the control LEDs were adjusted in order to keep the output of the solar panel at the set point. The perturbations to the solar panel were accomplished by the movement of the stepper motor which was coupled to the solar panel by two gears. The perturbation LED was controlled by ladder logic programs implemented in the PLC. The user was able to control the stepper motor function and the perturbation LED through the HMI interface.

Capstone Course Description

In the past several years EET program in the School of Technology at Michigan Tech was very successful in establishing collaboration with the industry. This, in turn, trig-

gered nearly all the capstone projects conducted in the EET program to be industry sponsored. Only during the last four years, EET program has successfully completed 12 capstone projects with 10 of them being industry sponsored. The benefits of having senior design (SD) projects industry sponsored are very significant for both the students and faculties. On the other hand, the faculty sponsored projects gain popularity as well. Students working on faculty sponsored projects have an opportunity to participate in externally funded research or conduct faculty defined projects resulting in the equipment that can further be used to enhance in class teaching approaches.

A capstone course in the EET program requires the knowledge gained in upper and lower division courses. Students participating in a capstone project practice independent and creative work by completing an engineering design project. Projects are normally team oriented, where the team consists of two to four members, with one member chosen as team leader. Team based capstone projects provide a better practice of industrial environment, to better train today's engineers. Weekly progress reports are required, and the work culminates with a final report and oral presentations, including a poster of the project. As a requirement for graduation, six credits of Senior Project are completed in two three-credit semesters.

Upon completion of the capstone project course, students should fulfill the following course objectives:

- Conduct practical research on electrical engineering technology.
- Research and organize data for synthesis.
- Write reports.
- Deliver oral presentations.
- Work in teams.
- Coordinate and manage resources to meet deadlines.
- Consider economic issues, marketing issues, esthetics, and other non-engineering factors in engineering works.

At the beginning of the first semester team is required to prepare a typed project proposal in a formal memo format, including a proposed timeline. During the course of the project student's team meet with their faculty advisor weekly to discuss the progress report. The weekly formal memo is required the day prior to each weekly meeting and addresses the following three areas: current progress, problems encountered and their resolution, and plan for the following week. To stay on the top of industry requirements sponsoring the project and to receive valuable engineering feedback students conduct by-weekly web conference calls with industry liaison. The oral and written reports due near the end of each semester are to concern themselves with the pro-

gress made in each semester. The one at the end of the first semester will be a progress report, with a full final report due at the end of the second semester. To further improve the quality of capstone projects conducted in the EET program in the School of Technology (SoT) at the Michigan Tech and make students experience as participating in undergraduate research, in the middle of the second semester the team led by the faculty prepares the paper to be further submitted in one of the engineering journals or conference proceedings. In the author's opinion, this experience should become an integral part of any capstone project since it derives an additional benefits previously not included in the capstone environment. First, this requirement makes the students to fill them proud to be engaged in undergraduate research, which in-turn derives more responsibility and teamwork. Second, it provides the students with the opportunity to learn different styles of technical writing following required formats associated with various journals and conference proceedings. The last but not the least, it significantly improves graduates portfolio that while looking for the job can "bring to the table" more than their competitors - applicants.

System Components

The control system consists of 4 main components: a solar panel, a stepper motor, LED lights and a PLC/HMI. Along with the main components there were various sub-components and a constructed system enclosure. The solar panel for the system is a Value Line Series, a VLS-10W solar panel. The PID controller will be used to try and keep the solar panel output voltage at the setpoint of the system. The solar panel is constructed of an anodized aluminum frame with tempered glass that houses the polycrystalline module cells. The solar panel has an open circuit voltage rating of 21.4 V, a maximum power rating of 10W and a maximum power voltage rating of 17.1 V [36]. In choosing a solar panel an important factor was the weight it would bear on the stepper motor. The VLS-10W was an ideal option as it only weighs 1.2 kg/2.6 lbs and has a small area with dimensions of 14.17 in x 10.63 in x 1.38 in.

The SureStep STP-MTR-17060 [37] is a single shaft bipolar stepper motor with 125oz/in of torque, 2amps/phase with a NEMA 17 in2 frame. The required stepper motor holding torque needed to rotate the solar panel was calculated based on the solar panels weight and dimensions. The calculations for the stepper motor torque required for a solar panel weighing 2.7 lbs and dimensions of 14.17 in x 10.63 in x 1.38 in is as follows. We have: Torque (T) = Acceleration (α) \times Inertia (J). The required torque was calculated assuming that the motor must move 60 degrees per second and needs to reach that speed in 0.5 sec. Acceleration is

calculated by: $\alpha = 2 * \Pi * \text{RPS} / \text{Time}$, where $\Pi = 3.14$, $\text{RPS} = 60 \text{ degree} / 360 \text{ degree} = 0.16667$, and $\text{Time} = 0.5 \text{ sec}$. Therefore, $\alpha = 2 (3.14) (0.16667 \text{ rps}) / 0.5 \text{ sec} = 2.093 \text{ rad/sec}^2$. Inertia is calculated by: $J = 1/12 m * (a^2+b^2)$, where $m = \text{mass} = 2.7 \text{ lb} = 43.2 \text{ oz}$, $a = \text{length} = 14.73 \text{ in}$, and $b = \text{width} = 10.63 \text{ in}$. Therefore, $J = 1187.9 * 0.00259 = 3.07 \text{ oz-in-sec}$ (including conversion factor). As a result, torque is calculated by: $T = \alpha \times J = 3.07 * 2.093 = 6.43 \text{ oz/in}$ (at 0.16667 rps).

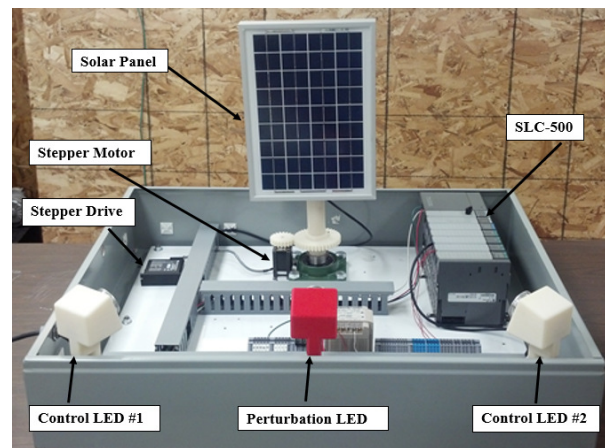
The selected stepper motor has a torque rating of 125oz/in which is much higher than what is required for the solar panel but was purchased to avoid motor overloaded. This stepper motor requires a stepper drive in order to control motor movement and function. SureStep offers various drivers that can be used to drive the STP-MTR-17060 stepper motor. The system driver needed to be highly efficient and have flexible controls to give the system good performance options. The SureStep STP-DRV-4850 [38] was selected to drive our stepper motor and is powered by 24-48 VDC and uses the SureStepPro software [39] for configuration.

The driver is capable of many different control modes such as step and direction, serial indexing, and velocity mode [39]. In our system, the velocity mode was implemented for easier speed control and ladder logic programming. In velocity mode the motor speed is dependent on the analog voltage value sent to the driver. The speed selection range is 0.1 rev/sec at 1 V to 0.5 rev/sec at 5 V. The STEP input of the driver is used for the Run/Stop of the motor, while the DIR input determines CW or CCW rotation. The analog value for speed is connected to the Analog Input of the driver. For smoother solar panel movement the stepper motor steps per revolution were set to 20,000 steps/rev.

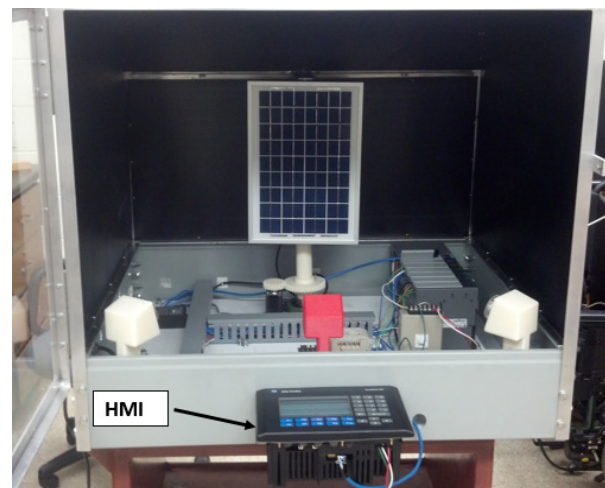
Three LED lights were used in the system with each light drawing 9 watts. Each light is fully dimmable with an output of about 410 Lumens apiece and a color temperature of 5400 K. The lights have a bi-pin configuration and are mounted in MR-16 sockets. Each light has a visible output as an approximate input of 8V and increases up to a maximum of 12V DC input.

An SLC-500 Allen Bradley PLC with a 5/04 CPU was used to communicate and control the entirety of the system with PID control. A Panel View 550 HMI was installed to assist in real-time monitoring of the process of the system configuration. The SLC-500 has seven rack slots for modules including the CPU. The modules used in our system include: three analog I/O modules, one analog input module, and one relay output module. The PLC controls the intensity of both control lights in accordance with the solar panel output voltage using PID control.

The base of our system enclosure consisted of a 36"Hx30"Wx8"D electrical box in which the components of the system were mounted to a sub-panel. To minimize the amount of unwanted ambient light in the system, the walls of the enclosure were constructed using black plastic sheets. An additional support was added to the top of the solar panel to add stability during rotation. The open system with labeled system components is shown in Figure 2 (a) and the fully enclosed system is shown Figure 2 (b). The system consists of the solar panel fastened to a rotating stand centered on the wide side of the system facing inwards, with the LED lights mounted on stands on the opposite side facing the panel. The panel stand is rotated by a gear system which is attached to the stepper motor. The output of the solar panel is connected to the input module of the PLC, and the inputs of the lights are wired to the analog output modules of the PLC.



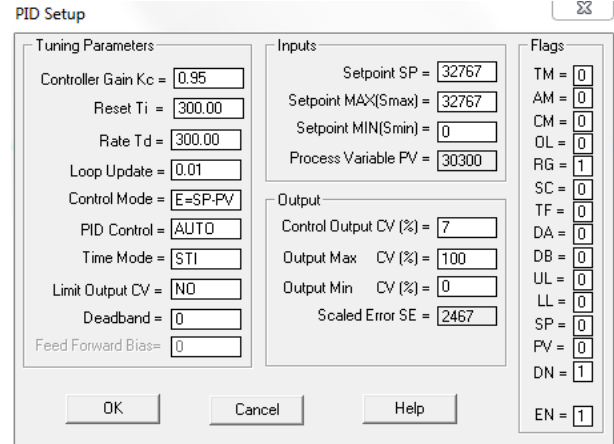
(a) System Components



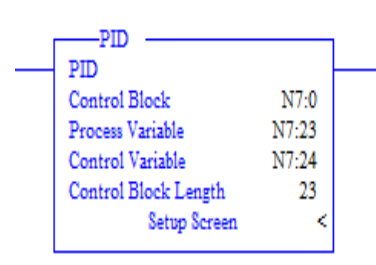
(b) Full Enclosure

Figure 2. Complete System

The stands used to mount the three LED lights in the system enclosure were designed in SolidWorks and 3D printed. The MR-16 bulb sockets were used for wiring and securing of the LED bulbs within the stands. The desired angles were then calculated for both the control and perturbation light stands since the control lights would be at further distances from the solar panel than the perturbation source. The stands were arranged to aim each light at the center of the solar panel. RSLogix500 was used to program the SLC-500 PLC. The main ladder logic program includes various different system functions which were implemented as subroutines in the program. Figure 3(a) shows the rungs of the main program which contain the directional control of the stepper motor. The position tracking of the solar panel was done via a timer and a counter and calculates the position based on the speed of the motor and how long it is enabled. The ladder logic rungs shown in Figure 3(b) make up the subroutine which is called when the oscillation mode is selected. The oscillation mode uses the positioning system to change the direction of the stepper motor once the panel has traveled just under 180 degrees. The intensity range of the perturbation light can be selected range by the user and the range selections include: full range, half range, and quarter range. The implementation of the PID controller is accomplished by configuring both the PID setup screen shown in Figure 4(a) and the PID block shown in Figure 4(b).



(a) PID Setup Screen

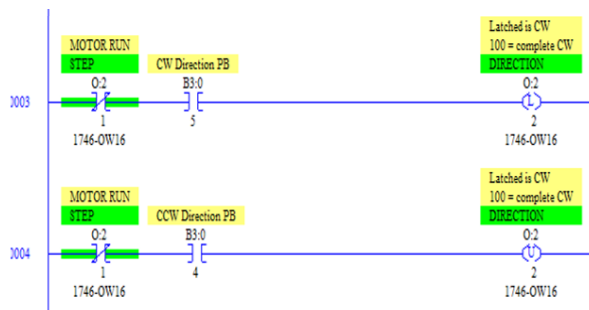


(b) PID Block

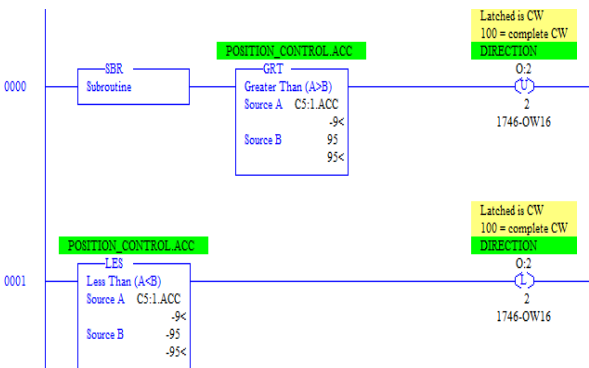
Figure 4. PID Module in Ladder Logic Program

HMI system menus were developed using PanelBuilder32 [40] software to allow the user to easily monitor and control the various functions of the system. The main menu of the system is shown in Figure 5 (a) and is where the user is able to navigate to different control and monitoring menus. With various HMI menus the user is able to adjust the perturbation LED light intensity, start and stop oscillation, change oscillation speed, and select the intensity range. The three selectable intensity ranges are full range, half range and quarter range. Various user controlled stepper motor functions through the HMI include stepper motor starting and stopping, the selection of speed, direction, and mode. The three stepper motor movement modes are oscillating, stop and manual/homing. Oscillation mode rotates the solar panel in a 180 degree range of motion while alternating between clockwise (CW) and counterclockwise (CCW) movement. Step mode rotates the solar panel from the center with a changing degree range.

The panel's initial rotation is 18 degrees CCW from center followed by the increase of 18 degrees for the next rotation range. The panel rotates up to 90 degrees, then returns to center and switches the direction of rotation from CCW to CW and repeats the process in the CW direction. The



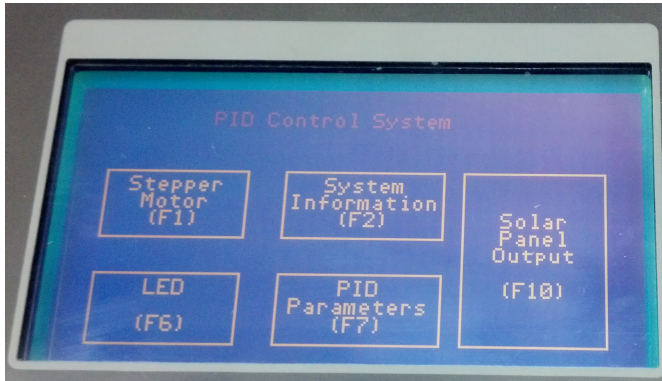
(a) Motor Direction Control



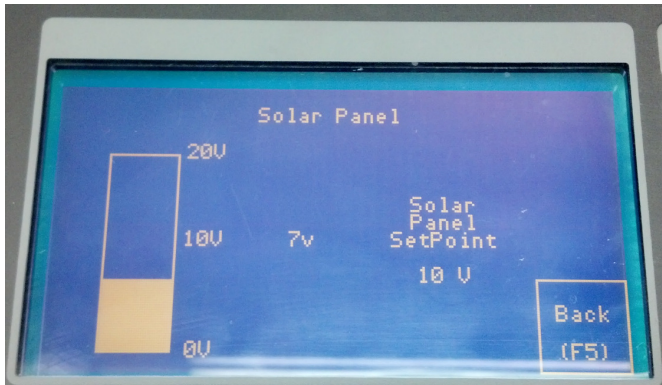
(b) Oscillation Mode

Figure 3. Ladder Logic Program

manual/homing mode is used for complete user controlled motor movement and for resetting the system position. Figure 5 (b) shows the HMI screen which allows the user to view the solar panel output voltage on a bar graph and number indicator in real-time alongside the setpoint value.



(a) System Main Menu



(b) Solar Panel Voltage Monitoring

Figure 5. HMI Screen

Results and Discussion

The testing of the PID controller in the system consisted of the implementation of a P, PI, and PID controller. The initial testing was without any perturbations in the system and was done to see how fast and accurately the set point was reached when the system was started. Figure 6 shows the system response for implementing P controllers with proportional gains of 0.5, 0.95, and 5. The controller with a proportional gain of 5 has the fastest rise time and the slowest settling time. This controller experiences the largest overshoot and is the only P controller to experience oscillation. For a controller with the gain set to 0.95 the rise time increases and the settling time decreases. With the decrease in the proportional constant the overshoot has decreased and

the oscillation has been removed. From the controller with a proportional gain of 0.5 the overshoot is completely removed, but the rise time has increased. Depending on the required rise time the proportional gain should be between 0.5 – 1 to minimize overshoot and steady state error; otherwise, the performance will be weak in terms overshoot, oscillations, and steady state error.

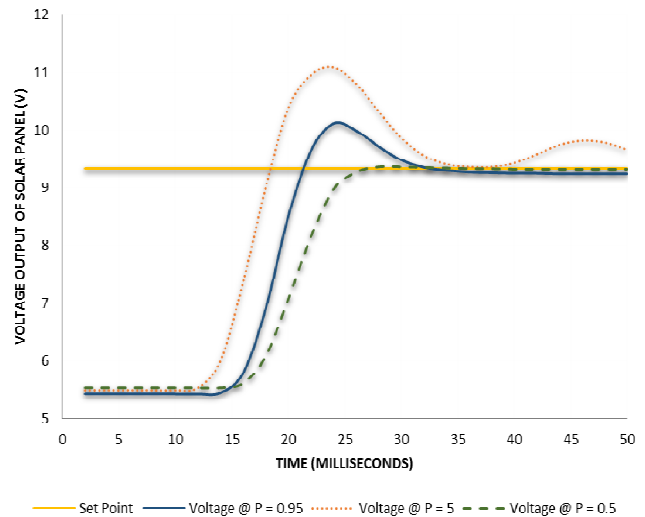


Figure 6. Proportional (P) Controller

Figure 7 shows the system response for implementing PI controllers with constant proportional gains of 0.95 and integral gains of 1, 50, and 300. The results show that as integral gain increases the rise time and settling time both slightly increase. The integral gain should be set close to 250 to minimize rise time and additional more aggressive perturbation scenarios will be used to validate various gain settings.

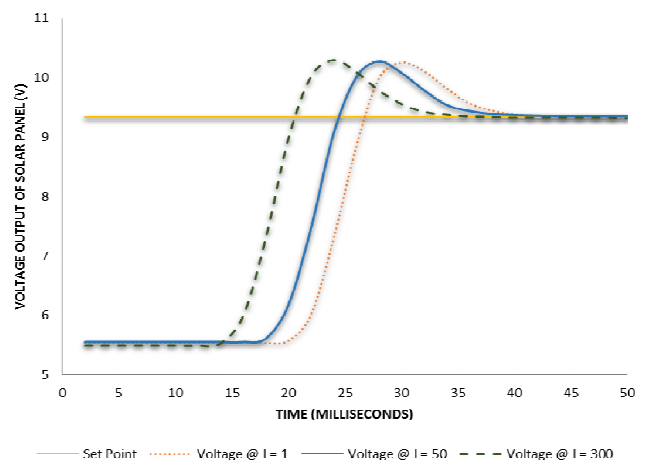


Figure 7. Proportional Integral (PI) Controller

Figure 8 shows the system response for implementing PID controllers with constant proportional gains of 0.95 and constant integral gains of 300 with derivative gains of 10, 75, and 300. For a low derivative gain of 10 the system response was quite unstable and never settled at the set point. For both derivative gains of 75 and 300 the system response was very similar, with slightly better overshoot for the gain of 75. In comparison to the PI controller, the addition of the derivative gain did not show a significant change in response. This was expected because testing had minimal future perturbations for the derivative gain to respond to. In Figure 8, the initial conditions are slightly different for the three test cases, and the difference is less than 0.25(V), which is an acceptable range to make a fair comparison among the three test cases. Additional testing will be done to further test the function of the PID controller and to determine the desired gain parameters for different test scenarios. Future test cases include changing the oscillation speed and intensity of the perturbation light, rotating the solar panel at different speeds and movement patterns, and combining both test cases to maximize the system perturbations for testing.

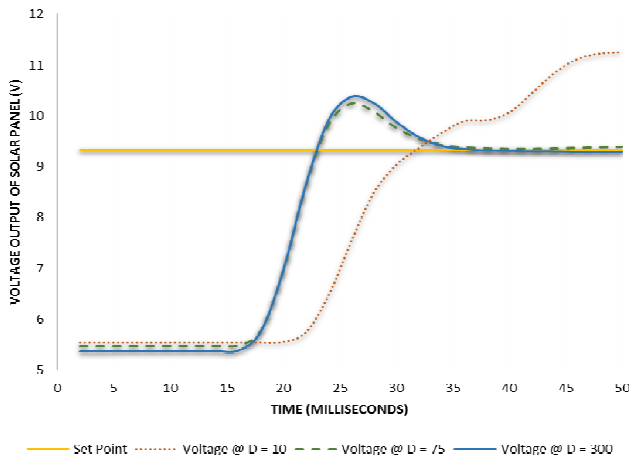


Figure 8. Proportional Integral Differential (PID) Controller

Conclusion

The PID controller was implemented into the completed system and testing confirmed the desired PID controller function. Based on initial results an implemented PI controller with a proportional gain of 0.6 and integral gain of 250 would be ideal for the system experiencing minimal perturbations. For the system experiencing various perturbations PID control should help with the stability of the system. With topics addressed in the system such as the basic input/outputs, system troubleshooting, complex PLC programming methods, HMI programming/implementation, and PID

controllers, this system can be used as an educational tool for students learning basic and advanced PLC techniques. Through this capstone project group members gained valuable experience with components such as PLCs, HMIs, solar panels and stepper motors and has been a valuable learning experience completing a complex system from design to completion.

At Michigan Tech, all School of Technology programs are designed to train technical professionals for employment in industry and business. In order to meet the expectations of the EET program in the SoT at Michigan Tech, the curriculum is constantly being enhanced to supply qualified engineers with extensive hands-on experience. As part of the continuous effort to prepare graduates of the School of Technology, an EET program at Michigan Tech engaged a group of EET students in solving engineering problems as part of capstone integrating experience and to fulfill the degree program requirements. Working with the advisors, the team was challenged to integrate a Programmable Logic Controller (PLC) with the Human Machine Interface (HMI) to create an effective PID controller.

With the conclusion of this project the team was able to meet all of the requirements given by the faculty advisor and fulfill the degree program requirements at Michigan Tech. Successful assembly and testing of the unit was accomplished. An extensive tutorial was created which include step-by-step instructions with images and figures on how to use HMI and PLC to run the pre-programmed operational cycle of the PID controller. The tutorial also includes the detailed instructions on how to reconfigure individual control functions to modify the operating cycle of the system. The situational scenario was also included in the tutorial and provides all necessary steps for configuring HMI and programming PLC to achieve all the tasks. The developed tutorial along with the build PID controlled system will serve the purpose of providing the hands-on PLC, HMI, and PID theory training to the students enrolled in introductory and advanced PLC courses.

Future Works

This senior design project research is being extended to further study the behavior of the optical system in depth, and to improve the performance of the PID controller. So far, it is identified that the optical system is highly nonlinear at some operating points, and the nonlinearity is due to a dead-band characteristic of the optical system. To this end, the performance of the optical system (in a closed-loop configuration with the PID controller) is very different from the performance of a linear system, and hence at some operating points, the observations from the optical system contra-

dict our expectations from a linear system. This research is being continued and the nonlinearity in the optical system is being studied in details. Therefore, this senior design research is ongoing along the following directions of future work:

- The optical system will be investigated to analyze the dynamic model of the system.
- Once the dynamic model is analyzed, different PID controller design techniques will be investigated, such as Ziegler-Nichols (ZN) and model-based techniques.

References

- [1] Bai, T., Zhu, J., & Varma, V. (2007). Characteristics of Capstone Design Projects at Universities in US and China: An Analysis. *Proceedings of the 2007 ASEE Annual Conference, Paper #2007-1755*.
- [2] Dutson, A. J., Todd, R. H., Magleby, S. P., & Sorensen, C. D. (1997, January). A Review of Literature on Teaching Engineering Design through Project-Oriented Capstone Courses. *Journal of Engineering Education, 86*(1), 17-28.
- [3] Pomberger, G. (1993). Software Engineering Education—Adjusting Our Sails. *Education and Computing, 8*(4), 287-294.
- [4] Thorpe, J. F. (1984). Design of Mechanical Systems: A Capstone Course in Mechanical Engineering Design. *Proceedings of the 1984 ASEE Annual Conference*, (pp. 803-807). Rochester, NY.
- [5] Todd, R. H., Magleby, S. P., Sorensen, C. D., Swan, B. R., & Anthony, D. K. (1995). A Survey of Capstone Engineering Courses in North America. *Journal of Engineering Education, 84*(2), 165-174.
- [6] Banios, E. W. (1992). Teaching Engineering Practices. *Proceedings of the 1992 Frontiers in Education Conference*, (pp. 161-168).
- [7] Todd, R. H., Sorensen, C. D., & Magleby, S. P. (1993). Designing a Senior Capstone Course to Satisfy Industrial Customers. *Journal of Engineering Education, 82*(2), 92-100.
- [8] Rochefort, S. (1985). An Innovative ChE Process Laboratory. *Chemical Engineering Education, 19*(3), 150-155, 161.
- [9] Frechleton, J. E., & Walter, W. W. (1994) Constructing Prototypes in a College-Wide Capstone Design Course. *Proceedings, Advances in Capstone Education Conference, Brigham Young University*, (pp. 177-180).
- [10] Durfee, W. K. (1994). Engineering Education Gets Real. *Technology Review, 97*(2), 42-52.
- [11] Born, R. C. (1992). A Capstone Design Experience for Electrical Engineers. *IEEE Transactions in Education, 35*(3), 240-242.
- [12] Magleby, S. P., Sorensen, C. D., & Todd, R. H. (1992). Integrated Product and Process Design: A Capstone Course in Mechanical and Manufacturing Engineering. *Proceedings of the 1992 Frontiers in Education Conference*, (pp. 469-474). West Lafayette, IN.
- [13] Sloan, D. E. (1982). An Experiential Design Course in Groups. *Chemical Engineering Education, 16*(1), 38-41.
- [14] Hamelink, J. H. (1994). Industrial Oriented Senior Design Projects: A Key for Industrial Experience. *Proceedings, Advances in Capstone Education Conference, Brigham Young University*, (pp. 87-89).
- [15] Walter, W. W. (1991). Using a Large-Displacement General Purpose Dynamics Code in a Capstone Design Course. *Twenty-Third International SAMPE Conference*, (pp. 288-296).
- [16] Zhan, W., Goulart, E. P., Morgan, J. A., & Bird, M. A. (2012). Integration of Capstone Experience and Externally Funded Faculty Research. *Proceedings of the 2012 ASEE Annual Conference*. San Antonio, TX.
- [17] Brackin, M. P., & Gibson, J. D. (2005). Capstone Design Projects with Industry: Emphasizing Teaming and Management Tools. *Proceedings of the 2005 ASEE Annual Conference*.
- [18] Karimi, A., Eftekhari, J., Manteufel, R., & Singh, Y. (2003). Industrially Supported Projects in a Capstone Design Sequence. *Proceedings of the 2003 ASEE Annual Conference*.
- [19] Corns, S., Dagli, C. H., & Guardiola, I. G. (2011). SE Capstone: Integrating Systems Engineering Fundamentals to Engineering Capstone Projects: Experiential and Active. *Proceedings of the 2011 ASEE Annual Conference*.
- [20] Crain, G. E., & Tull, M. P. (2004). A Capstone Course Targeting Industry Transition. *Proceedings of the 2004 ASEE Annual Conference*.
- [21] Gerbus, D., Cordon, D., Walker, M., Drew, R., Odom, E., Beyerlein, S., et al. (2002). Improving the Professional Skills of Engineering Graduate Students through a Capstone Project Mentoring in IEWorks. *Proceedings of the 2002 ASEE Annual Conference*.
- [22] King, L., El-Sayed, M., Sanders, M. S., & El-Sayed, J. (2005). Job Readiness through Multidisciplinary Integrated Systems Capstone Courses. *Proceedings of the 2005 ASEE Annual Conference*.
- [23] Sheppard, K. G., Nastasi, J., Hole, E., & Russell, P. L. (2011). SE Capstone: Implementing a Systems Engineering Framework for Multidisciplinary Capstone Design. *Proceedings of the 2011 ASEE Annual*

- Conference.
- [24] Redekopp, M., Raghavendra, C., Weber, A., Ragusa, G., & Wilbur, T. (2009). A Fully Interdisciplinary Approach to Capstone Design Courses. *Proceedings of the 2009 ASEE Annual Conference*.
- [25] Seaward, G. H. (2001). Converting Single Disciplinary Capstone Projects to Interdisciplinary Experiences. *Proceedings of the 2001 ASEE Annual Conference*.
- [26] Lumsdaine, E. (2007). Creative Problem Solving in Capstone Design. *Proceedings of the 2007 ASEE Annual Conference*.
- [27] Lin, Y., & Harby, D. (2004). Teaching Capstone Design in Globalization Environment. *Proceedings of the 2004 ASEE Annual Conference*.
- [28] Lin, Y., Harby, D., Jang, D., & Ye, Z. (2005). Problems and Solutions in Internationalizing Capstone Design. *Proceedings of the 2005 ASEE Annual Conference*.
- [29] Cooper, D. J. (1996). Picles: A Simulator for "Virtual World" Education and Training in Process Dynamics and Control. *Computer Applications in Engineering Education*, 4(3), 207-215.
- [30] Rahrooh, A., Motlagh, B., & Buchanan, W. (2005). Adaptive PID Controller Using PC MATLAB. *Proceedings of the 2005 ASEE Annual Conference*.
- [31] National Instruments. (2011, March 29). PID Theory Explained. Retrieved from <http://www.ni.com/whitepaper/3782/en/?vm=r&s=1>
- [32] Araki, M. (1984). PID Control. *Control Systems, Robotics, and Automation*, 2.
- [33] Ameresco Solar. (2013). Value Line Series (VLS) - 10W Panel. Retrieved from http://www.amerescosolar.com/sites/default/files/VLS-10W_1.pdf
- [34] Automation Direct. (2014). STP-MTR-17060. Retrieved from http://www.automationdirect.com/adc/Shopping/Catalog/Motion_Control/StepperSystems/Stepper_Motors_-z-_Cables/STP-MTR-17060
- [35] Automation Direct. (2014). STP-DRV-4850. Retrieved from http://www.automationdirect.com/adc/Shopping/Catalog/Motion_Control/Stepper_Systems/Stepper_Drives_-z-_Power/STP-DRV-4850
- [36] Automation Direct. (2014). STP-PRO. Retrieved from http://www.automationdirect.com/adc/Shopping/Catalog/Motion_Control/Stepper_Systems/Stepper_Drives_-z-_Power/STP-PRO.
- [37] Rockwell Automation. (2014). PanelBuilder32 Software. Retrieved from <http://ab.rockwellautomation.com/graphic-terminals/2711-panelbuilder32-software>
- [38] PID Controller. Wikipedia. Retrieved from http://en.wikipedia.org/wiki/PID_controller?vm=r&s=1
- [39] Demarest, J. T., Martin, C. D., & Darnell, J. H. (1998). Design of a Proportional Integral Derivative (PID) Controller for An Industrial Seminar. *ASEE*.
- [40] Craciun, C. (2011). Teaching Automation Using Real PLC's and Virtual Factories. *Proceedings of the ASEE Northeast Section Annual Conference*.
- [41] Barrett, M. (2008). The Design of a Portable Programmable Logic Controller (PLC) Training System for Use Outside the Automation Laboratory. *International Symposium for Engineering Education*, Dublin, Ireland.

Biographies

ABDULLAH AL ATWAH is graduating from Michigan Technological University in 2014 receiving his bachelor's degree in EET with a minor in Data Acquisition and Industrial Control.

IAN BUMGARDNER is graduating with a B.S. degree in EET from Michigan Technological University. He focuses on industrial controls and automation, with experience in a high volume manufacturing environment.

MOHAMMED BUSHLAIBI is graduating with a bachelor's degree in EET in 2014 from Michigan Technological University. He is interested in control systems.

STEVEN CASTELLO graduated with a B.S. degree in EET from Michigan Technological University in 2013. He is currently working as a control systems engineer for Dematic Corp.

JOSHUA ERICKSON is graduating with a B.S. degree in EET from Michigan Technological University with a minor in Data Acquisition and Industrial Control and a minor in Mathematical Sciences. He is currently employed as a controls systems engineer for Dematic Corp.

ALEKSANDR SERGEYEV is currently an Associate Professor in EET program in the School of Technology at Michigan Tech. Dr. Sergeyev is a member of ASEE, IEEE, SPIE and is actively involved in promoting engineering education. Dr. Sergeyev may be reached at avsergue@mtu.edu

MOHSEN AZIZI joined Michigan Technological University as an Assistant Professor of Electrical Engineering Technology program in 2013. He was a R&D Engineer with Pratt & Whitney Canada Inc. from 2010 to 2013. His research interests include control systems and diagnostics in jet engines, unmanned vehicles, and aircraft. He is a member of IEEE. Dr. Azizi may be reached at sazizi@mtu.edu

INSTRUCTIONS FOR AUTHORS: MANUSCRIPT REQUIREMENTS

The INTERNATIONAL JOURNAL OF ENGINEERING RESEARCH AND INNOVATION is an online/print publication, designed for Engineering, Engineering Technology, and Industrial Technology professionals. All submissions to this journal, submission of manuscripts, peer-reviews of submitted documents, requested editing changes, notification of acceptance or rejection, and final publication of accepted manuscripts will be handled electronically. The only exception is the submission of separate high-quality image files that are too large to send electronically.

All manuscript submissions must be prepared in Microsoft Word (.doc or .docx) and contain all figures, images and/or pictures embedded where you want them and appropriately captioned. Also, for all accepted manuscripts, each figure, image or picture that was imported into your Word document must be saved individually as a **300dpi or higher JPEG (.jpg)** file and submitted separately; your manuscript and figure numbers must be used in the title of the file (e.g., **J13-F-18 Figure 4**); that means one additional file for each image imported into your manuscript. These 300dpi images do NOT need to be embedded in your manuscript. For tables or graphs created directly in Word, you do not need to submit them as separate files.

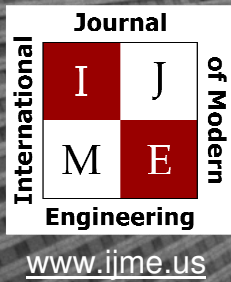
Included below is a summary of the formatting instructions. You should, however, review the [sample Word document](http://www.ijeri.org/formatting_guidelines) on our website (www.ijeri.org/formatting_guidelines) for details on how to correctly format your manuscript. The editorial staff reserves the right to edit and reformat any submitted document in order to meet publication standards of the journal.

The references included in the References section of your manuscript must follow APA-formatting guidelines. In order to help you, the sample Word document also includes numerous examples of how to format a variety of scenarios. Keep in mind that an incorrectly formatted manuscript will be returned to you, a delay that may cause it (if accepted) to be moved to a subsequent issue of the journal.

1. **Word Document Page Setup:** Two columns with ¼" spacing between columns; Top of page = ¾"; Bottom of page = 1" (from the top of the footer to bottom of page); Left margin = ¾"; Right margin = ¾".
2. **Paper Title:** Centered at the top of the first page with a 22-point Times New Roman (Bold), Small-Caps font.
3. **Page Breaks:** Do not use page breaks.
4. **Body Fonts:** Use 10-point Times New Roman (TNR) for body text throughout (1/8" paragraph indentation); 9-point TNR for author names/affiliations under the paper title; 16-point TNR for major section titles; 14-point TNR for minor section titles; 9-point TNR BOLD for caption titles for tables and figures; other font sizes as noted in the sample document.
5. **In-text Referencing:** List and number each reference when referring to them in the body of your document (e.g., [1]). The first entry must be [1] followed by [2], [3], etc., continuing in numerical order to the final entry in your References section. Again, see the sample Word document for specifics. Do not use the End-Page Reference utility in Microsoft Word. You must manually place references in the body of the text.
6. **Tables and Figures:** Center all tables and figures. Captions for tables must be above the table, while captions for figures are below; all captions are left-justified.
7. **Page Limit:** Manuscripts should not be more than 15 pages (single-spaced, 2-column format).
8. **Page Numbering:** Do not use page numbers.
9. **Publication Charges:** Manuscripts accepted for publication are subject to mandatory publication charges.
10. **Copyright Agreement:** A Copyright Transfer Form must be signed and submitted by all authors on a given paper before that paper will be published.
11. **Submissions:** All manuscripts and associated files must be submitted electronically.

MANUSCRIPTS should be submitted to Dr. Philip D. Weinsier, manuscript editor, at philipw@bgsu.edu along with a copy to editor@ijeri.org.

FILES containing your high-quality images should ONLY be submitted to philipw@bgsu.edu.



Print ISSN: 2157-8052
Online ISSN: 1930-6628



INTERNATIONAL JOURNAL OF MODERN ENGINEERING

ABOUT IJME:

- IJME was established in 2000 and is the first and official flagship journal of the International Association of Journal and Conferences (IAJC).
- IJME is a high-quality, independent journal steered by a distinguished board of directors and supported by an international review board representing many well-known universities, colleges and corporations in the U.S. and abroad.
- IJME has an impact factor of **3.00**, placing it among the top 100 engineering journals worldwide, and is the #1 visited engineering journal website (according to the National Science Digital Library).

OTHER IAJC JOURNALS:

- The International Journal of Engineering Research and Innovation (IJERI)
For more information visit www.ijeri.org
- The Technology Interface International Journal (TIIJ).
For more information visit www.tiij.org

IJME SUBMISSIONS:

- Manuscripts should be sent electronically to the manuscript editor, Dr. Philip Weinsier, at philipw@bgsu.edu.

For submission guidelines visit
www.ijme.us/submissions

TO JOIN THE REVIEW BOARD:

- Contact the chair of the International Review Board, Dr. Philip Weinsier, at philipw@bgsu.edu.

For more information visit
www.ijme.us/ijme_editorial.htm

INDEXING ORGANIZATIONS:

- IJME is indexed by numerous agencies.
For a complete listing, please visit us at www.ijme.us.

Contact us:

Mark Rajai, Ph.D.

Editor-in-Chief
California State University-Northridge
College of Engineering and Computer Science
Room: JD 4510
Northridge, CA 91330
Office: (818) 677-5003
Email: mrajai@csun.edu



www.tiij.org



www.ijeri.org

The International Journal of Engineering Research & Innovation (IJERI) is the second official journal of the International Association of Journals and Conferences (IAJC). IJERI is a highly-selective, peer-reviewed print journal which publishes top-level work from all areas of engineering research, innovation and entrepreneurship.



IJERI Contact Information

General questions or inquiries about sponsorship of the journal should be directed to:

Mark Rajai, Ph.D.

Founder and Editor-In-Chief

Office: (818) 677-5003

Email: editor@ijeri.org

Department of Manufacturing Systems Engineering & Management

California State University-Northridge

18111 Nordhoff St.

Room: JD3317

Northridge, CA 91330